Max-Planck-Institut
für Meteorologie

MAX-PLANCK-GESELLSCHAFT

International Max Planck Research School
on Earth System Modelling

Modelling the Carbon Cycle during the Paleocene-Eocene Thermal Maximum

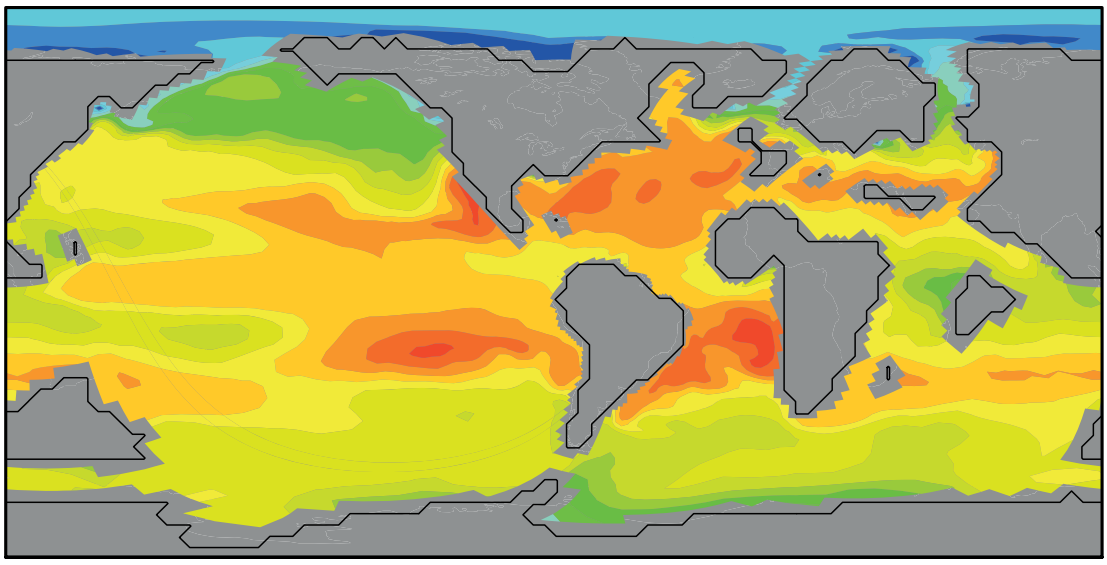

Mathias Heinze

Hamburg 2015

Berichte zur Erdsystemforschung
Reports on Earth System Science

165
2015

Hinweis

Die Berichte zur Erdsystemforschung werden vom Max-Planck-Institut für Meteorologie in Hamburg in unregelmäßiger Abfolge herausgegeben.

Sie enthalten wissenschaftliche und technische Beiträge, inklusive Dissertationen.

Die Beiträge geben nicht notwendigerweise die Auffassung des Instituts wieder.

Die "Berichte zur Erdsystemforschung" führen die vorherigen Reihen "Reports" und "Examensarbeiten" weiter.

Notice

The Reports on Earth System Science are published by the Max Planck Institute for Meteorology in Hamburg. They appear in irregular intervals.

They contain scientific and technical contributions, including Ph. D. theses.

The Reports do not necessarily reflect the opinion of the Institute.

The "Reports on Earth System Science" continue the former "Reports" and "Examensarbeiten" of the Max Planck Institute.

Anschrift / Address

Max-Planck-Institut für Meteorologie
Bundesstrasse 53
20146 Hamburg
Deutschland

Tel./Phone: +49 (0)40 4 11 73 - 0
Fax: +49 (0)40 4 11 73 - 298

name.surname@mpimet.mpg.de
www.mpimet.mpg.de

Layout

Bettina Diallo and Norbert P. Noreiks
Communication

Copyright

Modelling the Carbon Cycle during the Paleocene-Eocene Thermal Maximum

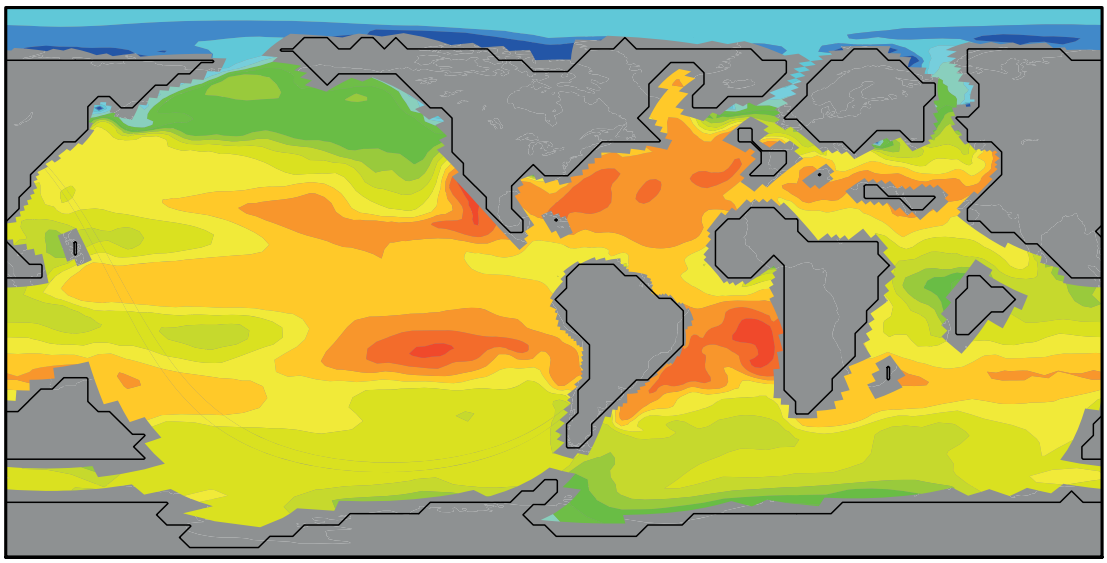

Mathias Heinze

Hamburg 2015

Mathias Heinze

Max-Planck-Institut für Meteorologie
Bundesstrasse 53
20146 Hamburg

Als Dissertation angenommen
vom Fachbereich Geowissenschaften der Universität Hamburg

auf Grund der Gutachten von
Prof. Dr. Gerhard Schmiedl
und
Dr. Tatiana Ilyina

Hamburg, den 25.11.2014
Prof. Dr. Christian Betzler
Leiter des Departments Geowissenschaften

Berichte zur Erdsystemforschung / Max-Planck-Institut für Meteorologie 165
Reports on Earth System Science / Max Planck Institute for Meteorology 2015

ISSN 1614-1199

Abstract

The Paleocene-Eocene Thermal Maximum (PETM, ∼56 million years ago) was a transient global warming event, characterized by a prominent negative carbon isotope excursion (CIE) in the proxy record, most likely caused by a massive input of carbon to the ocean and atmosphere.

Despite several plausible hypotheses, the exact rate of carbon release and the ultimate location of the carbon source remain unknown. The deep ocean conditions must have been inhospitable to marine organisms, since PETM sediment records indicate a mass extinction of benthic foraminifera and vast dissolution of $CaCO_3$ sediments. Both, ocean circulation and marine biogeochemistry must have been affected by the carbon perturbation of the PETM.

Until now, however, modelling studies did not consider the changes in the ocean circulation together with the changes in ocean biogeochemistry. As ocean circulation state is key in shaping the marine carbon cycle the current interpretation of the PETM proxy record may be incomplete. To address this issue, we simulate the Late Paleocene background climate and the onset of the PETM with the state of the art Earth System Model of the Max Planck Institute (MPI-ESM).

The background climate and ocean biogeochemistry state are important for studying the PETM itself. Therefore, simulations start in the warm steady-state climate of the Late Paleocene. We spin up the ocean biogeochemistry over several thousand years in an ocean stand alone model setup to establish plausible water column and sediment conditions for the marine carbon cycle parameters. In a second step, we use a coupled model setup, based on a newer version of the atmospheric general circulation model ECHAM. The comparison of the results of the two model configurations reveals major differences due to changes in the location of deepwater formation areas. Model results show, that already in the Late Paleocene, ocean circulation driven by deepwater formation in the Southern Hemisphere produces a horizontally reversed carbonate ion (CO_3^{2-}) gradient between the deep Atlantic and Pacific in comparison to modern conditions.

For the onset of the PETM, model scenarios of different carbon release rates and locations are performed. For the first time we show that weakening of the Southern Ocean deepwater formation and enhancement of ocean stratification in response to the carbon perturbation is key mechanism to reproduce the $CaCO_3$ dissolution pattern of the PETM suggested by the proxy record. Reduced ocean ventilation causes the products of organic matter remineralization (releasing PO_4, CO_2 and consuming O_2) to be trapped in intermediate waters. Thereby, deoxygenation and dissolution of $CaCO_3$ are triggered throughout the water column.

The stagnation of the ocean and the isolation effect of the deep ocean due to the reduced ventilation exceed the effect of higher input rates of carbon from the atmosphere. In summary, we conclude that while rising atmospheric CO_2 must have determined the response of ocean biogeochemistry to the carbon cycle perturbation during the PETM, ocean circulation modulated it. In this context we suggest a maximum atmospheric CO_2 increase rate of about 1 Gt C yr^{-1}, which is in agreement with surface and deep ocean biogeochemistry properties and is consistent with available proxy data.

Our results provide guidance for proxy data studies focusing on the reconstruction of the evolution of deepwater formation. Furthermore, the importance of the effects of reduced ventilation and increased respiration of organic matter for marine biogeochemistry demonstrated in our study, is of high relevance for research on the future climate under rising CO_2.

Contents

Chapter 1

Introduction

1.1 Motivation and research questions

The Paleocene-Eocene Thermal Maximum (PETM, ∼56 million years ago) describes a time period of about 170 kyr, which is characterized by an increase of mean surface temperatures of ∼6 ℃ (e.g., Kennett and Stott 1991; Zachos et al. 2003; Sluijs et al. 2006). This warming is attributed to the release of thousands of Gt of isotopically light carbon (1 Gt=10^{15} g) into the ocean-atmosphere system, which led to a negative $\delta^{13}C$ carbon isotope excursion (CIE) of about 4 ‰ and the massive dissolution of marine carbonates throughout the deep sea (e.g., Zachos et al. 2005; Zeebe et al. 2009; Ridgwell and Schmidt 2010). During the PETM, the atmospheric CO_2 concentrations and concomitant warming increased significantly over a relatively short time period of less than 10 kyr (Zeebe et al. 2009; Sluijs et al. 2012), starting from an already warmer background climate than today. However, the exact atmospheric CO_2 content before the PETM, as well as the maximum values of CO_2 during the PETM still remain poorly constrained. Estimates of atmospheric CO_2 concentration range from 600 to 2800 ppmv for the pre-PETM (Dunkley Jones et al. 2010; Pagani et al. 2006a).
In the ocean the different basins must have been affected by varying degrees of ocean acidification since the deep-sea carbonate dissolution pattern was characterized by stronger dissolution in the Atlantic than in the Pacific Ocean (Zeebe and Zachos 2007; Zeebe et al. 2009). The carbon input had only a moderate long-term impact on the surface ocean saturation state (Gibbs et al. 2006b), but the deep ocean biogeochemistry was much more affected by the carbon perturbation. Globally, about 30-50 % of species of benthic foraminifera went extinct during the event (Thomas 2007).
In terms of atmospheric CO_2 increase rate and (rapid) global warming, the PETM is dealt as the closest analogue to the ongoing present-day climate change (Ridgwell and Schmidt 2010; Hoenisch et al. 2012). This similarity widens the interest in studying and understanding the PETM climate state and in reconstructing the oceanic carbon cycle during this period. Although, carbon cycle boundary conditions before the PETM were different from modern conditions, the PETM serves as a case study for ocean acidification caused by anthropogenic CO_2 increase (Zeebe 2012b).

In this study I use the Max Planck Institute-Earth System Model (MPI-ESM), to study the transient changes in the ocean biogeochemistry during the PETM, as well as the long-term steady state ocean biogeochemistry of the Late Paleocene. The MPI-ESM consists of the coupled general circulation models for the atmosphere and the ocean, ECHAM6 (Stevens et al. 2013) and MPIOM (Jungclaus et al. 2013) and the subsystem models JSBACH (Reick et al. 2013) and HAMOCC (Ilyina et al. 2013) for simulating land/vegetation and the marine biogeochemistry, respectively.
For modelling the transient changes in ocean biogeochemistry in response to the carbon perturbation during the PETM, it is essential to establish the preceding background climate state of the Late Paleocene. This period was characterized by warm and stable climatic conditions, bearing ice-free conditions at the poles (Zachos et al. 2001). Typical for warm periods in Earth's past, the pole-equator temperature gradient used to be smaller during the Late Paleocene, featuring much higher temperatures in high latitudes (Sluijs et al. 2006; Lunt et al. 2012). As a consequence of climatic conditions and continental configuration/bathymetry, the ocean circulation differed to today's circulation state, since the main area of deepwater formation was likely located in the Southern Ocean (Thomas et al. 2003; Tripati and Elderfield 2005; Nunes and Norris 2006).
Modelling studies of the Late Paleocene address primarily the ocean and atmospheric circulation and climate state (Huber and Sloan 2001; Heinemann et al. 2009; Winguth et al. 2010). However, due to the different climate and higher atmospheric CO_2 content, ocean biogeochemical parameters must have been distributed differently to modern conditions, but only little is known about the ocean biogeochemistry during that time. Carbon cycle reconstructions are based on Earth system models of intermediate complexity (EMIC) and box models (Panchuk et al. 2008; Zeebe et al. 2009; Ridgwell and Schmidt 2010). There is no modelling study about Late Paleocene ocean biogeochemistry including a complex carbon cycle. Therefore, I spin up the ocean biogeochemistry in a ocean stand-alone configuration (MPIOM/HAMOCC) to answer the first research question:

1.) **Can the ocean biogeochemistry of the Late Paleocene be further constrained by using a complex ESM?**

Under Late Paleocene boundary conditions, the initial state in the ocean's carbonate chemistry before the PETM is expected to have been different to the pre-industrial one. For instance, the carbonate buffer capacity could have varied to the modern one due to generally higher atmospheric CO_2 concentrations (Zeebe 2012b), which would in turn influence the oceanic CO_2 uptake capacity during the PETM. Moreover, there are still high uncertainties concerning the Late Paleocene carbonate compensation depth

(CCD), the depth at which $CaCO_3$ is no longer found in sediments ($CaCO_3$ dissolution $>$ $CaCO_3$ precipitation). Changes in the CCD are used as a proxy for oceanic CO_2 uptake and concomitant ocean acidification in past climates. Zeebe et al. (2009) estimated the size of the PETM carbon input based on sediment records of deep-sea carbonate dissolution. However, quite different estimates of required CO_2 injection to the ocean, derived from $CaCO_3$ dissolution, are related to uncertainties in the pre-PETM CCD. Panchuk et al. (2008), for instance, suggest a deeper pre-PETM CCD for the Pacific and Atlantic Ocean than Zeebe et al. (2009). Based on answers to research question 1, I want to further constrain the carbonate chemistry of the surface and deep oceans and investigate if sedimentary $CaCO_3$ would be more or less vulnerable to dissolution in the different ocean basins. Therefore, I address the following question:

2.) **Did the Late Paleocene climate state influence the ocean biogeochemistry's sensitivity towards a carbon perturbation during the PETM?**

As a consequence of atmospheric CO_2 increase and concomitant warming during the onset of the PETM, the Southern Ocean deepwater formation decreased (Tripati and Elderfield 2005; Nunes and Norris 2006). Furthermore, a switch of deep water formation from southern to northern high latitudes during the onset of the PETM is discussed (Bice and Marotzke 2002).
Studies of the future high CO_2 world investigated the response of the ocean biogeochemistry to circulation changes in ESM simulations (e.g., Bopp et al. 2002; Najjar et al. 2007). Climate change induced increase of surface stratification and decrease of intermediate and deep water formation strongly influence marine ecosystems and deep ocean tracer concentrations, promoting processes such as deoxygenation and lowering of primary production (Bopp et al. 2013; Seferian et al. 2013).
Modelling studies concerning the ocean carbon cycle during the PETM do not, or just insufficiently, account for change in physical conditions, e.g., changes in ocean circulation. Winguth et al. (2012) simulated the PETM with the Community Climate System Model Version 3 (CCSM3). They predict a general weakening of deepwater formation and changing ocean circulation due to CO_2 induced warming. However, they just analyze export production and oxygen concentrations to study processes related to the benthic extinction during the PETM. Panchuk et al. (2008), investigate the marine carbon cycle during the PETM, but their simulation does not predict a weakening of Southern Ocean deep water production. Zeebe et al. (2009) run several simulations of the PETM with a box model. They prescribe a weakening of the Southern Ocean deepwater formation, but instead add a second deepwater source in the North Pacific. Hence, former studies did not investigate the alterations in circulation patterns of ocean currents in response to the carbon perturbation together with carbon cycle modelling.

Therefore, important processes to explain the PETM CIE may not have been considered when interpreting the proxy record.
The presented study is the first attempt to simulate the ocean biogeochemical response to a PETM related carbon perturbation with an ESM based on general circulation models of the atmosphere and ocean including the ocean biogeochemistry.
Changes in ocean circulation have only received little attention in relation to:
(1) the deep ocean carbonate chemistry during the PETM and its influence on $CaCO_3$ dissolution, which differed strongly between the single ocean basins (Thomas et al. 2002; Zachos et al. 2005). While the $CaCO_3$ dissolution was only weak in the Pacific (CCD shoaled several 100 meters), the Atlantic Ocean showed severe dissolution of $CaCO_3$ and concomitant CCD shoaling of 2 km (Zeebe et al. 2009).
(2) The benthic extinction event. Deep-sea benthic foraminifera suffered severe extinction (30-50 % of species) globally, while pelagic-planktonic organisms showed only smaller changes in total abundance during the PETM (Thomas 2007). Proxy records show that the perturbation of surface water saturation state which coincided with the onset of the PETM was not detrimental to most calcareous nannoplankton taxa (Gibbs et al. 2006b, 2013). The differences in the planktonic and benthic response to the carbon perturbation could imply a less intense coupling of surface and deep ocean biota at the Paleocene-Eocene boundary. This decoupling is also seen in a delay in the benthic $\delta^{13}C$ carbon isotope signal (compared to the surface) in the sediment record spanning the PETM (Thomas et al. 2002; Zachos et al. 2008). Several studies discuss the single reasons for the extinction event, but it seems to be most likely that the covariation of ocean acidification, warming, and corresponding oxygen depletion could have led to the PETM extinction event (Ridgwell and Schmidt 2010; Thomas 2007). Since our model accounts for all of the mentioned stressors, it is possible to evaluate if the deep ocean tends to become inhospitable during the onset of the PETM and if so to define more closely the driving mechanisms behind it. Therefore, I propose the following research question:

3.) **How did the ocean circulation affect the marine carbon cycle and the biology in response to the PETM carbon perturbation?**

Several possible carbon emission scenarios are discussed for the onset of the PETM (e.g., Pagani et al. 2006a; Zeebe et al. 2009). The carbon emission pathways differ in their emission rate as well as in the location of the carbon source. PETM modelling studies conclude that annual emission rates of 0.6 Gt C (Zeebe et al. 2009) and 0.68 Gt C (Panchuk et al. 2008) would be sufficient to reproduce the CIE, but they fail to obtain the global warming of 6 °C, unless a much higher climate sensitivity than today is assumed. Furthermore, the models produce too strong $CaCO_3$ dissolution in the

Pacific, if annual emission rates exceed the values of Panchuk et al. (2008); Zeebe et al. (2009). However, Hoenisch et al. (2012) hypothesize that CO_2 emissions of $\geqq$1 Gt C are necessary to produce the appropriate signal in the ocean acidification proxy record. Also Penman et al. (2014) give estimates of atmospheric CO_2 increase rates needed to reproduce the proxy derived surface pH decrease during the PETM, which are higher than the one applied in the existing modelling studies.
Besides the annual atmospheric emission rate, additional carbon sources in the ocean (methane hydrate decomposition) represent a possible mechanism for driving the PETM warming and the CIE (Dickens et al. 1995; Thomas et al. 2002). For instance Zeebe et al. (2009) prescribe 40 % of the prescribed carbon emissions directly in the deep Atlantic in order to reproduce the $CaCO_3$ dissolution record between the Atlantic and the Pacific. This leads me to the following research question:

4.) **What is the relevance of different sources and rates of carbon perturbation for the marine biogeochemistry?**

Besides the discussion of how much carbon is needed to produce the PETM global warming and negative CIE (Dickens et al. 1997; Zeebe et al. 2009; Cui et al. 2011), another uncertainty/unknown lies in the prolonged warming during the body of the CIE, covering a period of 100 kyrs (Zeebe 2013; Zeebe and Zachos 2013). Feedback processes in the carbon cycle could have driven this long lasting warming by keeping atmospheric CO_2 concentrations at an elevated level. Modelling the PETM carbon perturbation with a complex ESM could give some indication if feedback processes contributed to this warming. In this context I state the following research question:

5.) **Did feedback mechanisms between climate and ocean carbon cycle play a role for maintaining elevated atmospheric CO_2 and temperatures throughout the PETM?**

1.2 Thesis Outline

Each of the three main chapters of this thesis is written in the style of journal publications. As a consequence, they contain their own introduction and conclusions, and can be read largely independently of one another.
In **Chapter 2**, I present the simulation of the ocean biogeochemistry steady state during the Late Paleocene. A warm period in Earth climate which served as the background state for the PETM. The conducted simulation is carried out with a stand-alone modelling setup. This work has been submitted to 'Climate of the Past' for publication and is currently under revisions (Heinze and Ilyina 2014).

Chapter 3 gives a description of the coupled PETM model setup, which is used for the simulations of the PETM carbon perturbation. Furthermore, different climate states for the Late Paleocene are analyzed and discussed, which result from the stand-alone and fully coupled model setup used in Chapter 2 and Chapter 4, respectively.
Chapter 4 deals with the response of the marine carbon cycle to a carbon perturbation which is related to the PETM. I present several carbon emission scenarios and analyze the response of the ocean biogeochemistry. The conducted simulations are carried out with the fully coupled model setup.
In **Chapter 5** I draw the main conclusions from the work presented in this thesis. Furthermore I give an outlook on possible future research.

Chapter 2

Ocean biogeochemistry in the warm climate of the Late Paleocene

2.1 Introduction

The Late Paleocene has received interest because of its role as background climate for the Paleocene-Eocene Thermal Maximum (PETM), which could have been a possible analogue for present-day greenhouse warming and ocean acidification (e.g. Zachos et al. 2005; Ridgwell and Zeebe 2005; Zeebe and Zachos 2013). The PETM describes a time period of about 170 kyr, which is characterized by an increase in mean surface temperatures of more than 5 ℃ (Kennett and Stott 1991; Dickens et al. 1995; Zachos et al. 2008). During the PETM, the atmospheric CO_2 values increased significantly over a relatively short time period of about 10 kyr (Panchuk et al. 2008). Nonetheless, the question about the exact atmospheric CO_2 content before the PETM, as well as the maximum values of CO_2 during the PETM still remains unanswered (e.g., Pagani et al. 2006a).

The climate of the Late Paleocene was characterized by higher global average temperatures than in present-day, bearing ice-free conditions at the poles (Zachos et al. 2001). The pole-equator temperature gradient was smaller, displaying in sea surface temperatures (SST) of >30 ℃ in the tropics (Pearson et al. 2001), and up to 20 ℃ in high latitudes (Sluijs et al. 2006; Lunt et al. 2012). Deep ocean water masses were up to 10 ℃ warmer compared to modern values (Kennett and Stott 1991; Zachos et al. 2008; Tripati and Elderfield 2005). The warmer climate and the Late Paleocene continental configuration influenced global ocean circulation patterns. The main deepwater formation occurred in southern high latitudes, with additional minor regions of deepwater formation in the northern hemisphere (Thomas et al. 2003). There is no consensus if the northern hemisphere deepwater formation was stronger in the Atlantic or the Pacific (e.g., Bice and Marotzke 2002; Tripati and Elderfield 2005; Nunes and Norris 2006).

Hitherto, the focus of modeling the Late Paleocene with complex Earth System Models (ESM) was set to the physical ocean and atmospheric system (Huber and Sloan 2001;

Heinemann et al. 2009; Winguth et al. 2010). Studies about the PETM background climate show a wide range of inter-model variability, using prescribed atmospheric CO_2 concentrations ranging from 2x to 16x pre-industrial CO_2 (Lunt et al. 2012). In previous studies the Late Paleocene ocean biogeochemistry has been addressed exclusively with Earth System Models of intermediate complexity (EMIC) or box models (e.g., Panchuk et al. 2008; Zeebe et al. 2009; Ridgwell and Schmidt 2010; Winguth et al. 2012). These modeling studies are covering the whole PETM, with the major objective of constraining the absolute amount of the carbon perturbation. Their approach is based on reconstructions of the calcium carbonate compensation depth (CCD). By observing vertical shifts in the $CaCO_3$ dissolution horizons in sediment cores, before and after the peak of the event, rough estimates of the carbon perturbation during the PETM can be obtained. The depth of the pre-PETM CCD is still under discussion for wider geographical areas of the Late Paleocene oceans (Zeebe and Zachos 2013). This leads to quite different estimates of total carbon mass and carbon injection speed into the climate system, necessary to obtain the observed sedimentary $CaCO_3$ dissolution (Dunkley Jones et al. 2010). Hence, the preceding conditions of ocean biogeochemistry are important for a realistic assessment of the PETM itself in order to gain knowledge about ocean biogeochemistry's influence on feedback mechanisms for the PETM, e.g. alterations in the carbonate buffer capacity. Yet, estimates of for instance, total alkalinity (TA) and dissolved inorganic carbon (DIC) during the Late Paleocene are not well known at present (Dunkley Jones et al. 2010).

In order to further constrain the state of the oceanic part of the carbon cycle during the Late Paleocene, we spin up and run the Hamburg Ocean Carbon Cycle model, HAMOCC, and the Max Planck Institute Ocean Model, MPIOM, under Late Paleocene boundary conditions into an equilibrium state. Estimates for Late Paleocene atmospheric CO_2 concentrations range from 600 to 2800 ppm Pagani et al. (2006a). Based on Heinemann et al. (2009) we use a 560 ppm CO_2 Late Paleocene atmospheric forcing to achieve a plausible background climate for the PETM. The applied atmospheric CO_2 concentrations and Late Paleocene boundary conditions cause a new equilibrium climate state, which fits the proxy record based SST quite well (Lunt et al. 2012). Our study gives more detailed insights to the pre-PETM ocean biogeochemistry, since it is not only affected by modifications in temperature and atmospheric conditions at the ocean-atmosphere boundary (Archer et al. 2004), but also by alterations in the general ocean physical state. We answer the question how the vertically stratified ocean state affects the oceanic part of the carbon cycle and how the general higher concentration of atmospheric CO_2 influences the carbonate chemistry.

The used model has been applied in a number of previous studies, simulating the pre-industrial, modern and future climate/ocean state, for example in the framework of the climate model intercomparison project (CMIP5; Ilyina et al. 2013). Therefore here we also use data of the CMIP5 experiments for comparison. This data is based on calcula-

tions with the Max Planck Institute for Meteorology-Earth System Model (MPI-ESM), for pre-industrial (1850-1879) climatic conditions.
In section 2 of this paper we describe the model and give detailed information on the spin up of HAMOCC under Late Paleocene conditions. The general Late Paleocene climate state achieved by our simulation is presented in section 3. Section 4 comprises the results of the modeled ocean biogeochemistry, followed by the conclusions in section 5.

2.2 Model description & setup

2.2.1 The ocean biogeochemistry model HAMOCC

For our study we employ the Hamburg Ocean Carbon Cycle model (HAMOCC 5.1), which is based on Maier-Reimer (1993) and successive refinements (Maier-Reimer et al. 2005). HAMOCC simulates 18 biogeochemical tracers in the oceanic water column and 12 tracers in the upper 14 cm of the sediment. The tracers are simulated prognostically within a three-dimensional ocean circulation state. HAMOCC is coupled online to the Max Planck Institute ocean model (MPIOM) (Marsland et al. 2003; Jungclaus et al. 2013), which computes tracer advection and mixing. Temperature, pressure and salinity of MPIOM are used to calculate various transformation rates and chemical constants within HAMOCC. The treatment of important biogeochemical processes in HAMOCC, related to this study, are being described in some more detail in the following paragraphs. For more complete information on HAMOCC, see Ilyina et al. (2013) and Maier-Reimer et al. (2005).
Air-sea gas exchange is calculated for O_2, CO_2 and N_2. The air-sea CO_2 flux is a result of the partial pressure difference between atmosphere and water, multiplied by a gas exchange rate and solubility according to Weiss (1974) and Groeger and Mikolajewicz (2011). It is then divided by the actual thickness of the surface layer. The velocity of the gas transfer depends on the Schmidt number and prognostic wind speed at the surface (Wanninkhof 1992). The oceanic partial pressure of CO_2 (pCO_2) in the model is prognostically computed as a function of temperature, salinity, DIC, TA, and pressure. Biological processes are described by an extended NPZD (Nutrient-Phytoplankton-Zooplankton-Detritus) type model (Six and Maier-Reimer 1996). Primary production in HAMOCC is based on the co-limitation of phosphorous, nitrate and iron, as well as on temperature and radiation. The biogeochemistry related processes within the model are calculated on the basis of phosphorous. Associated changes between the remaining tracers are calculated using constant stoichiometric ratios (Redfield ratio following Takahashi et al. (1985), P:N:C:-O_2 ratio of 1:16:122:172). Phytoplankton is divided into silicifiers (opal shell) and calcifiers ($CaCO_3$ shell). It is assumed that silicifiers are preferentially produced as long as silicate is available, which is shown by several

observational studies (e.g., Lochte et al. 1993). Via prescribed vertical sinking rates opal, $CaCO_3$ and particulate organic carbon (POC) are transported to depth. During the sinking, the particles undergo remineralization at a constant rate, distributing silicate, DIC, TA and nutrients (while decreasing oxygen) at depth. Remineralization of POC depends on oxygen. If oxygen falls below a concentration of 0.5 μmol L^{-1} organic matter is decomposed by denitrification and sulphate reduction.
The formation of $CaCO_3$ shells consumes DIC and TA in a molar ratio of 1:2. The dissolution of $CaCO_3$ at depth is a function of the calcite saturation state (Ω) of sea water and a dissolution rate constant. Ω is calculated from Ca^{2+} concentration in sea water, which is kept constant at 1.03e-2 kmol m^{-3}, CO_3^{2-} (carbonate ion) concentration and the apparent solubility product of calcite, based on temperature and pressure. Dissolution of opal takes place continuously over the whole water column with a rate of 0.01 d^{-1}. Whereas $CaCO_3$ is less soluble in warm waters, the dissolution intensity of opal is positively correlated with temperature (Ragueneau et al. 2000).
The sediment module is based on Heinze and Maier-Reimer (1999) and Heinze et al. (1999). It basically calculates the same tracers as the water column model. The solid components of the sediment comprise opal, $CaCO_3$, organic carbon and chemically inert dust (referred to from here onwards as 'clay'). The liquid sediment components (pore water tracer) are DIC, TA, PO_4, O_2, N_2, NO_3, $Si(OH)_4$ and Fe. The tracer concentrations within the oceanic bottom layer and particularly the particle deposition from it determine the upper boundary for the sediment. The sediment reflects the uppermost 14 cm of the ocean floor and is resolved by 12 layers with increasing thickness and decreasing porosity from top to bottom. Below these layers, the model contains a diagenetically consolidated layer (burial). Major processes simulated in the sediment are vertical diffusion of porewater, decomposition of detritus, as well as dissolution of opal and $CaCO_3$.

2.2.2 Topography and grid

The model setup is based on the interpolation of a Late Paleocene 2°x 2° topography (Bice and Marotzke 2001) onto our 3.5°x 3.5° ocean model grid (Figure 2.1). It is used in several Paleocene-Eocene climate studies (Panchuk et al. 2008; Roberts et al. 2009; Heinemann et al. 2009; Zeebe 2012a). Main differences to present-day bathymetry lie in the open Central American Seaway, connecting the Atlantic and Pacific, as well as the existence of the Tethys Ocean and its connection to the Arctic Ocean, via Turgai strait. Although the Arctic Ocean has an additional link to the surrounding oceans, it lacks, unlike the present-day bathymetry, a deepwater connection. In the southern hemisphere, Drake Passage and Tasmanian Seaway are already open, but operate just as shallow water connections around Antarctica. The average ocean floor depth amounts to 3135 m (present-day setup: 3700 m) and has its deepest point at 5287 m (present-day

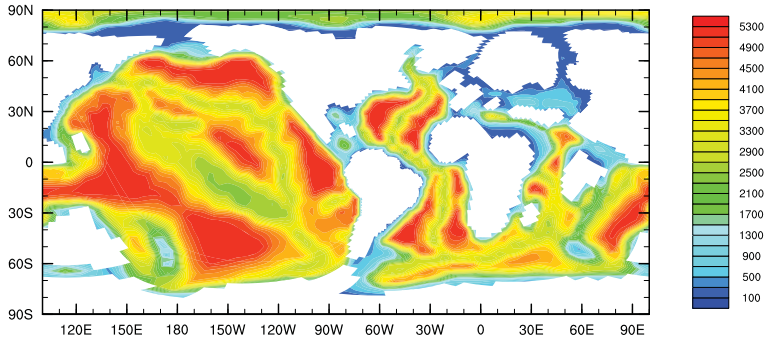

Figure 2.1: Paleocene topography (m depth).

setup: 5958 m) in the eastern equatorial Pacific. Vast areas of the Pacific are shallower in depths than in the modern ocean, the Atlantic is narrower than today and almost the whole Tethys does not exceed depths of 1000 m. It is mainly shaped by extended shelf areas. Taken into account these differences, the model bathymetry yields a 14 % reduced sea water volume, compared to today's ocean. Although, the missing ice sheets in the Late Paleocene setup would suggest an increase in oceanic volume, the provided bathymetry from Bice and Marotzke (2001) results in a reduced ocean volume compared to modern conditions. However, since we adapt the inventories of the ocean biogeochmical tracers (see 'Initialization biogeochemistry'), we hold on to the reduced ocean volume bathymetry, since it allows a better comparison of the results to other models using the same bathymetry (e.g., Panchuk et al. 2008; Heinemann et al. 2009). In the conducted simulations HAMOCC integrates with a time step of 2.4 hours (0.1 days). The horizontal resolution of the ocean model is 3.5°x 3.5° which equals a grid spacing from 70 km around South America to 430 km in the Pacific. The ocean model has 40 vertical layers, with increasing level thickness with depth: 9 layers are covering the upper 100 m and 23 layers the upper 1000 m of the water column. An orthogonal curvilinear grid is applied, with the poles located over northern Eurasia and South America to achieve best grid resolution for all ocean regions.

2.2.3 Forcing

The ocean stand-alone model approach requires an atmospheric forcing. We use a Late Paleocene climate with an atmospheric CO_2 concentration of 560 ppm, which is mimicked by an adequate atmospheric forcing, derived from Heinemann et al. (2009). The atmospheric conditions used in this study were calculated with a coupled climate model using ECHAM5, MPIOM and JSBACH in Paleocene-Eocene boundary conditions (560 ppm CO_2). Atmospheric methane and nitrous oxide were set to pre-industrial values.

The model showed after 2300 years of integration an equilibrium state in atmospheric and oceanic conditions (Heinemann et al. 2009). From the atmospheric model output we take 30 consecutive years from which we reproduce a daily mean Late Paleocene atmospheric forcing, based on the Ocean Model Intercomparison Project (OMIP) forcing used for present-day ocean-model-only setups (Roeske 2006). The model is then forced using daily heat, freshwater and momentum fluxes in a 30 year cycle.
We initialize the stand-alone ocean model (MPIOM) based on the result of the 2300 years Late Paleocene equilibrium run by Heinemann et al. (2009). Additionally, we define a Paleocene climatology for ocean temperature and salinity from the same data. It displays the monthly mean climatological state for the two variables, averaged from daily data over a 30 year period. Sea surface salinity (SSS) and SST (upper 12 m) in our model are relaxed towards this Paleocene based climatology. Relaxation is taking place with a time constant of 180 days, it takes about 3 months till the surface layer is restored completely to the climatology.

2.2.4 Initialization of biogeochemistry

Using the MPIOM physical ocean state, we spin up HAMOCC starting from basin-wide-homogeneous distributions of biogeochemical tracers, taking pre-industrial concentrations as a rough orientation for spatial and vertical tracer distributions. We reduce the oceanic carbon inventory (from ∼38500 Gt to ∼32000 Gt), as well as the different nutrient pools, proportional to the 14 % reduced ocean volume in the Late Paleocene setup. The reduction results in tracer concentrations close to modern values in the water column.
The model is integrated for 3200 years, periodically repeating the forcing (see section 2.3), while the inventories of TA are adjusted to the CO_2 level of 560 ppm. Fluxes and tracer distribution stabilize after about 1000 model years within the water column. The distributions of tracers are not restored to any kind of data set, to be consistent with the biological, chemical, and physical dynamics of the model.
Since for the Late Paleocene the monthly mean dust deposition fields are not available (pers. com. A. Winguth), we prescribe a spatially homogeneous input of dust at the sea surface. The total amount of annual bio-available iron deposition to the ocean is the same as in the modern ocean setup (∼38 e+7 kg Fe yr^{-1}; Mahowald et al., 2005). Besides the inventory adaptation and homogeneous dust deposition, the ocean chemistry in the Late Paleocene simulations is modeled the same as in modern MPI-ESM (Ilyina et al. 2013).
The weathering fluxes depend on the long-term sedimentation rates. It is used for balancing the water column inventory of the calcite, silicate and OM pools. The annual amount which is leaving the system through sedimentation, is added (globally distributed) at the surface again. The calcite weathering varies between 0 and 900 kmol

Model parameters		
	pre-industrial (CMIP 5)	**Late Paleocene**
Atmospheric CO_2 (ppm)	278	560
Ocean volume (10^{18} m^3)	1.353	1.164
Ocean temperature surface (℃)	9.6	24.8
Ocean temperature at 4000 m depth (℃)	1.4	8.9
Ocean salinity	34.67	34.31
Inventories		
Carbon (10^3 Gt)	38.5	32.0
Phosphate (10^{12} kmol)	2.73	2.48
Silicate (10^{14} kmol)	1.64	1.88
Nitrate (10^{13} kmol)	3.44	2.84
Weathering		
Global input of CaCO3 (Tmol yr^{-1})	28.4	22.1
Global input of opal (Tmol yr^{-1})	6.5	0
Global input of POC (Tmol yr^{-1})	0	0.1
Primary production		
Global (Gt C yr^{-1})	61.14	58.65
Export production		
CaCO3 (Gt C yr^{-1})	0.89	0.63
Opal (Tmol Si yr^{-1})	118.24	159.57
POC (Gt C yr^{-1})	8.72	8.54
Molar export ratio		
C(CaCO3):Si(opal)	0.63	0.33
C(CaCO3):C(POC)	0.1	0.07
Si(opal):C(POC)	0.16	0.22
N-cycle		
N_2 fixation (Tmol N yr^{-1})	14.89	22.33
Denitrification (Tmol N yr^{-1})	14.53	21.18

Table 2.1: Globally integrated values of biogeochemical parameters calculated with the model HAMOCC for the pre-industrial (CMIP5, Ilyina et al. 2013) and the Late Paleocene.

C s^{-1}. Silicate weathering varies between 0 to 650 kmol Si s^{-1}, and organic material varies from 0 to 4 kmol C s^{-1} during the spinup. After establishing an equilibrium state in the sediment, constant weathering fluxes are applied, as showed in Table 2.1.

2.2.5 Initialization of sediment

We initialize the sediment with 100 % clay, while the $CaCO_3$, opal and organic carbon sediment pools start filling from first year on. While these long spin up simulations (50 kyr) have been done for present-day (e.g., Heinze et al. 1999), they do not exist for the Paleocene configuration. However, in matter of computing time it is not feasible to spin up the sediment module and achieve an equilibrium state within a realistic time frame. To circumvent this problem we use a computational method to accelerate processes within the sediment module of HAMOCC. In the sediment module, the sediment layers are subdivided into a solid sediment fraction and a porewater fraction. The fraction of solid sediment varies with depth, but not with time. The downward shifting of particles depends on the âfillingâ state of the sediment. For the sediment acceleration we simply divide the volume fraction of solid sediment and porewater by a prescribed factor, while keeping the sediment thickness constant. As a result, the surface area of the sediment is reduced relating to its vertical profile. From a modeling perspective this reduction in volume (area) is acceptable, since the proportion of the single grid cells (100 km x 15 cm) prevents horizontal gradients, anyway. By maintenance of mass conservation the tracers are distributed faster throughout the sediment, since the volume is reduced and the material is shifted faster to deeper layers. To prevent an overcompensation of the porewater, the diffusion has to be reduced by the same factor as the volume is reduced. As soon as the sediment is saturated and in equilibrium, the sediment module is extended to its original volume (area) again. This sediment acceleration is turned on in year 1350, after having the water column tracers in an equilibrium state. The run proceeds using an acceleration factor of 1000. After approximately 150 years, the net-fluxes at the ocean-sediment boundary are strongly reduced and the sediment acceleration is turned off. In this way, accumulation of the sediment pool is equivalent to ∼150,000 years of integration.

2.3 Late Paleocene climate state

The Late Paleocene climate state in our simulation is characterized by a global annual mean temperature of 23.56 ℃ (at 2 m height), using the atmospheric forcing described above (for comparison see Lunt et al. 2012). Maximum annual average temperatures are reached along the equator over Africa, Asia and South America with temperatures close to 40 ℃ (Figure 2.2). The absolute annual average heat maximum lies over southern Asia (42.1 ℃). Southern high latitudes (-1 ℃ at 90° south) are in annual average around 4 ℃ colder than northern high latitudes (3 ℃ at 90° north).

The prescribed wind forcing displays similar patterns as in the pre-industrial setup (not shown). However, the variability of Late Paleocene winds is much stronger than the variability of the pre-industrial state. Highest variability is found in the storm-

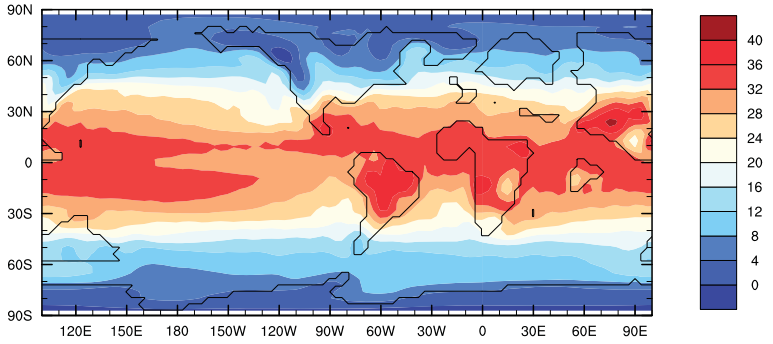

Figure 2.2: Forcing field: annual mean atmospheric temperature (℃) at 2 m height.

track regions in higher latitudes, while around the equator winds are comparable to pre-industrial. The atmospheric climate state has been evaluated in an earlier study using the same model version by Heinemann et al. (2009).
The ocean has a mean temperature of 14.68 ℃ (pre-industrial: 5.61 ℃) and a global annual mean SST of 24.78 ℃, which is in agreement with results of other climate models (Lunt et al. 2012). The northern high latitudes reach maximum SST's of 12.78 ℃ in northern hemisphere summer (JJA), but the sea surface of the Central Arctic Ocean does not get warmer than 4 ℃. The southern high latitudes show maximum SST's of 17.83 ℃ in austral summer (DJF). In the presented setup there is no sea ice occurring, in each hemisphere winter the ocean stays completely ice free. The simulated high latitudes SST is in general agreement with the reconstructions for the Southern Ocean (Thomas et al. 2002), but do not fit the extreme proxy data assumptions of Sluijs et al. (2006) for the Arctic Ocean (for further discussion, see Heinemann et al. 2009). The meridional cross sections of the Pacific and the Atlantic Ocean (Figure 2.3) differ from each other in their vertical temperature profiles. While the Atlantic features homogeneous relatively warm temperatures over largest parts of the water column, the temperature gradient in the Pacific is much more pronounced. Differences in deep sea temperatures reach up to ∼5 ℃ between the two basins. While deep sea temperatures for the Atlantic (13 ℃) are in line with proxies (Tripati and Elderfield 2005), the deep Pacific (8 ℃) seems comparatively cold.

The Late Paleocene ocean in our simulations has a mean salinity of 34.31 (pre-industrial: 34.67) and a mean SSS of 33.77. Within the subtropics regions of elevated SSS around 36 emerge, while higher latitudes show generally lower values (Figure 2.3). The Atlantic Ocean has the highest SSS, here the annual mean surface salinity amounts to 35.06 and maximum salinities of 36.9 in the North- and 37.4 in the South Atlantic are reached. The upper 1000 m of the basin reveal the advection of more saline waters from the Tethys, around 30° north and less saline waters from the Southern Ocean. In

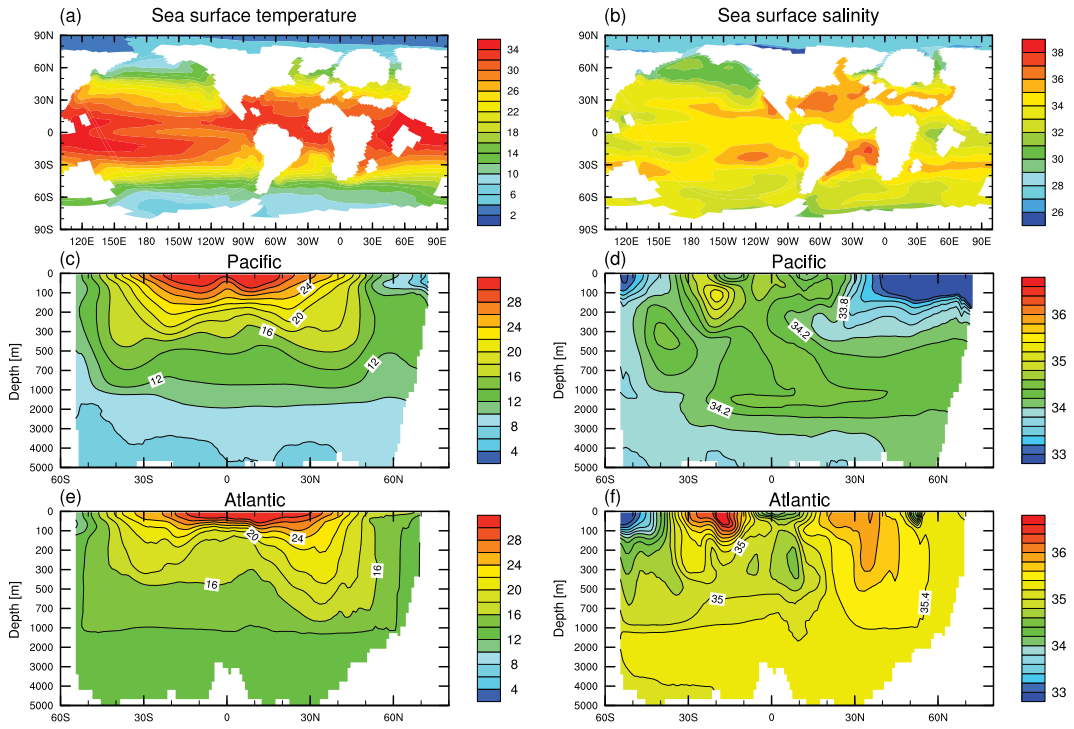

Figure 2.3: Sea surface temperature (°C) (left) and salinity (right); for the surface (a,b), Pacific (c,d), and Atlantic (e,f) averaged meridional cross cut. Note the non-linear vertical axes, used to zoom in the upper ocean layers.

depth >1000 m the Atlantic basin salinity is characterized by homogeneous distributions, except the small tongue of slightly less saline Antarctic Bottom Water (AABW) extending until 20° south (Figure 2.3), mirroring the weak vertical mixing and hence strong stratification. The Pacific is much more heterogeneous in terms of vertical salinity distribution. In the northern Pacific the Arctic inflow of water causes very low surface ocean salinities up to 30° north. The southern hemisphere and even parts of the northern deep Pacific are dominated by less saline AABW. The inflow of Atlantic water via the Central American Seaway (strongest net-inflow in the uppermost 100 m) is causing the highest salinities in the Pacific (Figure 2.3). Here the more saline waters descend and are then transported northward. This gradient between southern (low salinity) and northern (high salinity) Pacific shapes the vertical salinity profile. The Arctic Ocean's mean surface salinity amounts to 27.13. This low salinity is interpreted as an effect of freshwater inflow due to an intensified hydrological cycle in a warmer atmosphere and as an effect of the shape of the ocean basin. Low surface salinities and a poor ventilated water column are also derived from proxy data (Pagani et al.

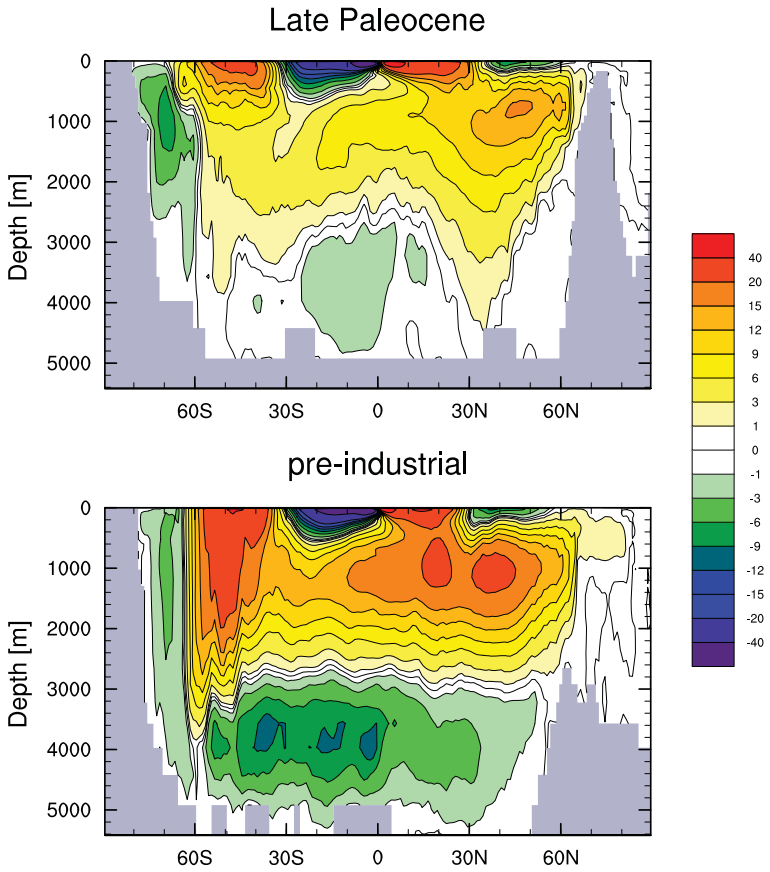

Figure 2.4: Globally averaged meridional overturning circulation (Sv), for the Late Paleocene (top) and the pre-industrial (bottom). Positive values corresponds to clockwise circulation. Pre-industrial values were calculated within CMIP5 experiments.

2006b; Waddell and Moore 2008). The bathymetry prevents any deepwater exchange with the surrounding oceans and hence contributes to a sharper stratification of the Arctic Ocean and its low salinity cap. There is no additional amplifying mechanism for mixing of Arctic waters due to the absent sea ice formation and consequent brine production.

Salinity and temperature profiles are mainly shaped by the meridional overturning circulation (MOC) (Figure 2.4). The large-scale circulation structures are generally similar to modern conditions, but the Late Paleocene Atlantic is dominated by just one large scale circulation cell in our simulation (spreading nearly over the whole basin up to a depth of 4000 m), causing more homogeneous temperature and salinity distributions. The Atlantic Ocean lacks an AABW cell, while the AABW formation and spreading are much more pronounced in the Pacific.

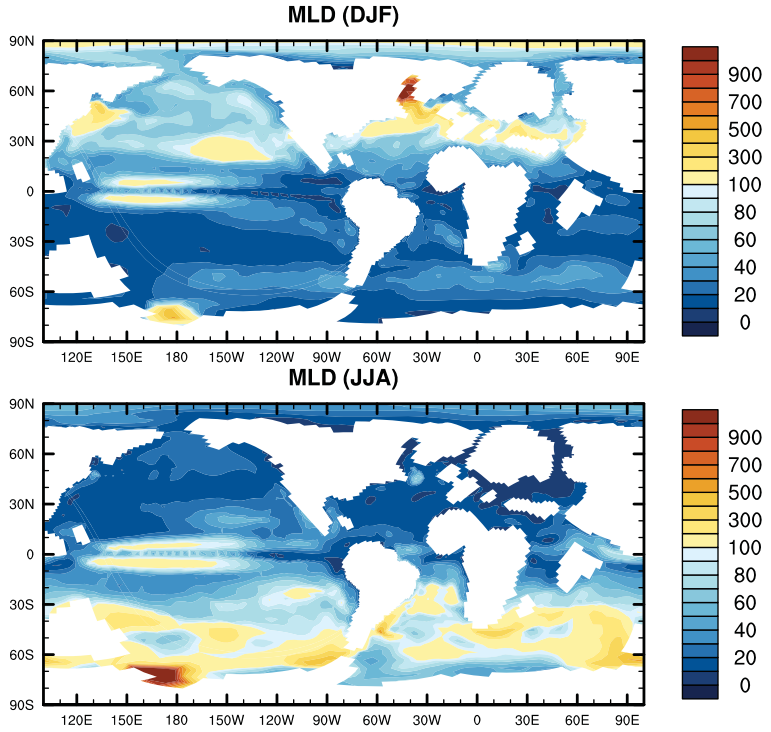

Figure 2.5: Mixed Layer Depth (m) averaged over boreal winter (DJF) and boreal summer (JJA).

Here formation of deepwater occurs at 70° south. No further overturning takes place in the northern Pacific, as salinity concentrations in the surface ocean are too low, due to the Arctic Ocean water inflow. The Late Paleocene climate causes the ocean to be warmer on average (compared to pre-industrial conditions), leading to increased stratification throughout the water column. The reduced equator to pole temperature gradient results in a further slowdown of the MOC. Maximum deepwater formation (for depth >900 m) of ∼15 Sv occurs in the Southern Ocean and the North Atlantic (Figure 2.4). Southern Ocean sinking occurs in the Ross Sea, similar to other Paleocene-Eocene simulations (Sijp et al. 2014), whereas the North Atlantic deepwater source is not produced in all models.

In MPIOM the mixed layer depth (MLD) is defined as the depth, where in situ density exceeds surface water density by more than 0.125 kg m^{-3} (sigma-t criterion). The annual global mean MLD in the Late Paleocene setup levels at 52 m depth. Observations suggest an annual global mean of 65 m for MLD in present-day oceans (de Boyer Montegut et al. 2004). Since the MLD is interpreted as an indicator for the stratification of the ocean, which apparently is stronger in a warmer climate (e.g., Wetzel et al. 2006),

the reduced MLD appears to be an expected result of our model simulation. As shown in Figure 2.5 the MLD has a strong seasonal signal. In boreal winter deepwater formation is taking place in the North Atlantic. In austral winter the same deepening of MLD as an effect of convectional processes occurs in the South Pacific.

2.4 Late Paleocene ocean biogeochemistry

2.4.1 Air sea exchange processes

In this study we aim at achieving steady-state conditions with respect to ocean biogeochemistry, in accordance with a long-term warm climate. Corresponding to the expectation of an equilibrium climate state, the annual mean CO_2 flux at the atmosphere-ocean boundary is balanced around zero. The global annual mean of surface ocean pCO_2 is 560 ppm within the Late Paleocene model setup. It shows highest values along the equator and in the eastern boundary currents, along South America in the Pacific, and Africa in the Atlantic (Figure 2.6), similar to present-day (Takahashi et al. 2009). While the general spacial distribution of pCO2 is mainly defined by temperature and salinity, the high pCO_2 areas in the equatorial and coastal areas result from upwelling of high pCO_2 and nutrient rich waters from mid ocean depth.
The Atlantic Ocean is the major net-emitter of CO_2 with an annual outgassing of 0.41 Gt C, while the Pacific Ocean balances its net-fluxes around zero over the year. While high oceanic pCO_2 is associated with carbon release to the atmosphere, oceanic CO_2 uptake occurs in regions with low pCO_2 (if pCO_2oce $<$ pCO_2atm). The model computes lowest pCO_2 around Antarctica, especially close to Drake Passage, which corresponds to low salinity and TA concentrations in this area. Nevertheless, nearly the whole Southern Ocean (40°-80° S) is characterized by pCO_2 values below the atmospheric CO_2 concentration of 560 ppm. This is consistent with deepwater formation and the deep MLD in austral winter in the Southern Ocean. Another prominent zone of low pCO_2 is located between 50° and 80° N, with its maximum in the North Atlantic and the North Pacific. Summarized over the whole year, the Arctic Ocean acts as a CO_2 sink (net-uptake of 0.06 Gt C). However, it plays a minor role in carbon uptake compared to present-day, due to the reduction in surface area of 40 % and increased ocean temperature. Instead, the Indian Ocean becomes the major driver in CO_2 net-uptake (0.31 Gt C yr^{-1}). The southern part of the Indian Ocean is influenced by a deep mixed layer in austral winter (>200m), but even parts of the northern Indian Ocean show a MLD of up to 80 m, resulting in rather low pCO_2 values in the Indian Ocean surface waters. Consistent with the solubility effect, which declines with rising temperature (Weiss 1974), our model shows that the equatorial regions in the Late Paleocene acted as a source for CO_2, while the high latitudes operate as a CO_2 sink. This matches the present-day simulations with HAMOCC (Ilyina et al. 2013), but during the Late Paleocene it is mainly the CO_2 uptake of the Indian and Southern Ocean which compensates for the CO_2 outgassing in the Atlantic.
Globally, the high ocean temperatures lead to a reduced solubility of CO_2 in the surface ocean, compared to pre-industrial conditions. Moreover, the transfer of CO_2 from the surface to intermediate and deep waters, by the oceanic velocity field is reduced

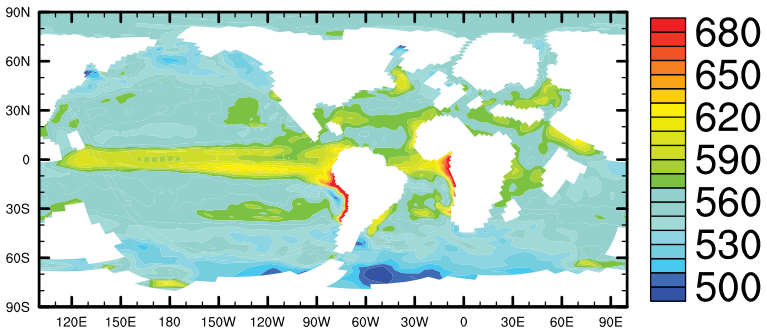

Figure 2.6: Annual mean surface ocean pCO_2 (ppm).

by the more sluggish circulation in the Late Paleocene compared to the pre-industrial simulation (Figure 4). The sluggish circulation together with the weak ocean solubility pump, would act to reduce the ocean's uptake capacity of atmospheric CO_2 in response to the carbon perturbation during the PETM.

2.4.2 Biological production & nutrients

Phosphate concentrations in the surface ocean show pronounced latitudinal gradients and weaker basin to basin differences in the Late Paleocene simulation. High phosphate concentrations characterize the surface ocean in the southern high latitudes, equatorial Pacific and Atlantic, as well as in northern hemisphere mid latitudes (Figure 2.7). Strong equatorial upwelling of water masses in Atlantic and Pacific as well as moderate upwelling along the western coasts and in the Southern Ocean cause a maximum in phosphate surface concentrations in these regions. All other regions are characterized by phosphate-depletion, with the Atlantic and the Pacific gyres revealing the lowest phosphate concentrations in subtropical surface waters. Moreover, our simulation reveals a strong depletion in nutrients in the Arctic surface ocean, as a result of the interaction between bathymetry, stratification and freshwater input.

Generally, the phosphate and nitrogen cycle are treated very similar in the model, since they are connected via the Redfield ratio. However, bacterial processes such as nitrogen fixation and denitrification cause deviations between nitrate and phosphate distributions. In oxygen depleted zones denitrifying bacteria provide oxygen for remineralization, representing an additional sink for nitrate in these regions. In the Late Paleocene simulation intense oxygen minimum zones (OMZ) lead to low nitrate concentrations in the eastern boundary currents of the Atlantic and the Pacific. In global average the denitrification is ∼45 % higher than in the simulation for the pre-industrial climate state (Table 2.1). The increased denitrification originates from the low oxygen concentrations in mid ocean depth, which are induced by the reduced mixing of water

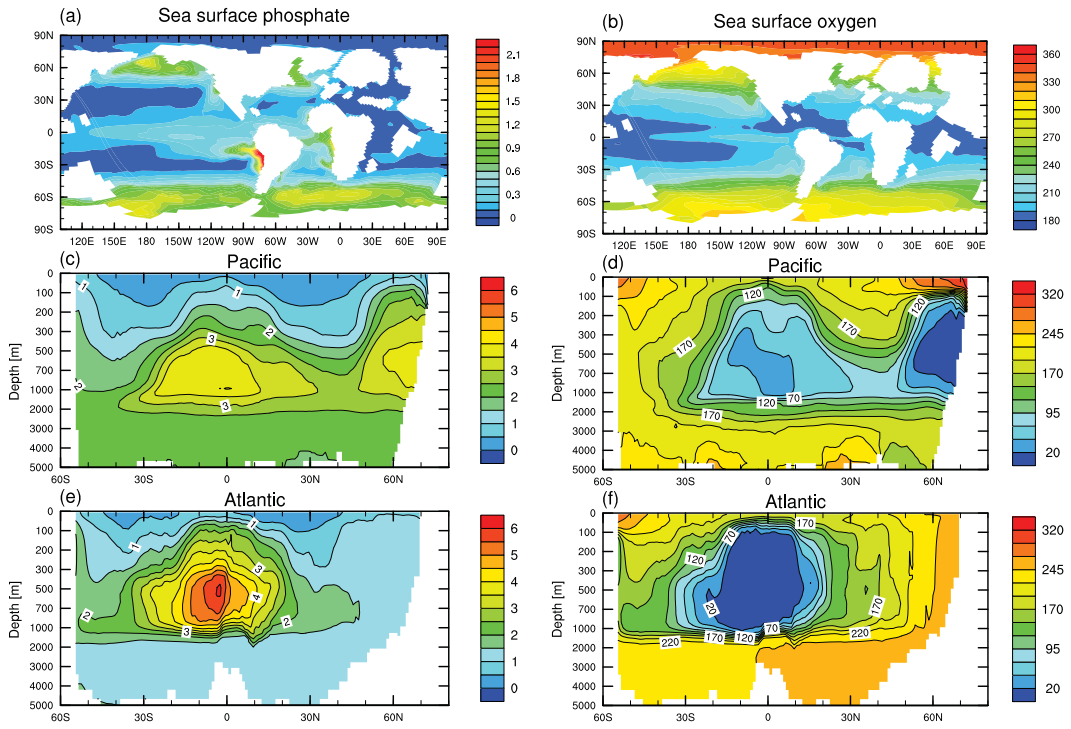

Figure 2.7: Phosphate (left) and oxygen (right) concentrations (both in μmol L^{-1}); for the surface (a,b)), Pacific (c,d), and Atlantic (e,f) averaged meridional crosscut. Note the non-linear vertical axes, used to zoom in the upper ocean layers.

masses during the Late Paleocene. Nitrogen fixation occurs in areas where the ratio of nitrate to phosphate is lower than the (constant stoichiometric) value of $R_{N:P}$. This is primarily in the tropics, the North Pacific and the North Atlantic. Likewise, also nitrate fixation is higher in the Late Paleocene than in the pre-industrial climate state. The gradient in surface ocean nutrient concentrations between low and high latitudes in the southern hemisphere resembles the modern one, despite the homogeneous dust/iron concentration prescribed for every grid cell. This indicates that the dust climatology is not producing a strong signal in higher latitudes. Hence, in our Late Paleocene setup the iron limitation is not the major driving mechanism for preventing the surface ocean from complete consumption of nutrients, making the physical conditions at the poles accountable for it.

Surface oxygen concentration decreases from pole to equator, confirming its strong temperature dependency (Figure 2.7). Generally higher SST than in modern conditions lead to slightly lower oxygen concentrations in the surface oceans. Only in the Arctic Ocean the low salinity is counteracting the temperature effect, as salinity is inversely

related to oxygen solubility in seawater, according to Weiss (1970). This leads to similar oxygen concentrations/solubility like in the present-day setup.
While the physical dynamics and the export production of particulate organic carbon determine the surface concentrations of nutrients, the distribution of nutrients at depth is controlled by remineralization (Maier-Reimer 1993). Modern nutrient and oxygen concentrations in the Pacific and Atlantic mirror the different age of the deepwater, defined by the global thermohaline circulation. In the Late Paleocene simulation the upper 1000 m of the water column reveal the maximum in phosphate concentrations in both basins, resulted by strong remineralization of organic matter, whereas the phosphate concentrations at depth are rather a product of global ocean circulation, then in situ remineralization. This explains the lower phosphate concentrations in the Atlantic over the Pacific, although OM export rates (in units per area) and oxygen concentrations are higher in the Atlantic. The oxygen concentration in Pacific deepwater is highly increased (Figure 2.8), compared to modern conditions, which can be attributed to Southern Ocean deepwater formation and an enhanced exchange of Pacific and Atlantic through the Central American Seaway.

The OMZ's are very pronounced within the upper 1000 m in both basins. Oxygen concentrations are as low as 20 μmol kg-1, in meridional average, along the equatorial Atlantic and the North Pacific. The prominent OMZ's are attributed to the existence of productive equatorial zones (Figure 2.9) (Norris et al. 2013) and reduced mixing in a more stagnant ocean during the Late Paleocene. For the Atlantic the low oxygen concentrations along the equator are even intensified in the meridional average, due to an additional high productivity zone along the northern continental margin of South America. In general the Atlantic shows an increase in OM export (in units per area) of nearly 60% in comparison to pre-industrial. Although, the total export just increased by 13%, due to the reduced area of the Atlantic in the Late Paleocene setup. However, the simulated OMZ's might be somewhat overestimated as illustrated in CMIP5 simulations. The model produces lower than observed oxygen concentrations, spreading over larger areas in the equatorial Pacific and along the western continental margin of Africa (Ilyina et al. 2013), which is typical for other global models as well (Andrews et al. 2013; Cocco et al. 2013).

The annual global primary production amounts to ∼59 Gt C (Table 2.1) in the Late Paleocene simulation. The coastal upwelling regions along the western continental margins, as well as the equatorial regions of the Pacific and the Atlantic tend to be the dominant mechanism fueling primary production (Figure 2.9). Compared to modern conditions, the production along the eastern boundary currents in Atlantic and Pacific is less pronounced. However, resulting from the open Central American Seaway, strong production arises along the northern tip of South America. The mid latitudes (nutrient poor mid latitudinal gyres) and the Arctic Ocean exhibit sparse productivity. On the contrary the nutrient rich Southern Ocean is responsible for ∼11 % of the global

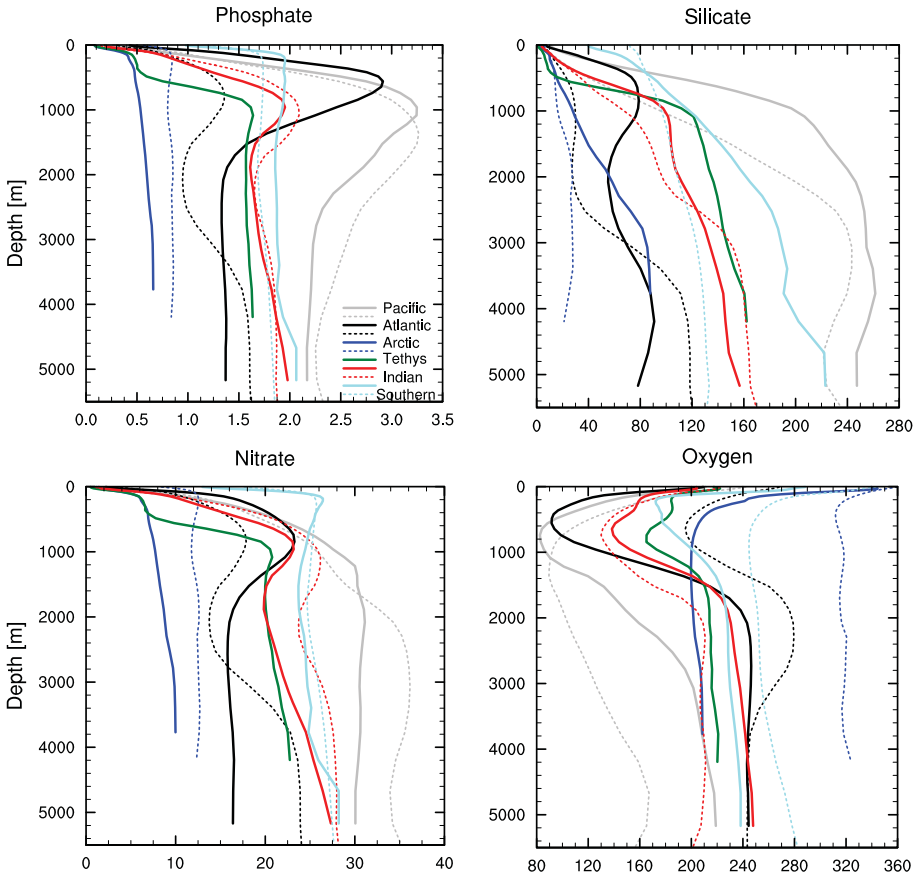

Figure 2.8: Globally averaged vertical profiles of phosphate, silicate, nitrate and oxygen (all in μmol L^{-1}). Solid lines show Late Paleocene distributions, dotted lines show pre-industrial concentrations calculated within CMIP5 experiments.

primary production.

The production of calcite shells follows the low silicate surface concentrations in the Atlantic, Tethys and Indian Ocean, as well as in the western equatorial Pacific. Regions of higher silicate concentrations which correspond to upwelling locations, are dominated by production of opal shells as implied from our modeling approach.

The export production of $CaCO_3$ is with 0.63 Gt C yr^{-1} lower than for pre-industrial conditions (see Table 2.1). This leads to a $CaCO_3$: POC export ratio of 0.07, contrary to the PETM simulations of Panchuk et al. (2008) and Ridgwell and Schmidt (2010) suggesting a ratio of 0.2. As the $CaCO_3$: POC rain ratio is an important source of uncertainty, controlling the sedimentary $CaCO_3$ wt% distribution, Panchuk et al. (2008) base their suggestion on an ensemble run using different export ratios. Finally,

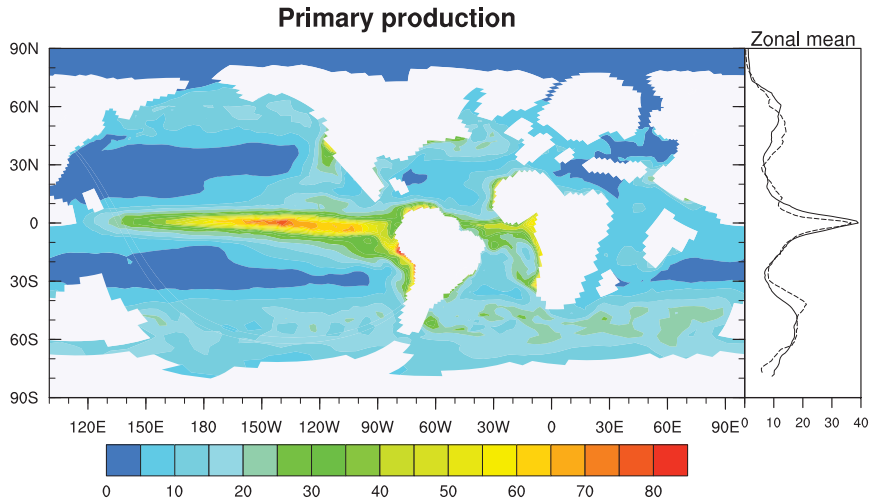

Figure 2.9: Annual mean primary production plotted as map and zonal average (both in mol C m^{-2} yr^{-1}). The zonal average plot shows the primary production for the Late Paleocene (solid line) and the pre-industrial (dashed line).

0.2 matches best their pre-PETM CCD (3.5-4 km depth) and $CaCO_3$ sediment distribution. Simulations for present-day export ratio suggest that the ratio levels more around 0.1 (∼0.06 Sarmiento et al. (2002); ∼0.1 CMIP5 runs MPI-ESM; <1.4 Ridgwell and Schmidt (2010)). In our simulation the $CaCO_3$: POC export ratio is a result of production, remineralization and sinking velocity. Because dissolution of opal is positively correlated with temperature, in a warmer ocean more silica is available for opal production in the upper ocean (Figure 2.8). This indirectly results in less $CaCO_3$ formation in our model set up. The homogeneous dust (iron) climatology can not cause a shift from $CaCO_3$ towards opal producing skeletons. Thus it can only lead to an absolute increase in production of former iron-limiting low productivity zones, but not change the proportions between the two building materials.
An interbasinal comparison reveals increased overall export fluxes in the Atlantic. Opal, $CaCO_3$ and POC export (in units per area) even exceed the ones in the Pacific. However, in absolute numbers the Pacific Ocean is the main driver, covering about 50 % of the global ocean surface area it is responsible for >50 % of POC export (4.55 Gt C yr^{-1}), globally. The strong depletion in silica in Tethys surface waters (Figure 2.8) favours high $CaCO_3$ production. As a consequence parts of the Tethys ocean shows low surface TA. The Tethys has just a minor impact on the strength of the biological carbon pump, exporting 0.28 Gt C yr^{-1}.

2.4.3 Carbonate chemistry

TA concentrations decrease from the equator towards the poles, with the subtropical gyres showing both, elevated DIC and TA, compared to the surrounding surface waters (Figure 2.10). The spatial patterns of surface ocean DIC and TA reproduced by the model are similar to pre-industrial conditions. Highest DIC concentrations, besides the gyres, are located in the Southern Ocean (2100 μmol kg^{-1}) whereas the Arctic Ocean exhibits low DIC concentrations around 1800 μmol kg^{-1}. While the SST determines mainly the surface distribution of DIC, the surface TA is rather reflecting the structure of salinity (Maier-Reimer 1993), which is shaped by the precipitation-evaporation gradients, leading to increased TA concentrations in the subtropics. Low salinity in the Arctic Ocean, induced by strong vertical stratification and the low exchange with the surrounding oceans (no deep-water exchange) is driving the TA to very low values (<1800 μmol kg^{-1}). High SST, low TA, and little CO_2 uptake in the Arctic Ocean result in generally low DIC concentrations over the whole water column, reducing the Arctic Ocean's carbon storage capacity.
The surface seawater CO_3^{2-} concentration is shaped by the elevated atmospheric CO_2 concentration of 560 ppm. Higher atmospheric CO_2 concentrations do not have an impact on TA, but cause a shift from CO_3^{2-} to HCO_3^- (bicarbonate). The reduced CO_3^{2-}:DIC ratio which is characterizing the pre-PETM carbonate chemistry is reducing the oceanic buffer capacity towards atmospheric CO_2 perturbations.
In the vertical profile the maximum in DIC concentration around the equator, spreading from 400 to 1000 m depth (Figure 2.10), is related to biological processes. It marks the depth in which intense dissolution and denitrification of the exported particles takes place. The aerobic remineralization of POC is releasing DIC and consuming oxygen, while at the same time the dissolution of $CaCO_3$ and the denitrification is increasing the TA at ∼1000 m depth (Figure 2.10). That the subsurface Atlantic (up to 1000 m depths) exhibits higher TA and DIC concentrations over the Pacific can be explained by the stronger export of $CaCO_3$ and POC (in units per area). In the uppermost layers of the ocean, the difference in CO_3^{2-} concentration between Atlantic and Pacific is not evident anymore. The atmospheric CO_2 concentration of 560 ppm causes low CO_3^{2-} concentrations, reaching up to a depth of 600 m in both oceans. In layers beneath 2000 m the CO_3^{2-} concentrations within the basins show homogeneous distributions, with the Atlantic CO_3^{2-} concentrations (100-120 μmol kg^{-1}) being nearly twice as high as in the Pacific (60-70 μmol kg^{-1}).
The calculated global average pH in the surface ocean amounts to 7.9, which is in agreement with the estimate by Tyrrell and Zeebe (2004) and close to the suggestion of Ridgwell and Schmidt (2010), that Late Paleocene pH surface values were ∼0.4 lower than today. The surface distribution in pH displays a similar pattern as we know from pre-industrial pH, albeit at lower values. Within the upwelling areas along the equa-

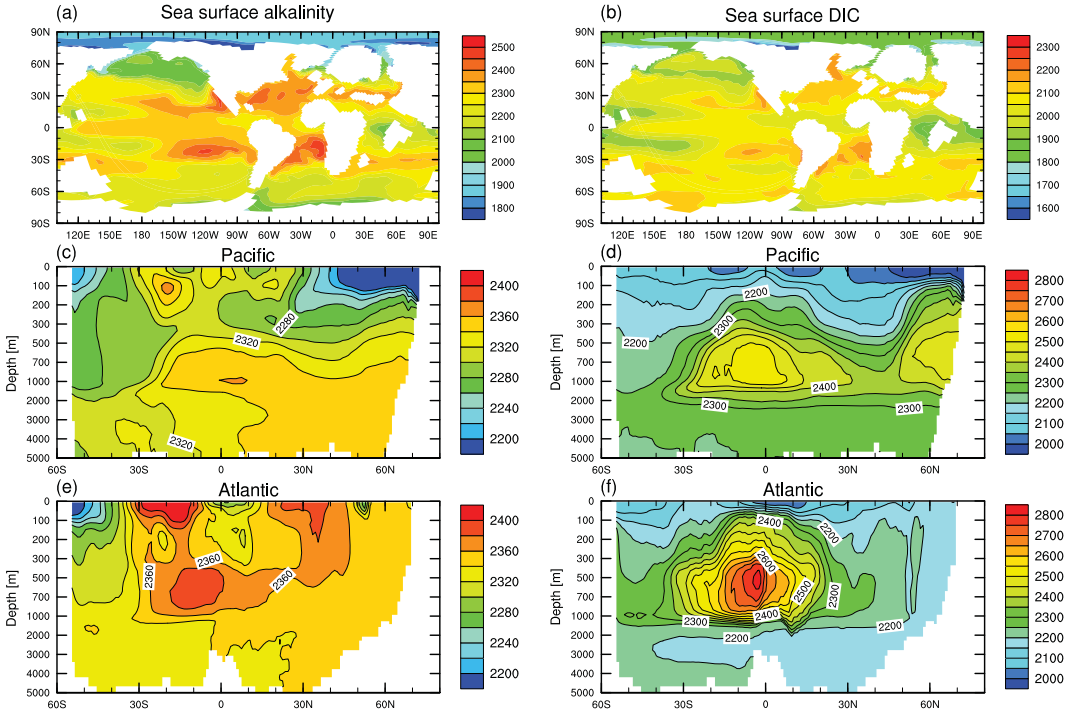

Figure 2.10: TA (left) and DIC (right) concentrations (both in μmol kg^{-1}); for the surface (a,b)), Pacific (c,d), and Atlantic (e,f) averaged meridional crosscut. Note the non-linear vertical axes, used to zoom in the upper ocean layers.

tor and in front of the western continental margins the pH is lower than in the mid latitudes. The Arctic Ocean shows particularly low pH, correlated to the very low salinities.

At depth large parts of the Pacific are undersaturated with respect to $CaCO_3$ (Figure 2.11). However, the undersaturation is characterized by a strong gradient in the east-west direction, which is not evident in the zonally averaged Ω values (Figure 2.11). The basin wide undersaturation in the Pacific starts below a depth of 3700m. The horizontal gradient in Ω is even enhanced by inflow of CO_3^{2-} rich water from the Indian Ocean and undersaturated (Ω <1) near-surface waters in the eastern part of the basin. Undersaturation occurs due to biological respiration processes in intermediate waters, which correlate to very low pH values of up to 6.9, computed for the uppermost 1000 m of the water column within the equatorial Pacific.

The elevated ocean temperatures during the late Paleocene produce a lower CO_3^{2-} saturation concentration, because it inversely depends on temperature. This should lead to an increased Ω, in comparison to present-day, as formerly discussed in Zeebe and Zachos

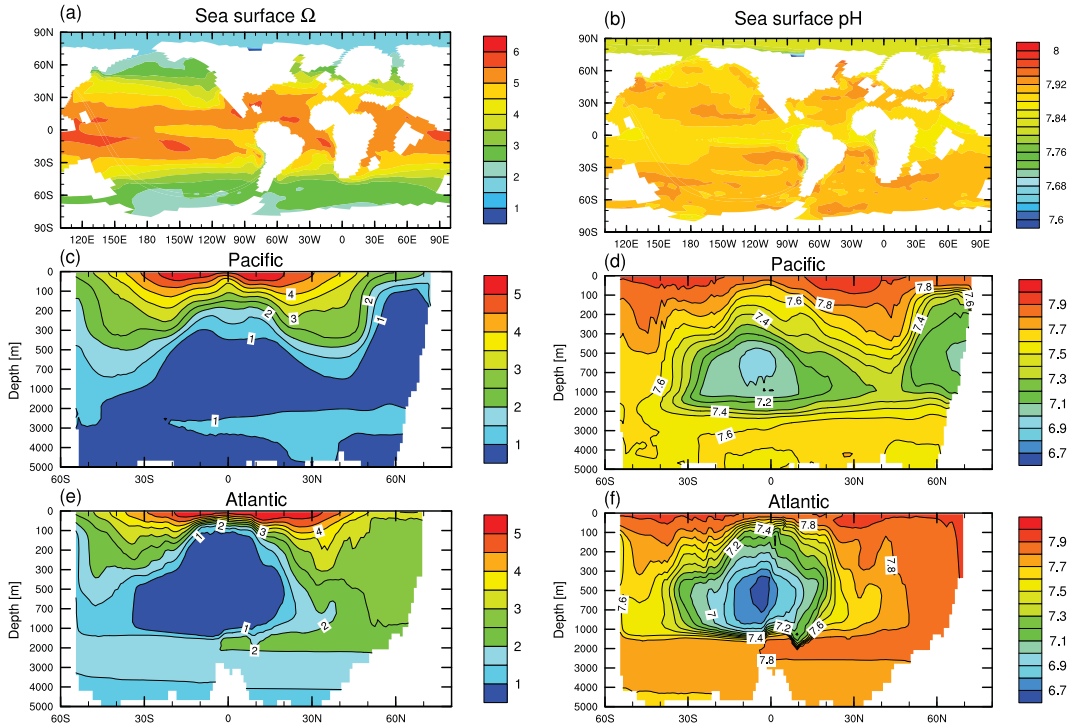

Figure 2.11: Ω (left) and pH (right); for the surface (a,b)), Pacific (c,d), and Atlantic (e,f) averaged meridional crosscut. Note the non-linear vertical axes, used to zoom in the upper ocean layers.

(2007). This effect is strong in the Atlantic, which is at depth in average around 5 °C warmer than the Pacific in our simulation. Here, a reduced calcite saturation concentration counteracts the lower CO_3^{2-} concentrations. The undersaturation with respect to CO_3^{2-} in the equatorial Atlantic between 200-1000 m depth is a result of very low pH in the low latitudes subsurface ocean, caused by aerobe and anaerobe remineralization (Figure 2.8). The North Atlantic and the Indian Ocean show no undersaturation with respect to $CaCO_3^{2-}$ at all.

Our approach provides Ω distributions being consistent with the 3-d hydrodynamical field and the biogeochemical processes as simulated for the Late Paleocene ocean. We perceive a complex pattern of Ω, which includes e.g. undersaturated waters in shallower depth overlying supersaturated waters in deeper layers, as seen in the Pacific in our simulation. Local undersaturation might be of importance since 60 to 80 % of the $CaCO_3$ export is dissolved already in the upper 1000 m of the water column, as shown by present-day studies (Feely et al. 2004; Ilyina and Zeebe 2012). The assumption of a uniform basinwide saturation horizon (depth where Ω=1) or lysocline (depths where

Ω=0.8; Ridgwell and Zeebe (2005)) for the Late Paleocene oceans (e.g., Panchuk et al. 2008; Zeebe et al. 2009; Cui et al. 2011) as it has been made for several EMIC and box model studies might underestimate these dissolution processes.

2.4.4 Sediment composition

The sediment compartment was initialized with 100 % clay. Hence, the resulting distribution of organic matter, opal and $CaCO_3$ in the sediment reflects water column processes. Large sedimentary opal deposits are located in the equatorial Pacific, along the eastern boundary currents and in the Southern Ocean (Figure 2.12). This mirrors the nutrient rich upwelling areas, zones where high production at the surface takes place. However, it is noticeable that the annual net sedimentation rate of opal is very small on the global scale. Since the opal remineralization rate is positively correlated with temperature, we attribute this effect to the increased deep sea temperature as compared to the pre-industrial setup of the model.
$CaCO_3$ deposits cover wider areas, corresponding to supersaturated ($\Omega > 1$) bottom waters and $CaCO_3$ production at the surface. Present-day apparent predominance of $CaCO_3$ accumulation in the Atlantic and Indian Ocean compared to the Pacific is also preserved in the Late Paleocene simulations. A greater degree of undersaturation in the deep Pacific exists as a consequence of metabolic CO_2 accumulation (Ridgwell and Zeebe 2005). Unlike today, the Arctic and Southern Ocean bear $CaCO_3$ deposits, attributed to a regionally higher $CaCO_3$: POC rain ratio and less corrosive bottom waters in these regions.

The upper 14 cm of the sediment being affected by dissolution processes contain a total $CaCO_3$ amount of 2049 Gt C. This corresponds to a global average $CaCO_3$ wt% of 36. The absolute amount of sedimentary $CaCO_3$ in our simulation is slightly higher than estimates for present-day (1610 Gt C, CMIP5 simulation with MPI-ESM; 1770 Gt C, Archer et al. 1998). Another model study results in a lower total $CaCO_3$ amount of 800 Gt C for present-day and a decrease to 620 Gt C for a pre-PETM setup (Zeebe (2012a)).
Panchuk et al. (2008) evaluate their computed $CaCO_3$ distribution by a compilation of late Paleocene marine sediment cores. We use the same dataset to evaluate our results. Our model captures the spatial pattern and the absolute values of the compiled sediment core data relatively well (Figure 2.12), yet our model calculates a much smaller $CaCO_3$: POC rain ratio. Differences between Panchuk et al. (2008) and our estimates persist in the absence of $CaCO_3$ in the Central Pacific, as well as in the abundance of $CaCO_3$ in the North Atlantic in our results. This could be due to the different locations for northern hemisphere deepwater formation, which is located in the North Pacific in Panchuk et al. (2008), but in the North Atlantic in our simulation. Our model results match the South Atlantic data quite well. The same is true for Western

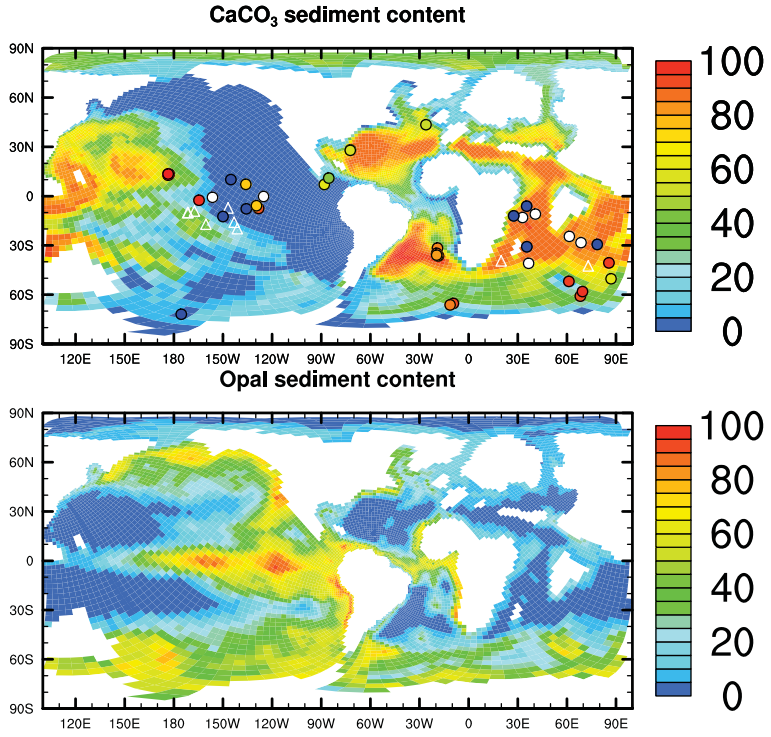

Figure 2.12: Sediment content of $CaCO_3$ and opal (both in wt%), averaged over the last 30 years of the simulation. The $CaCO_3$ plot includes observational data points from Panchuk et al. (2008): colored dots indicate wt%, white dots indicate that $CaCO_3$ is present but wt% is unknown, triangles indicate a hiatus (due to non-deposition).

and Central Pacific sediments and parts of the Indian Ocean. The mismatch in the eastern Pacific and Central Indian Ocean is mainly due to depth divergences between the cores and the model bathymetry. For instance, the 0 wt% sediment cores in the Indian Ocean are displaying the $CaCO_3$ content between 4000 and 4900 m depth. The applied bathymetry is several 100 m shallower in these locations. Nevertheless, the model seems to underestimate the $CaCO_3$ abundances in the Atlantic and Indian sector of the Southern Ocean while the Pacific sector shows, consistently with the data, very low $CaCO_3$ wt%.

2.5 Summary & Conclusions

Using the biogeochemistry model HAMOCC coupled with the ocean general circulation model MPIOM we establish a steady-state ocean biogeochemistry simulation with Late Paleocene boundary conditions. We present spatial and vertical tracer distribu-

tions within a warmer climate and display how the Late Paleocene ocean physical state influences the biogeochemistry. We provide a general overview of major oceanic carbon cycle components in a high CO_2 (560 ppm) world and give estimates of the PETM background climate.

The Late Paleocene simulation reveals a strong stratification of water masses, which is displayed by temperature and salinity profiles, as well as the shallow MLD. These conditions are also found in other coupled atmosphere-ocean general circulation models using Eocene boundary conditions (Lunt et al. 2010). The sluggish circulation affects the atmosphere-ocean exchange fluxes of CO_2 by shifting its spatial patterns, i.e. uptake in the Indian and Southern Ocean compensates the CO_2 outgassing of the Atlantic Ocean. Moreover, we infer a reduced vertical transfer of carbon from surface to intermediate and deep waters due to the more stagnant circulation in comparison to pre-industrial conditions. Nevertheless, the enhanced thermal vertical stratification is not prominent enough to prevent the supply of nutrients to surface waters and hence the global primary production is only slightly decreased.

The intensification of primary production along the equator causes enhanced remineralization within the upper 1000 m of the Atlantic and Pacific, leading to strong OMZ's. The global pattern in oxygen distribution in the intermediate and deep waters is affected by the altered continental configuration. In particular the open Central American Seaway and deepwater formation in the South Pacific ensure the adjustment between Atlantic and Pacific oxygen concentrations.

Our results indicate that an equilibrium CO_2 exchange during Late Paleocene can be established without increased concentrations of TA, as assumed by Pearson and Palmer (2000), while the calculated surface ocean pH (lower than today) is in agreement with the results of Tyrrell and Zeebe (2004) and Ridgwell and Schmidt (2010). Low surface TA concentrations are positively influenced by a lower $CaCO_3$: opal export ratio, since less carbonate leaves the surface ocean. This effect is associated with the temperature dependent remineralization of opal, which produces an increased silicate/opal turnover rate. The simulated export ratio lies within the range of estimates for modern conditions (Schneider et al. 2008), but falls below the estimates given by the simulations of Panchuk et al. (2008) and Ridgwell and Schmidt (2010), covering the Paleocene-Eocene period. This difference may be a result of using quite different type of models.

While the Pacific deepwater is widely undersaturated with respect to $CaCO_3$, the Atlantic does not show any $CaCO_3$ undersaturation in depth beneath 1000 m. We claim that the warm temperatures in the deep Atlantic are responsible for producing a too weak saturation gradient (by decreasing saturation concentration) compared to other studies (e.g., Zeebe et al. 2009). The surface ocean is characterized by globally lower CO_3^{2-} concentrations than today, because of higher atmospheric CO_2 concentrations.

In terms of sensitivity of the carbonate chemistry to a large carbon perturbation, as it is estimated for the PETM, Late Paleocene climatic conditions seem to have opposing

effects. The lower surface ocean CO_3^{2-} : DIC ratio indicates a reduced carbonate buffer capacity and results in higher sensitivity towards additional CO_2. Yet, the reduced $CaCO_3$: opal export ratio counteracts this effect at least partially in our simulation, since effectively less carbonate is exported from the surface ocean. In greater depth, the decreased $CaCO_3$ saturation concentration (i.e. increased Ω) would reduce the sedimentary $CaCO_3$ dissolution. Furthermore, the warm and stratified ocean would reduce the amount of CO_2 reacting with seawater and being transported into the deep ocean already beforehand.

Chapter 3

Late Paleocene ocean biogeochemistry under different ocean circulation regimes

3.1 Introduction

As shown in Chapter 2, ocean biogeochemistry is to a large extent a product of climate state and the underlying ocean general circulation regime. Also previous studies using HAMOCC discuss the importance of the physical state of the ocean for the distribution of ocean biogeochemistry tracers (e.g., Maier-Reimer 1993; Ilyina et al. 2013; Heinze et al. 1991).
In the ocean stand-alone configuration, we investigated a steady-state Late Paleocene climate as initial condition for the PETM. However, in order to focus on the actual PETM perturbation of the oceanic biogeochemical cycles, fully coupled simulations with the MPI-ESM have to be performed. In contrast to the ocean-only simulations, based on ECHAM5 forcing (Heinemann et al. 2009), the ESM experiments are based on the ECHAM6 model version. Accordingly, a different climate state and ocean biogeochemical regime is produced.
The main goal of this chapter lies in the comparison of the two climate states (Table 3.1). We analyze the different climates, which emerge from the two setups by using a simple energy balance model. Furthermore, we study how the different ocean physical states influence the ocean biogeochemistry. Since the comparison of the ECHAM5 and ECHAM6 based Late Paleocene climate reveals major changes in the thermohaline ocean circulation, including a shift in main deepwater formation areas from the North Atlantic to the Southern Ocean. The location of the deepwater formation areas is under discussion for the Late Paleocene and the PETM (e.g., Kennett and Stott 1991; Bice and Marotzke 2002; Tripati and Elderfield 2005; Nunes and Norris 2006). Their location is of substantial importance for the vertical distribution of ocean biogeochemical properties. Consequently, the disappearance of North Atlantic deepwater production can have major implications on the ocean biogeochemistry. We evaluate the resulting Late Paleocene ocean biogeochemical conditions in respect to possible implications on the PETM.

Model setups

Version/Parameter	**ECHAM5** based	**ECHAM6** based
atmospheric model	ECHAM 5.3	ECHAM 6.1
spatial resolution	T31L19	T31L31
atmospheric carbon dioxide	560 ppm	560 ppm
orbital parameters	constant	constant
eccentricity	0.03	0.03
obliquity (deg)	23.25	23.25
longitude of perihelion (deg)	270	270
ocean model	MPIOM	MPIOM 1.5.1
spatial resolution	GR30L40	GR30L40
sea surface albedo	0.07 (const.)	0.12 [glob avg.] (dynam.)
land model	-	JSBACH 2.01
vegetation state	glob. homogeneous 40% woody savanna 60% bare soil	steady, computed by dynamical vegetation module
land surface background albedo (soil albedo)	0.16	0.4

Table 3.1: Model setups used for comparison of background climates. Overview of main model parameters.

The chapter is organized as follows. In Section 3.2 we give a description of the coupled (ECHAM6 based) model setup. In Section 3.3 the differences in atmospheric and oceanic physical states between the two model configurations are analyzed, before we deal with the consequences for the ocean biogeochemistry in Section 3.4. In Section 3.5 we discuss the reversed carbonate ion gradient between the Pacific and the Atlantic which results from the coupled setup. Section 3.6 presents a summary and discussion of the results.

3.2 Model description and setup

We use the Max Planck Institute-Earth System Model (version 1.0.00) (MPI-ESM, Fig. 3.1) for the simulations of the PETM. It consists of the AGCM ECHAM6 and the ocean general circulation model (OGCM) MPI-OM, as well as the ocean biogeochemistry model HAMOCC and the land surface model JSBACH. ECHAM6+JSBACH and MPIOM+HAMOCC interact with each other via the oasis3 coupler program (Giorgetta et al. 2013). The carbon cycle is fully represented in our setup. However, the atmospheric CO_2 concentrations are not calculated interactively, instead we use prescribed greenhouse gas concentrations. Fluxes between atmosphere, land and ocean are diagnosed.

The coupled model setup is spun up for additional several 1000 years to reach an equilibrium climate state and to reduce model drift to an acceptable size. The atmosphere and ocean physical climate state for the ECHAM6 based simulation is taken from the Late Paleocene simulation of Heinemann et al. (2009). The biogeochemistry state is based on the ocean-only simulation of Chapter 2. The model reaches an equilibrium in atmospheric conditions and surface ocean properties like temperature and salinity rather fast, but the deep ocean needs several overturning cycles until the drift is decreased to a tolerable extent (see Jungclaus et al. 2013, for description of spin-up requirements).

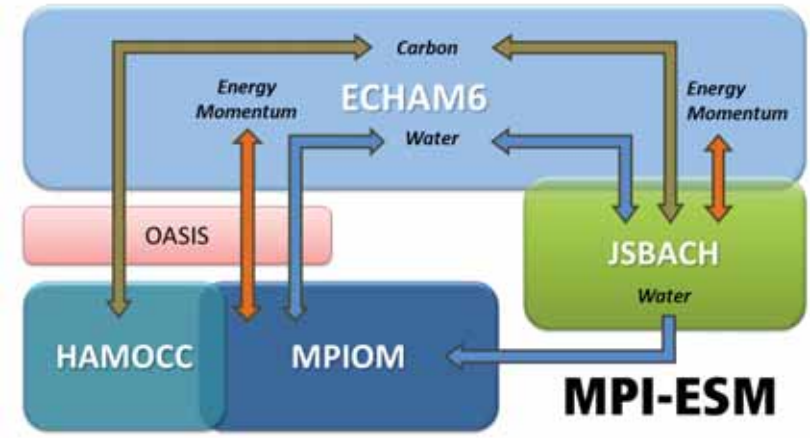

Figure 3.1: Schematic view of MPI-ESM. The colored boxes show the single model components (after Giorgetta et al. 2013).

3.2.1 Atmosphere model ECHAM6

ECHAM6 (here: version 6.1.00) is used for the numerical simulation of the general atmospheric circulation and describing the dynamics of the atmosphere (Stevens et al. 2013). ECHAM6 includes a spectral dynamical core for solving equations for vorticity, divergence, temperature and the logarithm of surface pressure. A flux-form semi-Lagrangian scheme following Lin and Rood (1996) is used for the transport of water components (vapor, cloud liquid water, cloud ice). An implicit coupling scheme, which allows for synchronous calculation of the prognostic variables and surface fluxes is used. Thus, the land surface temperature can be obtained from the surface energy balance equation (Roeckner et al. 2006).
ECHAM6 was developed on the basis of ECHAM5 (Roeckner 2003). Main differences between ECHAM6 and ECHAM5 lie in the radiation schemes. While the rapid radiation transfer model long-wave scheme (Iacono et al. 2008) has already been used in ECHAM5, the short wave scheme (formerly: four-band model of Fouquart and Bonnel (1980)) is now also based on a short-wave rapid radiation transfer scheme for GCM's. Another difference is the revised surface ocean albedo scheme. Over open water the surface albedo is calculated as a function of the zenith angle (Roeckner et al. 2012) in ECHAM6. Also the triggering condition for convection is changed in ECHAM6. It is based on predicted variance of the virtual potential temperature and not anymore on a constant temperature increment. (Giorgetta et al. 2013).
We use ECHAM6 in the T31 spectral truncation, which equals a horizontal grid spacing of approximately 3.8°x 3.8°. The 31 vertical layers resolve the atmosphere up to 10 hPa (note that the ECHAM5 simulation uses only 19 vertical levels, resulting in a poorer representation of the upper atmosphere). Orbital parameters (obliquity, eccentricity and longitude of perihelion) are prescribed rather than calculated from the internal calendar. Due to uncertainties in the calculations of these parameters for periods in Earth history older than 45 Myr (Laskar et al. 2011), we prescribe the values selected by Heinemann et al. (2009), which are close to the temporal average of the solution by (Laskar et al. 2011). Interactions between subgrid-scale orography and atmospheric flow have been included by the implementation of a Lott and Miller (Lott and Miller 1997) style parameterization. The parameterization treats interactions between subgrid-scale orography and atmospheric flow. Unlike the standard version of ECHAM6, we can not account for the subgrid-scale orography parameterization here, as the required information (i.e., standard deviation, anisotropy, maximum/minimum elevation, mean slope, mean orientation, and mean elevation of orographic features within a grid cell (Stevens et al. 2013)) is not available for the Late Paleocene setup. We prescribe an atmospheric CO_2 concentration of 560 ppm for the Late Paleocene background climate. In the absence of available proxy data, the other simulated greenhouse gases (i.e., methane and nitrous oxide) are set to pre-industrial concentrations. The CO_2 concentration is as-

sumed to be constant in the whole model atmosphere. For the simulations including CO_2 increase scenarios (PETM runs, Chapter 4), we add CO_2 linearly over a time period of 1300 years, ending in atmospheric CO_2 concentrations of up to 1480 ppm. For running the model in stable conditions under these high CO_2 concentrations, we use the modifications of Popp et al. (in press), which mainly comprise extensions of look up tables in the ECHAM6 source code. We ran test simulations with up to 800 ppm CO_2 and obtain binary identical model results. This makes us confident that the applied changes do not influence the general behaviour of ECHAM6.

3.2.2 Land surface model JSBACH

The land surface model JSBACH (here: version 2.01) describes physical and biogeochemical aspects of soil and vegetation and is incorporated into the atmosphere model ECHAM6. It is the subsystem model for land and vegetation (Reick et al. 2013; Schneck et al. 2013) within the MPI-ESM. The land surface in JSBACH is subdivided into tiles, to cope with subgrid scale heterogeneity. Theses tiles are covered with 8-12 different plant functional types (PFT). They distinguish from each other by particular properties, which characterize processes simulated in JSBACH (e.g. surface roughness, albedo, etc.) (Reick et al. 2013). Soil hydrology is described by a simple single-layer bucket model. River discharge is treated interactively and part of a hydrology module (Hagemann and Gates 2003). It contains a river scheme which is determined by the geopotential height gradient of the Late Paleocene topography. Freshwater fluxes resulting from it, are passed to the ocean via the precipitation field. JSBACH includes a dynamic vegetation module based on a tiling approach (Brovkin et al. 2009). It enables climate-consistent development of the geographic distribution of vegetation. The distribution is determined dynamically from plant productivity under the prevailing climate conditions.

To achieve a balanced vegetation state, the vegetation is simulated dynamically over a period of 700 years under Late Paleocene conditions (Port et al., in prep.). The resulting steady state vegetation distribution is then prescribed for the conducted simulations discussed in Chapter 3 and Chapter 4. The fractional coverage by each vegetation type within every grid cell is fixed. However, depending on the climatic conditions the net primary production and the leaf area index can vary within the cover fraction.

Due to the lack in proxy data, we selected a soil albedo (bare surface) of 0.4. This value is equivalent to a rather bright surface, leading to rather high albedo on the wide range of possible background albedos.

The CO_2 increase scenarios as they are computed in Chapter 4 are just partly influencing the land carbon inventories in our setup. JSBACH accounts for climate change induced effects due to rising CO_2 in ECHAM6 (e.g., changes in temperature increase/decrease vegetation), but not for the carbon concentration feedback (e.g. in-

creased carbon uptake by plants due to CO_2 fertilization).

3.2.3 Ocean circulation model MPI-OM

The Max Planck Institute-Ocean Model (MPI-OM, here: version 1.5.1) (Marsland et al. 2003; Jungclaus et al. 2006, 2013) is a global general circulation model, which is formulated on an orthogonal curvilinear C-grid in horizontal and z-grid in the vertical (Arakawa and Lamb 1977). The model contains a free surface elevation and fully resolves the discretised bottom topography, since vertical integration includes partial grid cells at the lower boundary. MPI-OM is based on primitive equations which are solved with the hydrostatic and Boussinesq approximations (Marsland et al. 2003). The Pacanowski and Philander (1981) scheme together with an additional wind mixing parameterization is applied for the vertical eddy viscosity and diffusion, since the classical Pacanowski and Philander scheme underestimates the turbulent mixing close to the surface (Jungclaus et al. 2006). The effect of isopycnal tracer mixing induced by unresolved mesoscale eddies is parameterized following Gent et al. (1995). The mixed layer depth (MLD) is calculated using a potential density critereon. It is defined as the depth at which a 0.125 kg m^{-3} change of potential density with respect to the surface occurs (Jungclaus et al. 2013). The MLD depends on wind-induced mixing, Ekman subduction, and mixing of gravitationally unstable water columns.
MPI-OM includes a sea-ice model which accounts for sea ice dynamics, following Hibler (1979) and sea ice thermodynamics following Semtner (1976). Changes in sea-ice thickness are calculated based on sea ice thermodynamics, which result from the balance of radiant and turbulent atmospheric fluxes and oceanic heat fluxes (Jungclaus et al. 2006).
The Late Paleocene setup includes MPI-OM with a quasi-homogeneous horizontal grid-spacing of 3.5° and 40 unequally spaced vertical levels. The time step is 2.4 hours. The model setup is based on the interpolation of a Late Paleocene 2°x2° topography, reconstructed by Bice and Marotzke (2001). The curvilinear grid allows an arbitrary placement of the grid poles. One pole is set over Siberia and the other one over South America. These locations are used to receive a relatively high grid resolution over the key ocean regions (e.g. deepwater formation areas). The combination of horizontal grid resolution and location of the poles translates into a grid spacing from 70 km around South America, to 430 km in the Pacific.

3.2.4 Ocean biogeochemistry model HAMOCC

For the simulation of the ocean biogeochemistry we use the Hamburg Carbon Cycle Model (HAMOCC, here: version 5.1), which is described in details in Section Section 2.2. The used version of HAMOCC includes a biogeochemical feedback on shortwave radiation penetration depth (Wetzel et al. 2006). The attenuation depth for

shortwave radiation is calculated as a function of phytoplankton concentrations simulated with HAMOCC (Wetzel et al. 2006). Besides the biogeochemical feedback on shortwave radiation penetration depth, the applied version of HAMOCC is the same as described in Section 2.2, the only difference consists in the coupled model environment. HAMOCC can interact with the atmosphere, as long as the respective tracers are provided by the atmospheric model. However, CO_2 exchange processes remain unchanged compared to the stand-alone setup, since we run our simulations with prescribed atmospheric CO_2 concentrations, which are homogeneously distributed throughout the atmosphere. HAMOCC in the coupled MPI-ESM setup accounts for climate change feedbacks on the ocean biogeochemistry. Ocean biogeochemical tracer distributions are influenced by freshwater fluxes (i.e., precipitation, evaporation, river runoff) and wind speed at 10m height (for air-sea exchange), which is calculated in ECHAM. MPIOM provides temperature and salinity for calculations in HAMOCC. The ocean and atmosphere components in MPI-ESM are coupled daily without flux corrections (Giorgetta et al. 2013).

In the frame of this study, new processes were introduced into the model:

1. $CaCO_3$ production dependent on the calcite saturation state
   We implemented a calcite saturation state (Ω) dependent calcium carbonate ($CaCO_3$) production (following Ilyina et al. 2009). In the standard HAMOCC configuration, diatom growth is favored as long as silicate is available. Production of $CaCO_3$ takes over after silicate is depleted. In a warm stratified ocean, this model assumption may lead to a shift in shell production: As the surface ocean becomes depleted in nutrients including silicate, production of $CaCO_3$ is favored (see for instance, Six et al. 2013). Yet, a high CO_2-world is more likely to experience a decrease in $CaCO_3$ production (e.g., Riebesell et al. 2000). Therefore, the saturation state dependent $CaCO_3$ production is used for all PETM simulations.

   The standard equation for opal and CaCO3 production as used in HAMOCC 5.1 reads as follows:

$$delsil = min\left(R_{Si:P}\frac{\Delta DET}{\Delta t}\ \frac{SI(OH)_4}{K_{PHY}^{SI(OH)_4} + SI(OH)_4}, 0.5\ SI(OH)_4\right) \tag{3.1}$$

   where $R_{Si:P}$ denotes the Si:P ratio required by silicifiers, $K_{PHY}^{SI(OH)_4}$denotes the half saturation constant for silicate uptake and $SI(OH)_4$ the available silicate for each grid cell.

$$delcar = R_{Ca:P}\frac{\Delta DET}{\Delta t}\ \frac{K_{PHY}^{SI(OH)_4}}{K_{PHY}^{SI(OH)_4} + SI(OH)_4} \tag{3.2}$$

where $R_{Ca:P}$ denotes the Ca:P ratio required by calcifiers.

Exported detritus (DET) is first assigned to forming of opal shells. Not more than 50 % of the available silicate can be used for opal shell formation. The rest of the detritus is assigned to $CaCO_3$ shell formation.

The equation for opal production remains unchanged. However, we change the $CaCO_3$ production in a way that it is depending on Ω, which is defined as:

$$\Omega = \frac{[Ca^{2+}] \times [CO_3^{2-}]}{K_{sp}^*} \tag{3.3}$$

where $[Ca^{2+}]$ is the calcium ion concentration (constant at 10.3 mmol kg^{-1} in the model), $[CO_3^{2-}]$ denotes the carbonate ion concentration of seawater and K_{sp}^* is the stoichiometric solubility product of $CaCO_3$ for in situ pressure.

$$\mathbf{prod_\Omega} = max\left(\Omega \times \frac{1}{\Omega_{ref} - 1} - \frac{1}{\Omega_{ref} - 1}, 0\right), \tag{3.4}$$

$$for\ \mathbf{prod_\Omega} > 1,\ otherwise\ \mathbf{prod_\Omega} = 1.$$

where Ω_{ref} describes a (3d-grid point specific) reference value for Ω, chosen at an arbitrary time step at constant atmospheric CO_2 concentrations. Eq. 3.2 is modified as:

$$delcar_\Omega = delcar \times \mathbf{prod_\Omega} \tag{3.5}$$

In a steady state climate (constant CO_2) the calcification rate is not affected by the applied changes. Just by increasing CO_2 and thus decrease in surface ocean Ω the calcification rate is reduced linearly. Consequently the ocean biogeochemical background state discussed in this chapter is comparable to the one of Chapter 2 since the production term is identical. However, for the experiments using a CO_2 emission scenario in Chapter 4 the calcification rate is affected by the additional factor in the production term.

2. Deep ocean carbon source
   Some studies (Dickens et al. 1995; Dickens 1999; Svensen et al. 2004; Zeebe et al. 2009) suggest that the PETM carbon perturbation was driven not only by the

atmospheric CO_2, but also by a deep ocean source (primarily located in the Atlantic) of carbon/CH_4 (this scenario is discussed in details in Chapter 4). Since released CH_4 would quickly oxidize to CO_2 we do not account for this intermediate step and only prescribe a carbon source. In a first order approximation, the addition of CO_2 to the deep ocean is simulated by simply increasing the DIC concentration (while keeping carbonate ions constant) according to the desired amount in Gt C a^{-1} in the oceanic bottom layer. We calculate the volume of the oceanic bottom layer for a specific ocean basin (here: Atlantic) and for a specific ocean depth (here: >1000 m). The simulated carbon input (atCin) is added yearly to the DIC concentration in the oceanic bottom layer of the Atlantic. Oxygen reduction due to dissociation of CH_4 to CO_2 is not considered in our approach.

$$for\ kbo > 1000m,$$

$$atlvol = dlxp(i,j) \times dlyp(i,j) \times ddpo(i,j,kbo(i,j)) \tag{3.6}$$

where kbo is the index field of the oceanic bottom layer in the model, dlxp relates to the longitudinal dimension, dlyp to the latitudinal dimension, and ddpo denotes the vertical extent of a grid cell in the model.

$$atCin = \left(\frac{C_{inp} \times R_{GtC:mol}}{dty \times atlvol} \right) \tag{3.7}$$

where C_{inp} denotes the respective carbon input in Gt C a^{-1}, $R_{Gt\ C:mol}$ denotes the ratio for conversion of Gt C in mol, dty denotes timesteps per year.

3.3 Climate states and ocean circulation regimes

3.3.1 Atmosphere physical state

The comparison of the atmospheric physical state between the ECHAM5 and ECHAM6 based simulations shows several differences, both in absolute numbers and in spatial distribution of atmospheric properties. Distinctly different atmospherical states between the two model versions are mainly caused by: (1) the different handling of shortwave radiation (i.e., application of new radiation scheme), (2) the parameterization of the surface albedo over open water, (3) the treatment of the land surface and vegetation and (4) representation of the upper atmosphere (19 vs. 31 vertical levels in ECHAM5 and ECHAM6, respectively).

Energy balance model

To study why the models behave differentially we are comparing globally averaged results by using a set of basic equations, which is compiled to a zero-dimensional energy balance model (EBM) following Heinemann et al. (2009).
The surface temperatures given by the general circulation models (GCM) differ by about 2 ℃ in global average (Table 3.2). Although the surface albedo is much higher in the ECHAM6 simulation, it yields a lower planetary albedo. The rather huge difference in surface albedo can be explained by the ocean albedo parameterization which results in a globally averaged albedo of 0.12 versus 0.07 (ECHAM5) over the ocean. Moreover, the dynamically calculated vegetation in combination with a higher value for the land surface background albedo (0.4 versus 0.16) produces a higher albedo over land than in the homogeneous vegetation distribution in the ECHAM5 configuration. Nevertheless, since the planetary albedo is smaller by 0.013, less shortwave radiation is reflected by the atmosphere. This effect alone should produce a warmer climate state in the ECHAM6 simulation. However, the longwave emissivity, which is much higher in the ECHAM6 simulation (by 0.22 in global average), causes a cooling of the atmosphere. Since more longwave radiation is leaving at the top of the atmosphere, the greenhouse effect is effectively smaller.
By calculating the planetary albedo and the emissivity for clear-sky conditions, the impact of clouds on the atmospheric state can be isolated. The planetary albedo change due to clouds amounts to 0.136 which is less than in ECHAM5 runs (0.158). The same applies to the influence of clouds on the longwave radiation, in the ECHAM6 runs clouds reduce the longwave emissivity less. The cloud radiative forcing for shortwave radiation (Equation 3.8) is consequently weaker in the ECHAM6 runs.

$$CRF_{SW} = (\alpha_{cs} - \alpha_{fs}) \times \frac{S_0}{4} \tag{3.8}$$

where α_{cs} denotes planetary albedo for clear sky conditions and α_{fs} for full sky conditions, S_0 denotes the total solar irradiance.

The cloud radiative forcing for longwave radiation (Equation 3.9) is weaker, too. Additionally to the smaller cloud effect, the upward longwave radiation at the surface is also reduced (as a result of lower surface temperatures) towards the ECHAM5 version.

$$CRF_{LW} = (\epsilon_{cs} - \epsilon_{fs}) \times LW_s^{\uparrow} \tag{3.9}$$

where ϵ_{cs} denotes longwave emissivity for clear sky conditions and ϵ_{fs} for full sky conditions, $LW_s^{\uparrow}$ denotes the upward longwave radiation at the surface.

The cloud related effects are smaller, although the total cloud cover is increased in the ECHAM5 runs (Table 3.2). However, the lower surface albedo in the ECHAM5 setup enhances the cloud effect. Since the calculation of the cloud radiative forcing includes clear sky conditions, the strength of the effect is also depending on the darkness of Earth's surface.
The vertically integrated water vapour is 20 % lower in the ECHAM6 setup. The reduced atmospheric water vapour content causes a decreased greenhouse effect, which should result in cooling compared to the ECHAM5 simulation. Heinemann et al. (2009) discussed that the water vapour feedback in the ECHAM5 - Late Paleocene setup may be larger than in other simulations representing this time period (e.g. NCAR model).

Quantification of single effects

We use the EBM to quantify the major mechanisms that cause the surface temperature differences between the two model versions. The EBM equates the incoming shortwave radiation and outgoing longwave radiation to obtain the global surface temperature:

$$\frac{S_0}{4}(1 - \alpha) = \epsilon\sigma\tau_{s,ebm}^4 \tag{3.10}$$

where S_0 is the incoming solar radiation at the top of the atmosphere, the factor $\frac{1}{4}$ accounts for Earth as a sphere, α is the planetary albedo, ϵ the atmospheric emissivity, σ is the Stefan-Boltzmann constant, τ is the surface temperature.

Based on the EBM we calculate a surface temperature of 296.5 K for the ECHAM6 simulation, which is close to the one given by the GCM (295.2 K). The EBM determined temperature difference between the two models compares relatively well to the results of the GCM. The globally averaged temperature difference between the two model versions amounts to 1.6 K based on the EBM and 1.8 K based on the GCM. According to the EBM the reduced planetary albedo should lead to a warming of 1.4 K in

Key climate parameters and Energy balance Model		
Parameter	**ECHAM5** based	**ECHAM6** based
surface temperature τ_s	297.0 K	295.2 K
surface temperature $\tau_{s,ebm}$	298.1 K	296.5 K
planetary albedo α	0.291	0.278
surface albedo α_s	0.094	0.162
effective emissivity ϵ	0.541	0.563
clear sky effective emissivity ϵ_c	0.607	0.622
clear sky planetary albedo α_c	0.133	0.142
total cloud cover (fraction)	0.575	0.584
vertically integrated water vapour	45.71 kg m^{-2}	36.71 kg m^{-2}
upward longwave radiation at the surface ($LW_s^{\uparrow}$)	-445.8 W m^{-2}	-434.0 W m^{-2}
Shortwave cloud radiative forcing (CRF_{SW})	-54.3 W m^{-2}	-46.5 W m^{-2}
Longwave cloud radiative forcing (CRF_{LW})	29.4 W m^{-2}	25.6 W m^{-2}

Table 3.2: Results of the energy balance model for the comparison of background climates in the two model configurations.

respect to the ECHAM5 simulation. The increased longwave emissivity is responsible for a cooling of 3 K. The emissivity induced cooling can be further separated into its underlying mechanisms. Since both simulations prescribe the same CO_2 concentration, the weaker longwave cloud radiative forcing (25.6 W m^{-2} compared to 29.4 W m^{-2}) explains 1.3 K of the cooling. The smaller amount of atmospheric water vapour (36.71 kg m^{-2} compared to 45.71 kg m^{-2}) is responsible for 1.7 K of the cooling.

Regional temperature differences

The zonal mean surface temperature difference is larger in the Northern Hemisphere than in the Southern Hemisphere (Figure 3.2). In the austral outer tropics, the zonal mean temperature is not deviating from each other. However, the horizontal 2 m temperature plot (Figure 3.3), shows that local temperature differences are mainly over the ocean, which can be attributed to oceanic heat uptake due do different overturning circulation (see Section 3.3.2). The average pole-to-equator temperature gradient is not affected by the different model versions.

Planetary albedo divergence is strongest in the Southern Hemisphere high latitudes. The reduced planetary albedo in the ECHAM6 version is linked to a lower surface albedo and weaker shortwave cloud radiative forcing than in the ECHAM5 simulation. The zonal mean longwave emissivity shows the same latitudinal variation in both simulations, but the ECHAM6 version emits constantly more longwave radiation, except

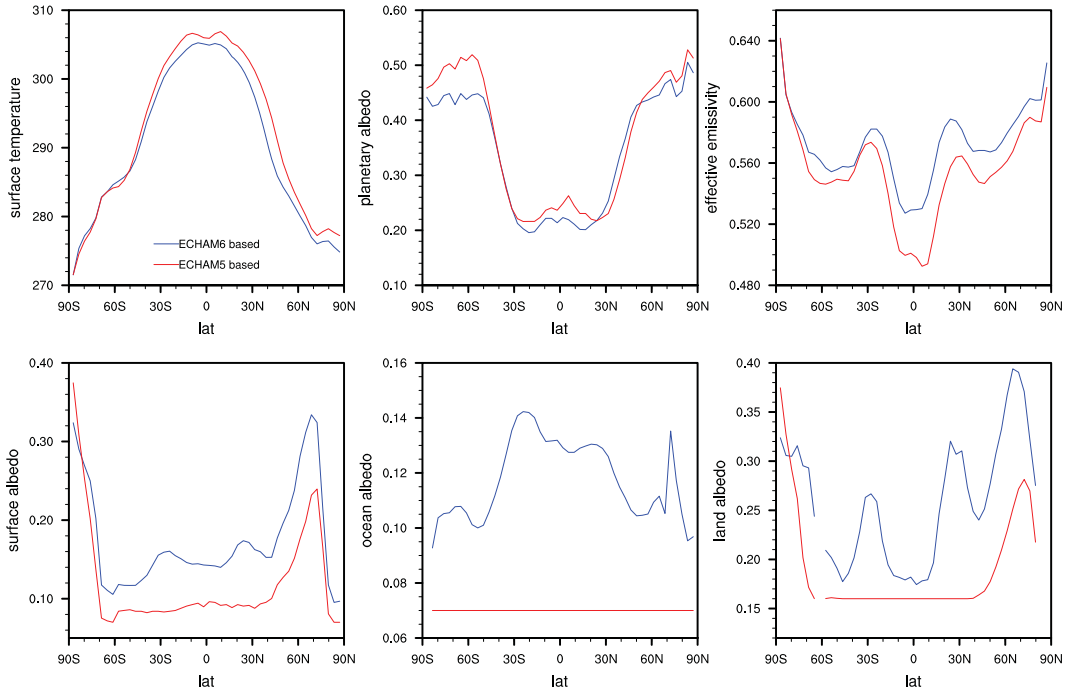

Figure 3.2: Globally integrated zonal mean of EBM properties for the ECHAM6 and ECHAM5 based simulations.

in southern high latitudes.

The zonal mean surface albedo is everywhere higher in the ECHAM6 version, except in the Southern Hemisphere high latitudes. To disentangle the single effects we need to look at ocean and land albedo separately. The ocean albedo is the main contributor to the surface albedo increase in ECHAM6. Through the new ocean albedo parameterization (incl. a zenith angle dependence) the globally averaged surface albedo over the ocean increases from 0.07 (ECHAM5) to 0.12 (ECHAM6). Both simulations are lacking multi-year sea-ice, glaciers and long-term snow accumulation. However, during each hemispheres winter, parts of the high latitudes are covered with snow. In the Arctic Ocean sea-ice emerges over the winter, too; causing a peak in zonal mean ocean albedo at 75 °N (Figure 3.2). The difference in albedo over land is determined by applying distinct approaches. While in the ECHAM5 simulation it is a result of prescribing a homogeneous vegetation, the surface albedo is much more heterogeneous in the dynamically calculated ECHAM6 simulation. The ECHAM5 based model version is computed without JSBACH activated. A globally homogeneous vegetation is prescribed (incl. fraction of bare soil to vegetation, roughness and evaporation), with characteristics similar to modern woody savanna. The surface albedo increases in high

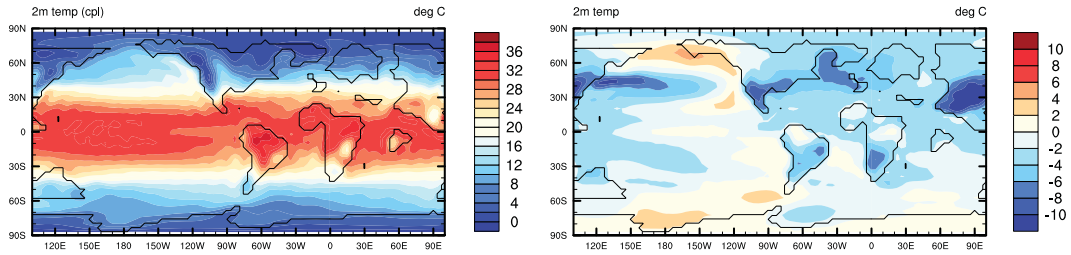

Figure 3.3: Late Paleocene temperature in 2 m height (in ℃) for the ECHAM6 based simulation (left) and the difference between the ECHAM6-ECHAM5 based simulation (right).

latitudes due to the snow cover in the winter months. In global average, this vegetation results in a lower albedo compared to the ECHAM6 simulation. The vegetation state which is used in the ECHAM6 simulations consists to a great extent of grasses (Figure 3.4), especially in mid and high latitudes, due to relatively cooler temperatures and disturbances, such as windthrow. The dominant vegetation type in low latitudes is trees, causing a low surface albedo. The dry and vegetation-poor subtropics, especially the extensive dessert in central Eurasia, are responsible for relatively high zonal mean surface albedos. The deserts have also major implications on the atmospheric temperature. The strongest deviations in 2 m temperature over land between the ECHAM6 and ECHAM5 simulations occur over the dessert regions (Figure 3.3). Due to the in average cooler surface temperature, the snow cover in Northern Hemisphere winter is larger then in the ECHAM5 version, causing a zonal mean surface albedo of up to 0.4 at 60-70 °N.

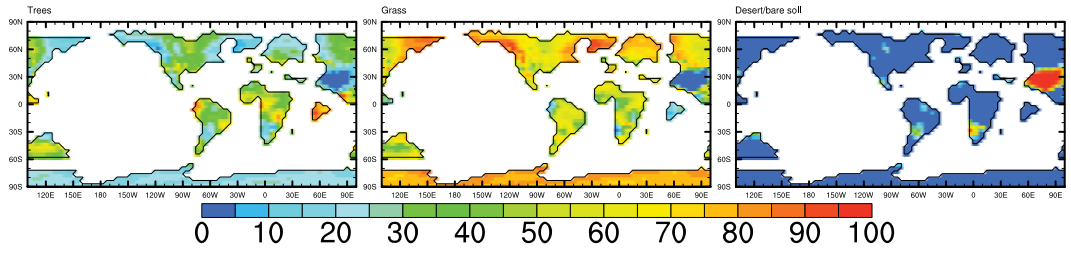

Figure 3.4: Late Paleocene vegetation type fractions (in %) as modeled in the ECHAM6 simulation, based on the (JSBACH) dynamical vegetation module.

3.3.2 Ocean physical state

The SST is on average 1.2 ℃ cooler than in the ECHAM5-based simulation (Table 3.4). Highest SSTs of 34-36 ℃ occur in low latitude areas in the Pacific and Indian Ocean (Figure 3.5) in both setups. In zonal average the simulated SSTs are quite similar between the two model configurations (for the global ocean). Yet, the ECHAM6-based simulation yields generally cooler temperatures due to the absolute decrease in radiative forcing (equivalent to a cooling of globally 1.6 ℃). For the Arctic Ocean, the simulated SSTs differ even more to the TEX_{86} biomarker based reconstructions of Sluijs et al. (2006), which suggest SSTs of ∼17 ℃. Especially the Northern Hemisphere shows lower SSTs compared to the ECHAM5-based simulation (Figure 3.7). In the Atlantic and Pacific these temperature differences are associated with heat transfer to the surface ocean due to convectional processes. These processes are stronger in the ECHAM5 simulation for the Atlantic and in the ECHAM6 simulation for the Pacific.

The sea surface salinity is capturing this signal as well. While in global ocean zonal mean the surface salinity looks similar, it is the North Atlantic region in which the simulations differ mostly. The Arctic Ocean is less saline in the ECHAM6 simulation, caused by a higher freshwater input and less exchange with the surrounding oceans. Figure 3.6 shows the temperature and salinity difference between the two simulations for the Atlantic and the Pacific. The deep Atlantic is less saline and colder (∼4 ℃) in the ECHAM6 simulation, which can be attributed to the different deepwater formation areas. In the ECHAM5 simulation the main sinking area for water masses lies in mid latitudes (40-60 °N), so that the sinking occurs mainly in high latitudes, where the water is colder. The temperature profile of the Pacific exhibits large temperature differences between 35 and 55 °N. The ocean in the ECHAM6 simulation is up to 5 ℃ colder in these latitudes because the absorbed heat from the atmosphere in the tropics

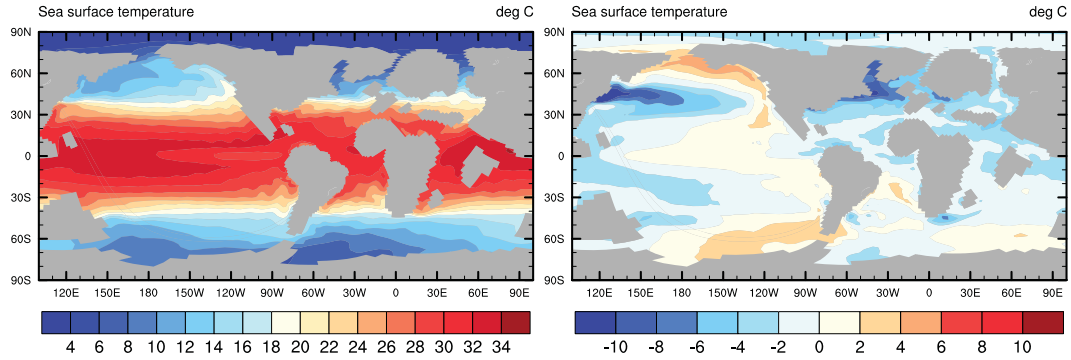

Figure 3.5: Late Paleocene SST (in ℃) for the ECHAM6 based simulation (left) and the difference between the ECHAM6-ECHAM5 based simulation (right).

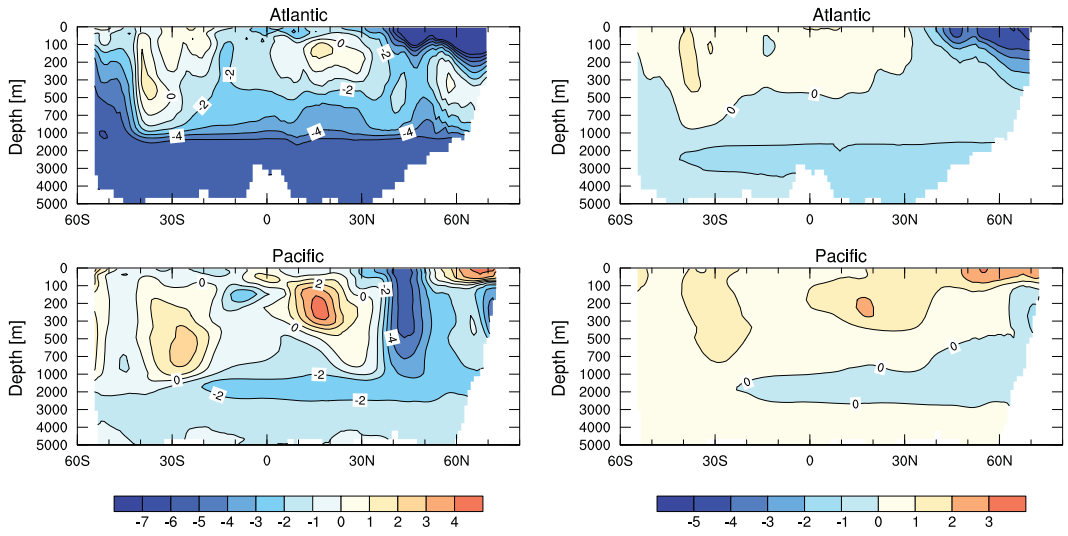

Figure 3.6: Difference in zonally averaged potential temperature (in ℃, left panel) and salinity (right panel) for the Atlantic (top row) and Pacific (bottom row) between the ECHAM6 and ECHAM5 based simulation. Note the non-linear vertical axes, used to zoom in the upper ocean layers.

is not transported as far north and not as deep as in the ECHAM5 simulation. The absolute difference in globally averaged ocean temperature at 4000 m depth is 2.1 ℃.

The North Atlantic surface water exhibits very low salinity in the ECHAM6 simulation which can be attributed to an inflow of low saline waters from the Arctic Ocean. The same is true for the North Pacific in the ECHAM5 simulation. The differences in Northern Hemisphere upper ocean salinity (Figure 3.6) result mainly from this inflow. Additionally, the sinking of denser waters due to thermohaline processes induce the formation of saltier water masses at depth.

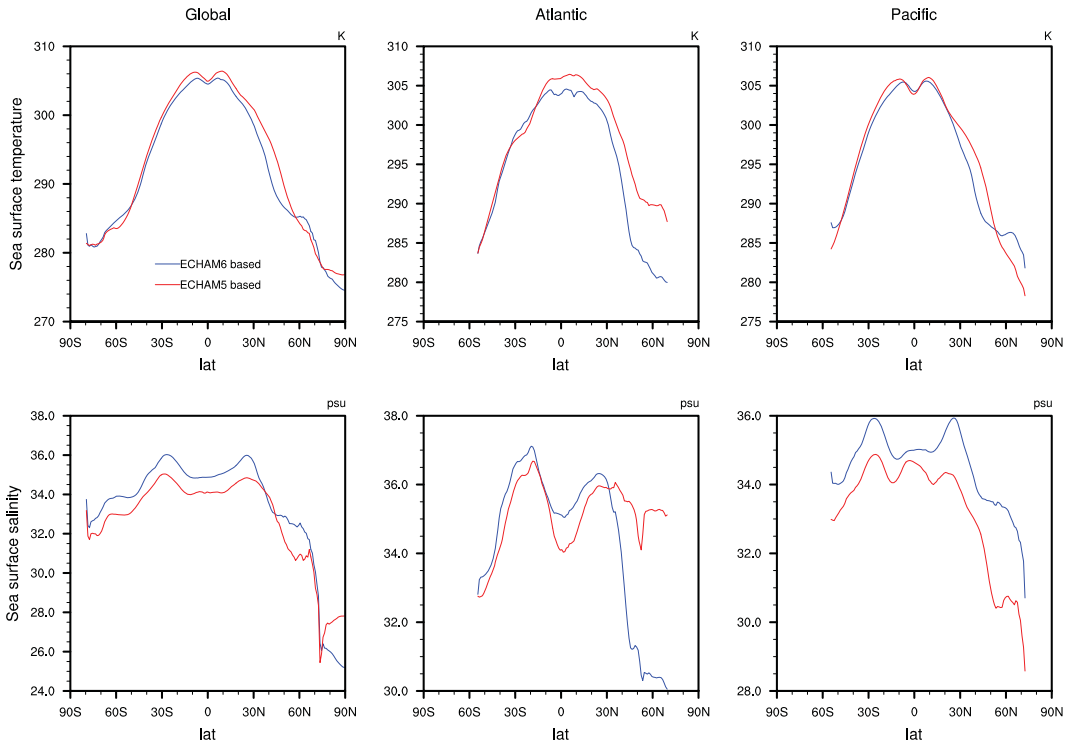

Figure 3.7: Zonally averaged sea surface temperature (in K, top row) and sea surface salinity (bottom row), for the global ocean (left column), the Atlantic (middle column) and the Pacific (right column). Note the different y-axis scales between each plot.

Freshwater budget in the Atlantic Ocean basin

The Atlantic is of special interest, due to its meridional overturning circulation (MOC) and its role for the global climate system. The freshwater forcing is one of the major drivers to changes in the meridional overturning and hence the deepwater formation. We diagnose the freshwater budget of the Atlantic by integrating the relevant properties over the whole Atlantic and a transect (40-70 °N) which covers the North Atlantic deepwater formation area more precisely, over a period of 100 years (Figure 3.8). A positive sign means that the respective term carries a net freshwater flux into the Atlantic basin (North Atlantic basin). The amount of freshwater entering the Atlantic (precipitation - evaporation + runoff) in the area where deepwater formation occurs differs in the two setups. Averaged over the North Atlantic, both simulations show positive fluxes, however the ECHAM6 simulation yields a 6 times higher freshwater input than the ECHAM5 simulation. More intense atmospheric freshwater forcing increases the stratification of water masses in the North Atlantic and results in a significantly

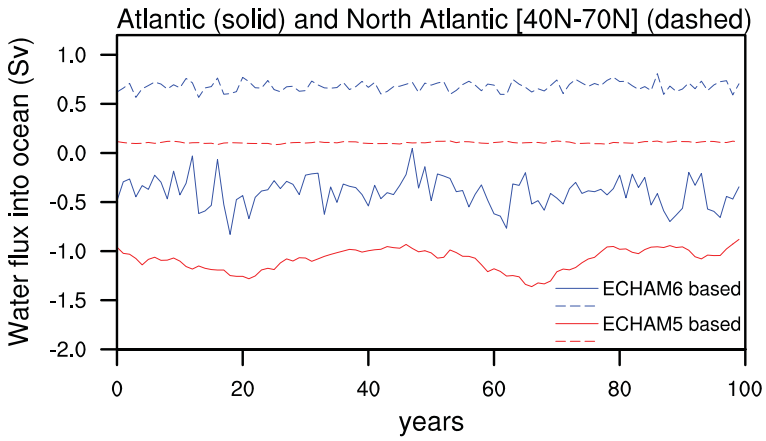

Figure 3.8: ECHAM6 and ECHAM5 based net freshwater flux (precipitation - evaporation + runoff) into the ocean (in Sv), averaged over the whole Atlantic (solid lines) and the North Atlantic (40-70 °N, dashed lines) over 100 simulation years.

weakened deep convection. The ECHAM6 simulation shows both, increased precipitation and decreased evaporation over that area.

Figure 3.9 shows the discrepancy of freshwater forcing in the Pacific and Atlantic between the two simulations. In the tropics the zonal averaged freshwater input behaves inversely to the freshwater input in Northern Hemisphere mid latitudes (over the deepwater formation areas). While the ECHAM6 simulation shows stronger tropical freshwater input over the Pacific, the ECHAM5 simulation exhibits stronger tropical freshwater input over the Atlantic. However, the global zonally averaged freshwater flux exhibits roughly the same pattern in the two simulations. This pattern is characterized by freshwater input in the tropics and mid to high latitudes, and freshwater loss in the subtropics. The peak around 75 °N (Figure 3.9) refers to river runoff in the Arctic Ocean.

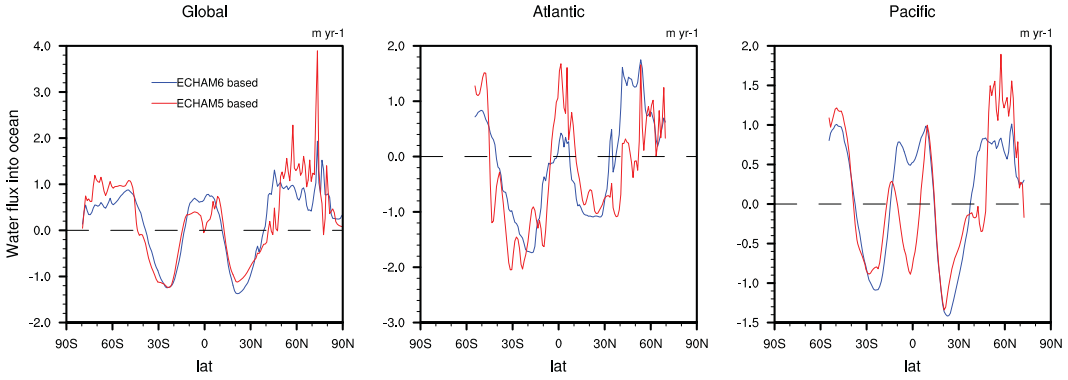

Figure 3.9: Zonally averaged net freshwater flux (precipitation - evaporation + runoff) into the ocean (in m yr^{-1}), for the global ocean (left), the Atlantic (middle) and the Pacific (right). Positive values correspond to an uptake of freshwater, negative values to a loss of freshwater by the ocean. Please note the different y-axis scales between each plot.

Ocean circulation

The circulation differs quite substantially from each other in the two setups, which mainly results from the different atmospheric states discussed in Section 3.3.1. Overall, these primarily regional effects have severe consequences for the overturning circulation of the ocean.

The Late Paleocene setup includes an additional ocean in comparison to the present-day setup: the Tethys Ocean. It is connected to the Arctic Ocean via the Turgai Strait. In both Late Paleocene simulations, the Arctic Ocean exports low salinity water via Turgai Strait into the Tethys (Table 3.3). While the net flux through Bering Strait into the Arctic Ocean is positive in the ECHAM6 simulation, it is negative in the ECHAM5 simulation, which equals an export from the Arctic Ocean into the Pacific. As a result the North Pacific surface salinity is up to 5 PSU lower than in the ECHAM6 simulation (see above).

For the Central American Seaway, the transport of water masses is reversed in the two model configurations. While the westward Atlantic equatorial current ends up in the Pacific in the ECHAM6 simulation, the net volume transport through the Central American Seaway is eastward in the ECHAM5 simulation. From the gross transport rates in the ECHAM6 simulation (Table 3.3), we can derive that the exchange between the Atlantic and Pacific is generally enhanced in this simulation. In the Southern Hemisphere the shallow depth of the Drake Passage and the Australian-Antarctic seaway (both 300-400 m sill-depth) prevent the establishment of the Antarctic Circumpolar

Ocean Currents		
Current/Location (in Sv)	**ECHAM5** based	**ECHAM6** based
Central American Seaway (net)	+5.3	-4.9
CAS (eastward)	+12.7	+19.6
CAS (westward)	-7.4	-24.5
Bering Strait (net)	-2.7	+0.6
Bering (northward)	+0.4	+1.7
Bering (southward)	-3.1	-1.1
Turgai Strait (net)	-2.3	-0.33
Drake Passage (net)	-7.5	-15.4
Max. Atlantic overturning (>1000m depth)	16.9	2.4
Max. Indo-Pacific overturning (>1000m depth)	16.7	17.2

Table 3.3: Major ocean connections and their throughflow (vertically and horizontally integrated), averaged over 100 years for the ECHAM5 and ECHAM6 based simulation. Positive values correspond to eastward or northward flows, negative values to westward or southward flows.

Current. Nevertheless, twice as much water is transported westwards through the Drake Passage in the ECHAM6 simulation, compared to the ECHAM5 simulation. Moreover, the flow direction in the ECHAM6-based simulation is reversed to the eastward circumpolar current we know from modern conditions.

3.3.3 Meridional overturning circulation

In accordance to the distinctly different climate states, the two simulations produce different overturning circulation states as well, which are illustrated in Figure 3.10. The meridional overturning circulation (MOC) of the ECHAM6 based simulation is driven by Southern Hemisphere deepwater formation (max. ∼17 Sv). Sinking of water masses, which is induced by convectional processes, occurs south of the Pacific and south of the Indian Ocean, within the Southern Ocean. In the Northern Hemisphere some overturning occurs in the North Pacific, which produces a locally increased MLD (Figure 3.12). However, it is not comparable to the strength of the North Atlantic overturning in the ECHAM5 simulation. The maximum Atlantic overturning in the ECHAM5 based simulation amounts to 16.9 Sv, while it is only 2.4 Sv in the ECHAM6 simulation (Table 3.3). The increased freshwater input into the North Atlantic in the ECHAM6 simulation acts as a major dampener of deepwater formation in that area. Besides the

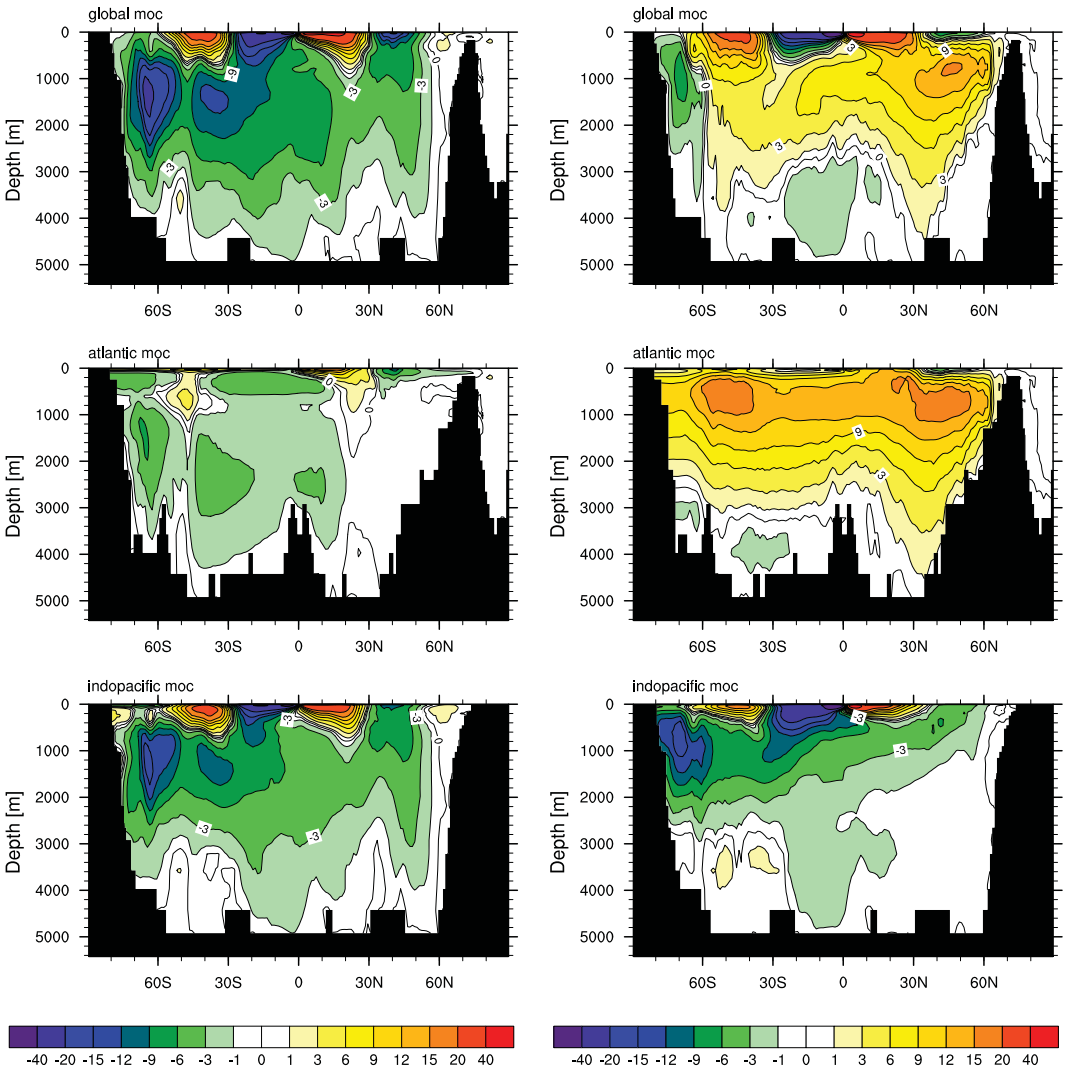

Figure 3.10: Zonally averaged crosscut of the MOC for global ocean (top row), Atlantic (middle row) and Pacific (bottom row), in the ECHAM6 based (left column) and ECHAM5 based (right column) simulation.

decreased evaporation and increased precipitation over the Atlantic in the ECHAM6 simulation, the outflow of subtropical waters from the Atlantic into the Pacific via the Central American Seaway could cause further reduction in salinity. This effective net freshwater flux into the Atlantic, due to free exchange of low-salinity surface water between the North Pacific and North Atlantic and the reduction of the AMOC is also discussed in Mikolajewicz et al. (1993) and Mikolajewicz and Crowley (1997). In the

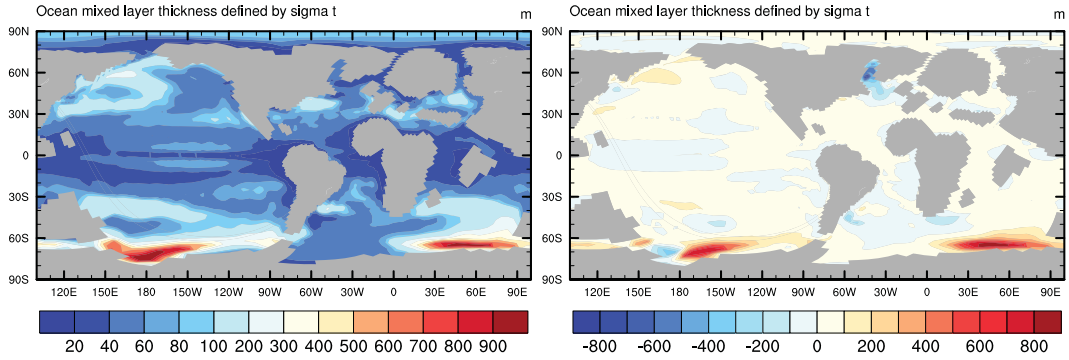

Figure 3.11: Late Paleocene MLD (in m depth) for the ECHAM6 based simulation (left) and the difference between the ECHAM6-ECHAM5 based simulation (right).

Late Paleocene simulation of Winguth et al. (2010) a comparable circulation state is established, lacking deepwater formation in the Northern Hemisphere.

In the ECHAM5 simulation (detailed description in Section 2.3) deepwater formation also occurs south of the Pacific, but it is lacking convectional processes south of the Indian Ocean. Neither does it show overturning in the North Pacific. This could be related to the Arctic Ocean water inflow and the consequently lower salinity concentrations in the surface ocean. Apart from this, the nearly identical equator to pole temperature gradient at the surface should not cause any differences in the MOC between the simulations.

The MOC state in the coupled ECHAM5 simulation of Heinemann (2009) yields switches in Northern and Southern Hemisphere deepwater formation. Since we are using an atmospheric forcing which consists of only 30 years of his model output, we do not reproduce this episodic flushes in our ECHAM5 based simulation. Furthermore, this large temporal variability does not occur in the fully coupled ECHAM6 simulation.

The MOC in the ECHAM5 based simulation is generally more similar to the MOC in modern conditions (Jungclaus et al. 2013). They both differ quite substantially from the MOC produced in the ECHAM6 based simulation. However, proxy-data studies suggest only one primary source of deepwater formation (Tripati and Elderfield 2005; Nunes and Norris 2006), which was located in the high latitudes of the Southern Hemisphere during the Late Paleocene. Based on $\delta^{13}C$ the resting time of water masses in the deep ocean during former time periods can be estimated. "Older" water is enriched in ^{12}C, since the remineralization of organic matter (rich in ^{12}C) leads to an accumulation of CO_2 over time in the deep ocean. According to Miller et al. (1987), no deepwater was formed in the North Atlantic. Instead, the analysis of carbon isotopes from 14 deep sea sites by Nunes and Norris (2006) indicates that the main deepwater

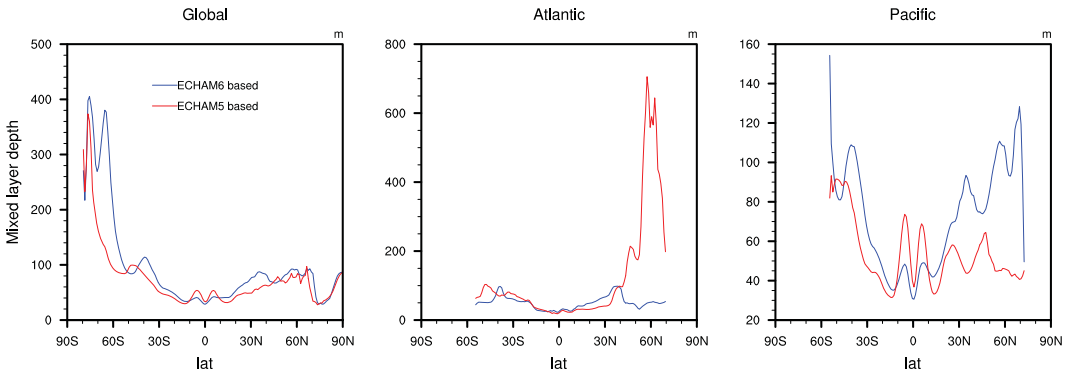

Figure 3.12: Zonally averaged MLD (in m depth), for the global ocean (left), the Atlantic (middle) and the Pacific (right) in the ECHAM6 and ECHAM5 based simulation. Note the different y-axis scales on each plot.

formation took place in the Southern Ocean, but as well in the South Atlantic. Tripati and Elderfield (2005) state that based on their isotope data, the deep ocean overturning must have been mainly driven by convection in the Southern Ocean.

Yet, higher deep sea temperatures in the ECHAM5 simulation are closer to the (temperature) proxy data, which is also resulting from the locations of the deepwater formation areas. The deepwater production in the ECHAM5 simulation takes place between 40-70 °N, where the annually averaged SST is around 20 °C, while the main deepwater formation in the ECHAM6 simulation takes place in the Southern Ocean, south of 60 °S. SST's in that area are below 10 °C in annual average. Consequently the deep ocean is provided with generally colder water.

The annually averaged mixed layer depth (MLD) clearly displays the main deepwater formation areas in the simulation (Figure 3.11). In the Southern Ocean (Pacific and Indian sector) the mixed layer spreads until 900 m depth. In the Northern Hemisphere the maximum MLD is located in the eastern part of the North Pacific (up to ∼300 m depth). In comparison to the ECHAM5 simulation weaker convectional processes in the North Atlantic lead to a much shallower Atlantic MLD in the ECHAM6 simulation (Figure 3.12). Instead the convection in the Southern Hemisphere produces a much deeper MLD than in the ECHAM5 simulation, both in the Pacific and the Indian sector of the Southern Ocean.

3.4 Different states of ocean biogeochemical parameters

3.4.1 Organic carbon cycle

The ocean circulation regimes in the ECHAM5 and ECHAM6 based simulation, produce different biogeochemical states in HAMOCC. The organic carbon cycle in the ECHAM6 simulation is characterized by a higher export of OM and opal from the surface. The export rate of $CaCO_3$ producers is decreased in comparison to the ECHAM5 simulation (Table 3.4). Primarily the sinking and upwelling of water masses, which is determined by the MOC, influences the nutrient concentrations at the surface, and with this the biological production. Especially the distribution of dissolved silicate in the ocean behaves very sensitive to changes in the overturning circulation and can be strongly correlated to the MLD in both simulations (Heinze et al. 2003). Overall, the globally integrated annual mean primary production is slightly increased in the ECHAM6 simulation.

Although, the deepwater formation in the North Atlantic and the deepwater circulation over the whole basin nearly disappears in the ECHAM6 simulation, the shallow ocean circulation in the low and mid latitudes is enhanced. In comparison to the ECHAM5 simulation the resupply of nutrients and especially silicate to the surface is

Key ocean biogeochemsitry properties		
Parameter/Variable	**ECHAM5** based	**ECHAM6** based
Ocean temperature surface (°C)	24.8	23.6
Ocean temperature at 4000 m depth (°C)	8.9	6.8
Ocean salinity	34.31	34.56
Primary production		
Global (Gt C yr^{-1})	58.65	61.91
Export production		
CaCO3 (Gt C yr^{-1})	0.63	0.37
Opal (Tmol Si yr^{-1})	159.57	170.73
POC (Gt C yr^{-1})	8.54	8.99
Molar export ratio		
C(CaCO3):Si(opal)	0.33	0.18
C(CaCO3):C(POC)	0.07	0.04
Si(opal):C(POC)	0.22	0.23

Table 3.4: Overview of key properties characterizing the state of biogeochemical variables for the ECHAM5 and ECHAM6 based simulations.

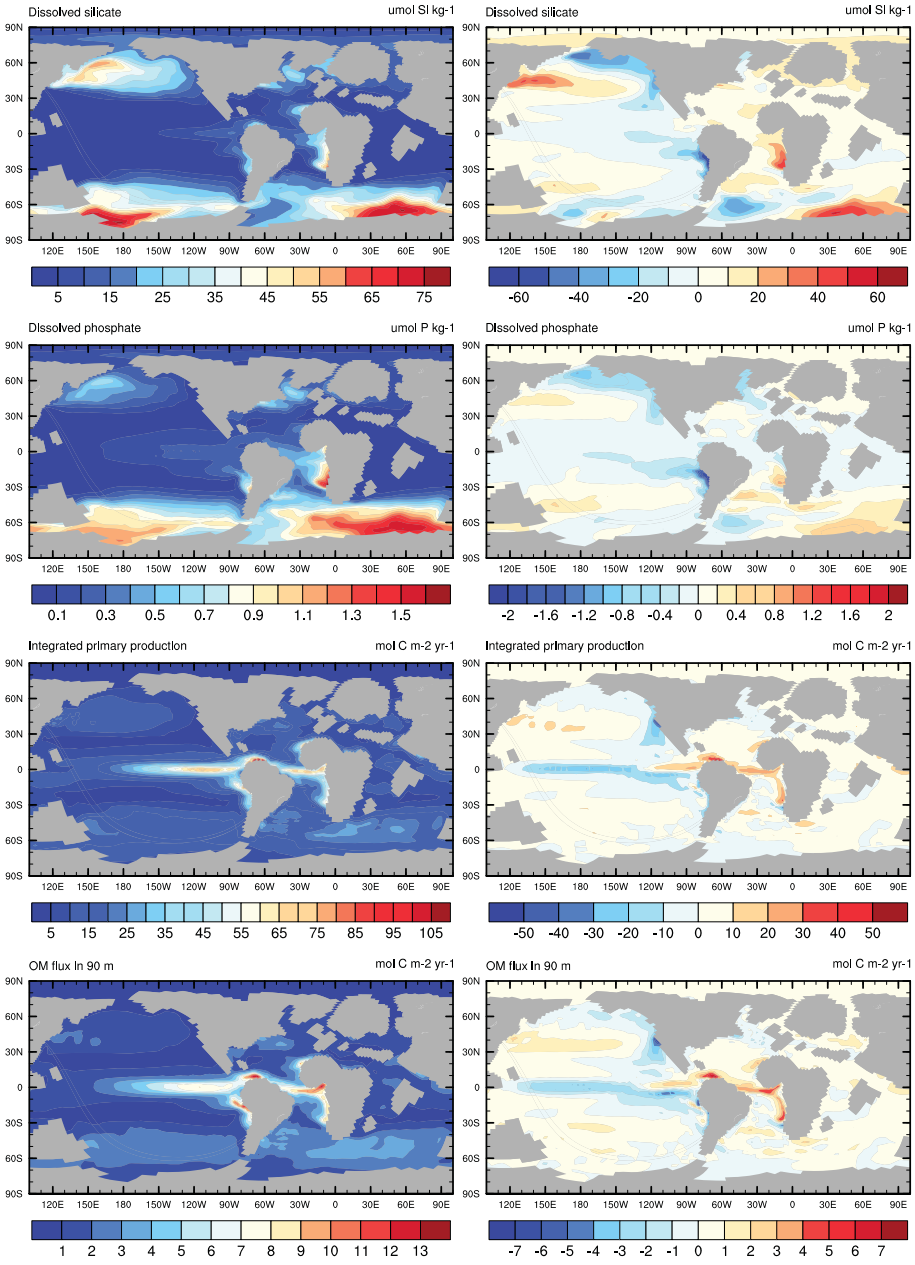

Figure 3.13: Late Paleocene silicate and phosphate concentrations (in μmol Si/P L^{-1}) and annual integrated primary production and OM export in 90 m depth (in mol C m^{-2}) for the ECHAM6 based simulation (left panel) and the difference between the ECHAM6-ECHAM5 based simulation (right panel).

enhanced in the low and mid latitude Atlantic, due to the increased upwelling (Figure 3.13). The increased silicate availability leads to a shift from calcite producers toward opal producers in the Atlantic. The largest differences in Atlantic phosphate and nitrate concentrations in comparison to the ECHAM5 simulation exist directly along the equator and in the eastern boundary coastal upwelling areas. These areas exhibit also the strongest increases in primary production (Figure 3.13). The high latitude Atlantic shows more depleted nutrient concentrations in the surface ocean in comparison to the ECHAM5 simulation. This involves a slight reduction in primary production in the high latitude Atlantic.

The basin averaged depth profiles in Figure 3.14 show a strong increase in Atlantic phosphate and nitrate concentrations which can be attributed to the increased export production and its remineralization (total OM export: 2.18 vs. 1.81 Gt C a^{-1} in ECHAM6 based and ECHAM5 based simulations, respectively). While the export rate (in mol per area) of silicate slightly increases (factor 1.26), the calcite export in 90 m depth is decreased by a factor of 4 in the ECHAM6 based simulation. The increase in remineralization of OM leads to a higher consumption of dissolved oxygen in the subsurface waters. Together with a reduced overturning it results in a stronger OMZ in the Atlantic. The silicate concentrations at depth rather result from opal dissolution in the sediment than from the surface export.

While the Atlantic shows a general increase in export production, less primary production and export of OM takes place in the Pacific (Figure 3.13). The equatorial Pacific shows a reduced MLD in the ECHAM6 simulation (Figure 3.12), which serves as an indicator for reduced upwelling and is reflected in decreased nutrient concentrations in the surface ocean. The wind speed (in 10 m height) over the equatorial Pacific is about 25 % weaker in the ECHAM6 simulation (not shown), which we interpret as one of the main reasons for the reduced upwelling. Within this region the decrease in primary production is strongest. Furthermore, the reduced upwelling of silicate in the central Pacific increases the calcite/opal export ratio strongly. In the mid and high latitude Pacific the increased MLD correlates again to higher nutrient and silicate availability in the surface ocean, favoring opal production. However, the diminished phosphate and silicate concentrations in the eastern boundary currents indicate reduced coastal upwelling in the North and South Pacific. These regions show significantly less export of OM than in the ECHAM5 simulation. Although there are regions in the Pacific where the calcite production decreases (i.e., western equatorial Pacific), the calcite/opal export ratio shows a general increase for the Pacific (averaged over the whole basin) compared to the ECHAM5 simulation.

At depth the increased overturning circulation leads to higher oxygen concentrations in the Pacific and Southern Ocean. Moreover, the reduced export of OM leads to a weaker OMZ, since less material is remineralized. Phosphate and nitrate concentrations show slightly decreased concentrations (Figure 3.14), which is also in line with the lower OM

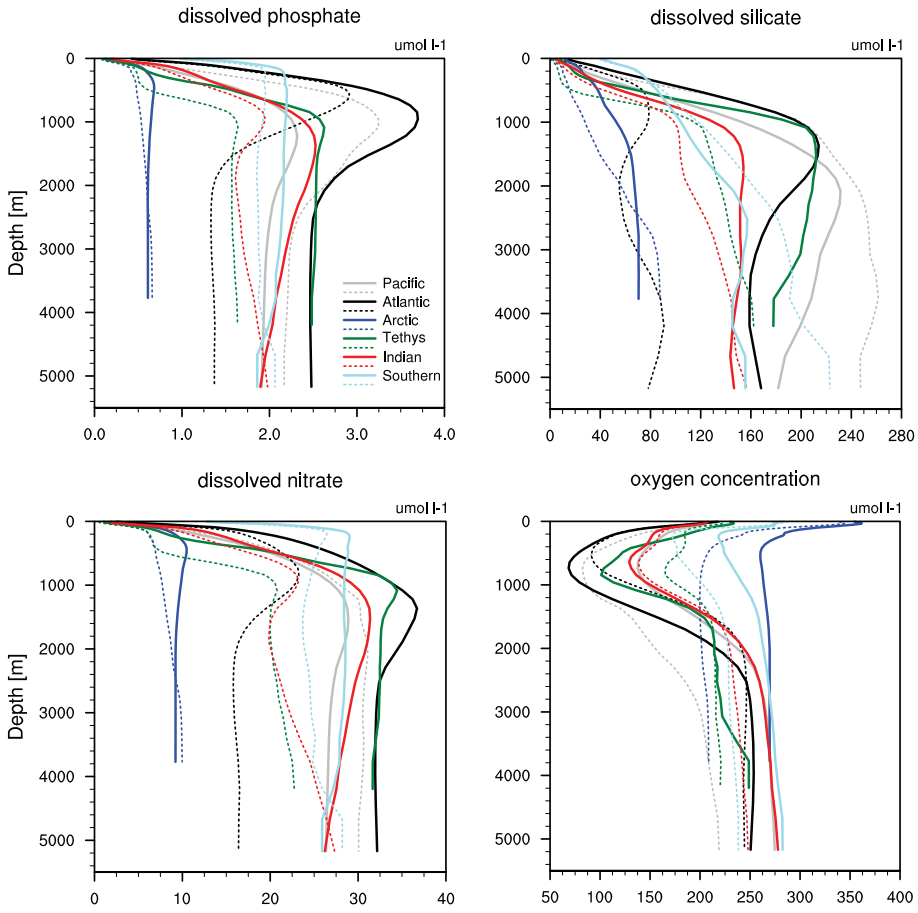

Figure 3.14: Basin-wide averaged phosphate, silicate, nitrate and oxygen concentrations for the ECHAM6 based (solid line) and the ECHAM5 based (dashed line) simulation. All concentrations are given in μmol L^{-1} and are averaged over the last 30 years of the respective simulation.

export in comparison to the ECHAM5 simulation (factor 1.1 decrease).

3.4.2 Inorganic carbon cycle

The Atlantic shows over wide areas higher CO_3^{2-} concentrations in the surface due to a decrease in biological calcite production and export (except in the area of former deepwater formation) in the ECHAM6 based simulation. As a result the TA increases, which potentially increases the carbonate buffer capacity of the surface ocean towards additional CO_2. The former deepwater formation area in the North Atlantic is depleted at the surface in TA, CO_3^{2-}, and DIC in comparison to the ECHAM5 simulation (Figure 3.15). Primarily this is a result of the increased freshwater input which depletes the concentrations respectively. The same is valid for the Arctic Ocean which is less saline in the ECHAM6 setup and therefore has generally much lower concentrations of TA, CO_3^{2-}, and DIC.
The missing inflow of low saline water due to the reversed net exchange with the Atlantic Ocean through Bering Strait leads to increased TA, CO_3^{2-}, and DIC concentrations in the North Pacific. The surface ocean pH does not show any major differences between the two setups in neither of the basins (not shown).

The ocean temperature in 4000 m depth is in global average 2.1 ℃ colder than in the ECHAM5 simulation (Table 3.4). For Ω this results in a higher saturation concentration, i.e., calcite gets into dissolution more easily. Therefore one would expect higher CO_3^{2-} concentrations at depth. However, the calcite export from the surface is in every basin lower than in the ECHAM5 simulation. Consequently there is less calcite available for dissolution which could act as a source for CO_3^{2-} in deeper ocean layers. Nevertheless, the Pacific ocean displays higher concentrations than in the ECHAM5 simulation. This is interpreted as a result of the main deepwater formation area in the Pacific sector of the Southern Ocean. Younger water with lower DIC concentrations characterizes the deep Pacific in the ECHAM6 simulation.
The pH difference of up to 0.3 in the subsurface Pacific (basin averaged, not shown) is a product of the reduced coastal upwelling along the South and North American coast. In these areas the subsurface waters in the ECHAM5 simulation yield the lowest pH as a result of OM remineralization. Also the horizontal extent of these low pH waters is much smaller in the ECHAM6 simulation. Moreover, a better spreading of the CO_2 enriched waters is achieved by the increased mixing of water masses which is induced by the stronger MOC in the Pacific.
The deep Atlantic acts contrarily. Due to increased export and remineralization of OM, as well as a decreased overturning circulation, the deep Atlantic gets enriched in DIC in contrast to the ECHAM5 simulation. The minimum in basin averaged pH (at 900 m depth) is 0.1 lower than in the ECHAM5 simulation (Figure 3.16). The pH decrease in the subsurface Atlantic is attributed to the increased OM remineralization and the reduced mixing.

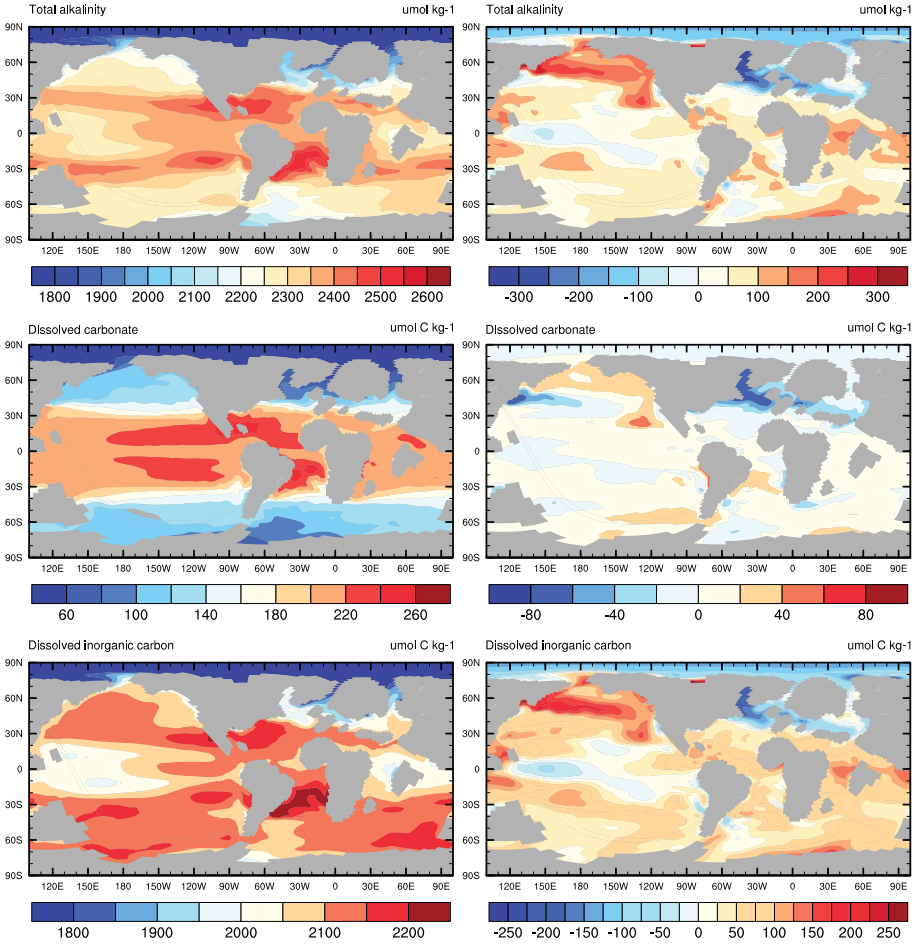

Figure 3.15: Late Paleocene TA concentrations (in μmol kg^{-1}, top row), CO_3^{2-} (in μmol C kg^{-1}, middle row), and DIC concentrations (in μmol C kg^{-1}, bottom row) for the ECHAM6 based simulation (left panel) and the difference between the ECHAM6-ECHAM5 based simulation (right panel).

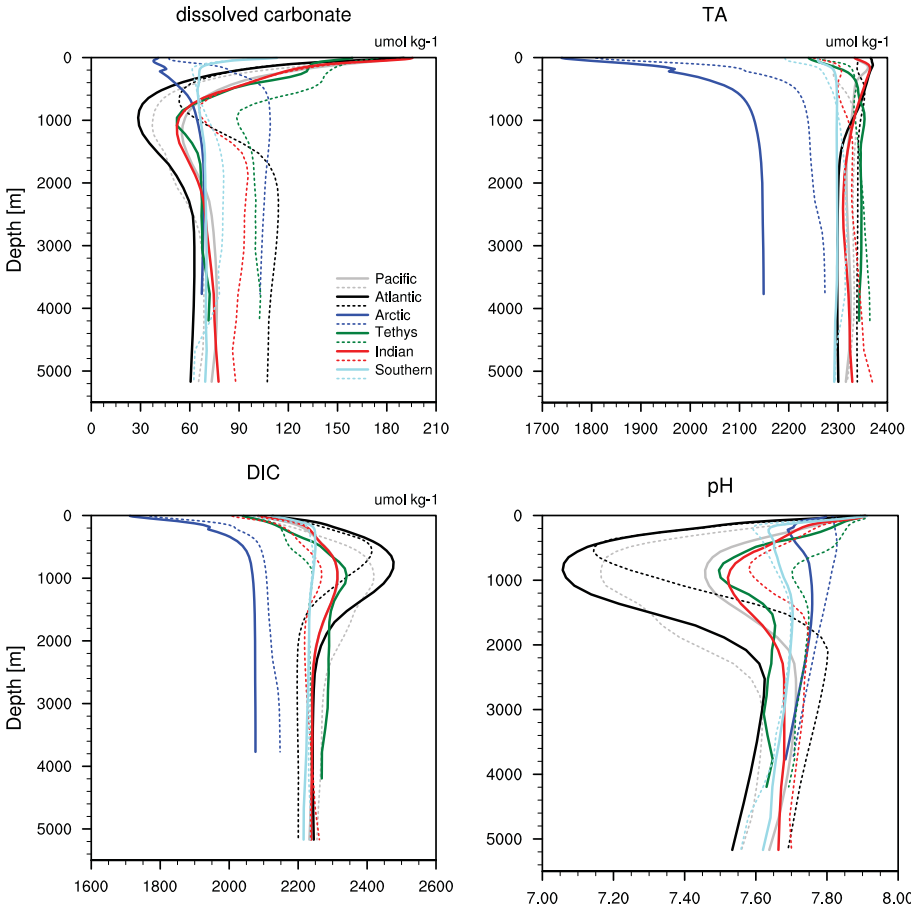

Figure 3.16: Basin-wide averaged carbonate, TA, DIC concentrations and pH for the ECHAM6 based (solid line) and the ECHAM5 based (dashed line) simulation. All concentrations are given in μmol kg^{-1} and are averaged over the last 30 years of the respective simulation.

3.5 Reversed carbonate ion gradient due to different ocean circulation regimes

The Pacific shows generally higher CO_3^{2-} concentrations in the ECHAM6 than in the ECHAM5 based simulation. Especially in the Northern Hemisphere tropics and temperate zones the reduced biological pump leads to higher CO_3^{2-} concentrations in the upper 2000 m of the water column (Figure 3.17). In the Atlantic the lack of North Atlantic deepwater production reduces the CO_3^{2-} concentrations significantly. Through the decrease in deep ocean ventilation the mid and deep ocean gets enriched in metabolic CO_2, resulting in basin averaged CO_3^{2-} concentrations of 60 μmol kg^{-1} (ECHAM5: 105 μmol kg^{-1}). With a basin averaged concentration 75 μmol kg^{-1} (ECHAM5: 65 μmol kg^{-1}) the Pacific ocean shows higher CO_3^{2-} values than the Atlantic. So it is mainly the reduction of CO_3^{2-} in the Atlantic which drives the reversal of the basin ratio in the two model setups. However, the difference between the Pacific and the Atlantic CO_3^{2-} concentrations only amounts to 15 μmol kg^{-1} in the ECHAM6 based simulation, while the difference between the basins is about 40 μmol kg^{-1} in the ECHAM5 based simulation. For comparison, the basin averaged deep sea CO_3^{2-} concentrations for the pre-industrial Pacific and Atlantic (CMIP5, historical run with MPI-ESM) differ by 10 μmol kg^{-1}.

Based on sediment core data, the carbonate compensations depth (CCD, depth at which $CaCO_3$ is no longer found in sediments) has probably not been shallower in the

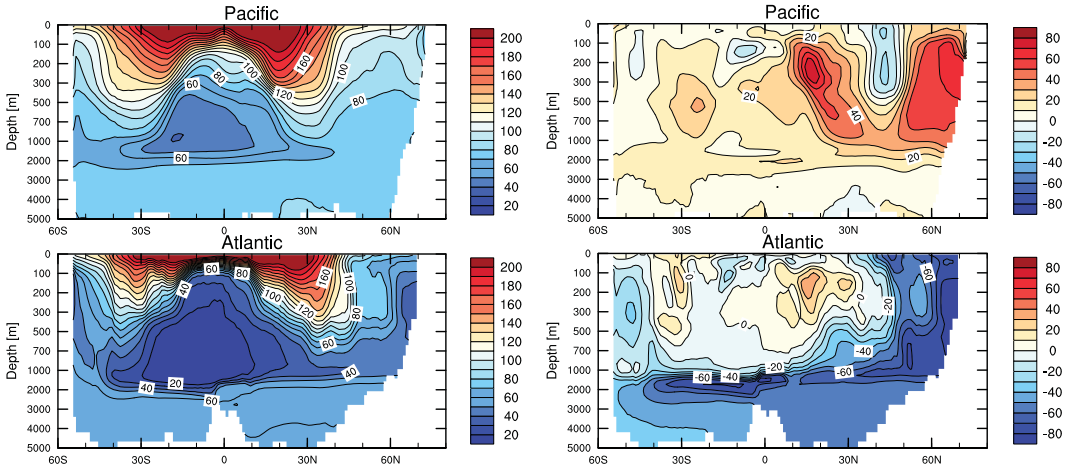

Figure 3.17: Late Paleocene CO_3^{2-} concentrations (in μmol C kg^{-1}) for the ECHAM6 based simulation (left column) and the difference between the ECHAM6-ECHAM5 based simulation (right column).

Atlantic than in the Pacific before the PETM (Zeebe et al. 2009). This does not allow the Pacific CO_3^{2-} concentrations to be much higher than in the Atlantic.
The CO_3^{2-} distribution is a result of the overturning circulation and vertical fluxes of OM and TA due to the biological pump. The Late Paleocene ocean circulation as it is predicted in our simulation (with multiple Southern Hemisphere deepwater sources), results in "older", more DIC enriched deepwaters in the Atlantic than in the Pacific. The corrosiveness of Atlantic bottom water is additionally enhanced by the increased export of OM. Not only the CO_3^{2-} gradients are reversed in our simulation, but also the phosphate, nitrate and oxygen gradients are reversed between Pacific and Atlantic in comparison to today (and the ECHAM5 based simulation) (Figure 3.14).
Another important factor for the CO_3^{2-} concentration at depth is the calcite export from the surface. While in the ECHAM6 simulation, the export of calcite shells in the Pacific is twice as high as in the Atlantic, this ratio is reversed in the ECHAM5 simulation. However, in terms of the calcite export ratio between Atlantic and Pacific, the ECHAM6 simulation for the Late Paleocene is closer to preindustrial conditions (CMIP5, historical run with MPI-ESM).
As the CO_3^{2-} concentration drives the dissolution of deep sea carbonates (Dickens 2000; Zeebe and Zachos 2007) it is an essential property to interpret the proxy record and to infer from it the actual dissolution pattern, i.e., strong shoaling of CCD and saturation horizon in Atlantic and weak shoaling in the Pacific (Dunkley Jones et al. 2010). Based on our results the thermohaline circulation could be one of the main drivers for an increased vulnerability of calcite sediments in the Atlantic during the PETM. The assumption of a reversed basin CO_3^{2-} gradient between the Atlantic and the Pacific relative to the modern was previously made by Zeebe and Zachos (2007). However, they assume it for the dissolution phase of the PETM. Our model results show that the deep-sea CO_3^{2-} basin gradient increased from the Atlantic over the Southern Ocean into the Pacific already in the Late Paleocene.
Other PETM model studies which include ocean biogeochemistry (i.e., Panchuk et al. 2008; Zeebe et al. 2009) prescribe a single Southern Hemisphere deepwater formation in the Indian sector of the Southern Ocean, mainly based on observational data from Thomas et al. (2003). Deepwater formation occurs in this spot in our simulation too, but our simulation shows an additional source of deepwater formation in the Pacific section of the Southern Ocean. Neither the observations (due to missing data points) nor the model studies take into account a second deepwater formation area in the Pacific sector of the Southern Ocean, which we predict in our simulation. Winguth et al. (2010) find in their Late Paleocene simulation, using the Community Climate System Model (CCSM3), a convection induced deepening of the MLD in the same Southern Ocean locations as we do. However, the convection does not trigger Pacific deepwater circulation in his simulation as it is seen in our simulation.
According to Tripati and Elderfield (2005) the Late Paleocene $\delta^{13}C$ values are lower in

the North Pacific than in the Atlantic and the South Pacific, which favors a Southern Hemisphere deepwater formation. This does not exclude deepwater formation in two different locations in the Southern Ocean. Nunes and Norris (2006) also derive from their data a Southern Ocean dominated deepwater formation. However, their study is lacking data points/ measurements in the Pacific section of the Southern Ocean, where our second deepwater formation area is located. Nunes and Norris (2006) further speculate about a ventilation of the deep Atlantic from the Southern Ocean sinking area, which does not occur in our simulation.

3.5.1 Model data comparison for $CaCO_3$ sediment content

Since the sedimentary calcite is highly dependent on the oceanic bottom layer CO_3^{2-} content, we evaluate our simulations against the available sediment record. Figure 3.18 shows the different calcite sediment patterns, achieved by the ECHAM6 and ECHAM5 based simulations. It includes a compilation of $CaCO_3$ wt% data which was derived from Late Paleocene sediments (Panchuk et al. 2008).

The discussed changes in the water column biology and chemistry in the ECHAM6

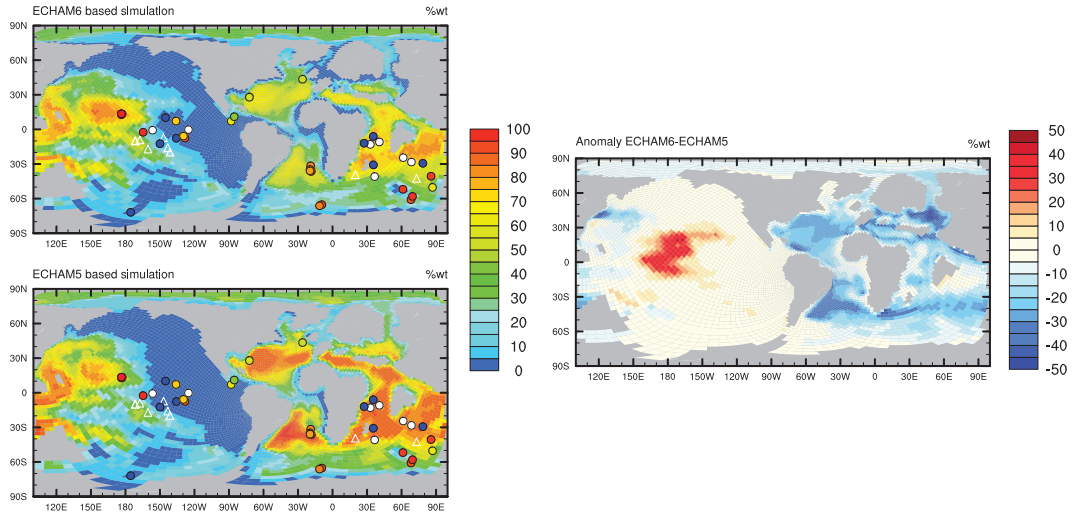

Figure 3.18: Left column: Late Paleocene calcite sediment content (in wt%) for the ECHAM6 and ECHAM5 based simulation, including observational data points from (Panchuk et al. 2008): colored dots indicate wt%, white dots indicate that $CaCO_3$ is present but wt% is unknown, triangles indicate a hiatus (due to non-deposition). Right column: difference between the ECHAM6-ECHAM5 based simulation. Calculations are based on 100 year averages.

based simulation result in a decrease in South Atlantic calcite sediments. This result does still reasonably match the calcite content, which is observed in the sediment record from Walvis Ridge (Zachos et al. 2005). The North Atlantic $CaCO_3$ wt% in the ECHAM6 based configuration matches the sediment record even better than in the ECHAM5 simulation. In the Pacific the horizontal expansion of calcite sediments matches the sedimentary record better, too. However, calcite sediments could still cover a wider area of the ocean floor in the Central Pacific than projected in our simulations. Although, the close vicinity of sediment cores bearing calcite wt% reaching from 0 to 95 wt% suggests that local heterogeneity's such as ridges and valleys play a major role in the Central Pacific. These may not be represented sufficiently in our model bathymetry. In the Indian sector of the Southern Ocean we see small to no changes in the calcite content between the ECHAM5 and ECHAM6 simulations (both 45 wt%). Both simulations are deviating from the available sediment core data (93 wt%), due to reasons which are already discussed in Chapter 2. For the Indian Ocean the ECHAM6 simulation predicts over widest areas a lower $CaCO_3$ content than in the ECHAM5 simulation, but areas free of $CaCO_3$ are not calculated either.
Zeebe et al. (2009) studied sediment cores of drilling sides in several ocean basins to derive the CCD in the pre-PETM setting. The analysis of the calcite content before the PETM suggests a basin-wide averaged CCD for the Pacific and Atlantic which is very close to each other, between 3.3 and 4 km depth. Due to their interpretation the Atlantic CCD must have been slightly beneath the CCD in the Pacific before the PETM started. However the basin-wide averages rely on 5 sediment cores from the Walvis Ridge for the Atlantic, and 3 sediment cores from the Central Equatorial Pacific and from Shatsky Rise for the Pacific. Our methods do not enable us to deduce the CCD directly out of our model, but the reversed CO_3^{2-} gradient would rather promote a CCD of similar depth in the Atlantic and the Pacific before the PETM.

3.6 Summary & Discussion

We compare two different model setups for reproducing Late Paleocene climatic conditions. In our analysis and evaluation of the model results we focus on the ocean biogeochemistry and discuss how it is affected by the respective states of climate and ocean circulation. The main differences between the two setups consists of differences in the shortwave radiation schemes, the treatment of land surface and vegetation, the parameterization of surface ocean albedo, and the representation of the upper atmosphere.

The predicted surface temperature between the ECHAM5 (Heinemann 2009) and the ECHAM6 based model simulation amounts to ∼2 ℃. The analysis with a zero dimensional energy balance model (EBM, Heinemann et al. 2009) assigns those temperature differences mainly to the atmospheric water vapour content (-20 %) which results in a reduced greenhouse effect in the ECHAM6 based simulation. While the planetary albedo reduction leads to a warming of 1.4 K, the increased longwave emissivity cools the climate by 3 K, resulting in cooler surface temperatures in the ECHAM6 based simulation.

The globally averaged pole to equator temperature gradient is not affected by the differences in the two simulations. The vegetation model influences temperatures regionally, especially over the simulated desserts in central Asia and the Southern Hemisphere subtropics. Due to changes in surface properties and the colder mean climate state the precipitation and wind patterns (absolute and locally) change.

The general ocean circulation state is distinctly different between the two setups. Besides reversed horizontal exchange rates between several ocean basins, it is particularly the MOC which drives severe change in the ocean circulation and biogeochemistry. The ECHAM5 based simulation produces a MOC which is more similar to modern conditions (Jungclaus et al. 2013), including the main deepwater formation in the North Atlantic. Moreover, it features a source for deepwater in the Pacific sector of the Southern Ocean. However, reconstructions of Late Paleocene circulation and deepwater formation areas, based on isotopic analysis of Late Paleocene sediments (Miller et al. 1987; Tripati and Elderfield 2005; Nunes and Norris 2006) and fish tooth (Thomas et al. 2003) promote a Southern Ocean driven deep ocean overturning. In the ECHAM6 based simulation, the ocean circulation system is driven by multiple deepwater formation areas in the Pacific and Indian sectors of the Southern Ocean. No deepwater formation takes place in the Atlantic, which experiences a six times higher freshwater input than in the ECHAM5 simulation. Moreover, the outflow of subtropical waters from the Atlantic into the Pacific (reversed in ECHAM5 based simulation) via the Central American Seaway reduces North Atlantic surface salinities. The influence of the Central American Seaway on the reduction of the AMOC is also predicted by Mikolajewicz et al. (1993); Mikolajewicz and Crowley (1997) for a modified present-day setup.

The simulated deep sea temperatures are closer to the temperature reconstructions (Tripati and Elderfield 2005) in the ECHAM5 based simulation. As a consequence of high latitude formation and sinking of water masses in the ECHAM6 based simulation (mid latitudes deepwater formation in ECHAM5 based simulation), the globally averaged deep ocean (at 4000 m depth) is 2.1 ℃ colder than in the ECHAM5 based simulation.
In consequence of the different ocean circulation state, the low latitude Pacific in the ECHAM6 based simulation is characterized by a shallower MLD indicating decreased upwelling of water masses, whereas, the opposite applies to the high latitude Pacific. In the Atlantic the upwelling of water masses is enhanced in the tropical and subtropical Pacific Ocean.
The ocean biogeochemistry is strongly affected by the different circulation states. The ECHAM6 based simulation shows in comparison to the ECHAM5 based simulation:
(1) A decrease in total $CaCO_3$ export and a reversal of the $CaCO_3$ export gradient between Atlantic and Pacific. While the Pacific is facing an increase in $CaCO_3$ export, the Atlantic exhibits a decrease in $CaCO_3$ export rate.
(2) An overall increase in primary production (6 %) and a reversal in OM export between Pacific and Atlantic, featuring higher OM export (in mol per area) in the Atlantic than in the Pacific.
(3) Increased respiration of OM in the Atlantic which causes higher consumption of oxygen in the subsurface waters. Together with the decreased ocean mixing the OMZs intensify and (metabolic) DIC concentrations get enriched in the Atlantic. The enrichment in metabolic CO_2 due to the lack of North Atlantic deepwater production decreases the CO_3^{2-} concentrations at depth.
(4) Younger and thus better oxygenated water in the Pacific, which exhibits lower DIC concentrations. In the deep Pacific the CO_3^{2-} concentrations are slightly increased due to better ventilation in comparison to the North Atlantic driven circulation state in the ECHAM5 based simulation.
As a result (of points 1-4) a horizontally reversed CO_3^{2-} gradient between Atlantic and Pacific establishes in the ECHAM6 based simulation, in comparison to present-day conditions.
As stated above the $CaCO_3$ export from the surface influences the deep sea CO_3^{2-} concentration as well. The export of $CaCO_3$ is twice as high in the Pacific than in the Atlantic in the ECHAM6 based simulation, while the opposite applies to the ECHAM5 based simulation. Also in pre-industrial model simulations (CMIP5, historical run with MPI-ESM) the Pacific $CaCO_3$ export exceeds the one in the Atlantic (in mol per area). The ECHAM6 based simulation, results in lower sedimentary $CaCO_3$ deposition in the Atlantic, Tethys and Indian Ocean, while the $CaCO_3$ content is increased in the central Pacific sediments. We compare the $CaCO_3$ sediment distribution resulting from the reversed deep-sea CO_3^{2-} gradient between Pacific and Atlantic in the pre-PETM

state to a compilation of $CaCO_3$ wt% which is based on the Late Paleocene sediment record (Panchuk et al. 2008). The increase in Central Pacific $CaCO_3$ deposits in comparison to the ECHAM5 based simulation matches the observations better, as well as the simulated North Atlantic $CaCO_3$ distribution.
The CO_3^{2-} gradient between Atlantic and Pacific is reproduced without some secondary control on the pattern of carbonate dissolution, considering the diverse physical and biogeochemical boundary conditions of the Late Paleocene. With the Southern Ocean driven ocean circulation we give a plausible explanation for a horizontally reversed deep-sea CO_3^{2-} gradient between Pacific and Atlantic which can be identified from the proxy record (Zeebe and Zachos 2007).

Chapter 4

Perturbation of the marine carbon cycle during the onset of the PETM

4.1 Introduction

In this chapter we prescribe different carbon concentration increase scenarios (Table 4.1) to simulate the onset of the PETM. To achieve modeling results which are consistent with the negative δ^{13}C carbon isotope excursion (CIE) and the dissolution of marine carbonates which characterize the PETM sediment record (Zachos et al. 2005), several possible carbon emission scenarios are discussed for the PETM (e.g., Pagani et al. 2006a; Zeebe et al. 2009). We are starting our simulation from the (coupled ECHAM6 based) pre-PETM state which is described and discussed in Chapter 3. The prescribed CO_2 scenarios for the PETM perturbation (0.47-0.71 ppm yr^{-1}) represent the upper limit of equivalent carbon emission rates (1-1.5 Gt C yr^{-1}) estimated for the PETM. Whereas, studies including carbon cycle models (Panchuk et al. 2008; Zeebe et al. 2009; Ridgwell and Schmidt 2010) rather prescribe emissions at the lower end of possible emission rates ($\sim$0.5 Gt C yr^{-1}) to reproduce the PETM related carbon isotope excursion (CIE).

For the onset of the PETM a reduction in deepwater formation in the southern high latitudes is discussed (Tripati and Elderfield 2005; Nunes and Norris 2006), as well as a possible switch of deep water formation from southern to northern high latitudes which could have induced mid depth and deep ocean warming (Bice and Marotzke 2002). Carbon cycle modelling studies of the PETM did not account for transient changes in the ocean circulation in response to the carbon perturbation so far. Panchuk et al. (2008) did not predict a weakening in Southern Ocean deep water production during the onset of the PETM. Zeebe et al. (2009) prescribed a weakening in Southern Ocean ventilation, but therefore ventilated the deep ocean via a North Pacific source (Zeebe et al. 2009). Against this background we want to study the response of ocean circulation to the PETM carbon perturbation with a complex ESM including ocean biogeochemistry,

Conducted CO_2 emission scenarios

PETM scenarios	Description	atm. CO_2 incr. (p.a.)	Acc. emission after 1300 yrs	Duration (yrs)
control	Late Paleocene climate state (560 ppm)	-	-	1000
high	Atm. CO_2 increase equal to 1.5 Gt C yr^{-1}	0.71 ppm	1950 Gt C	1500
medium	Atm. CO_2 increase equal to 1 Gt C yr^{-1}	0.47 ppm	1300 Gt C	3000
ocean source	*medium* + 0.5 Gt C yr^{-1} source in deep Atlantic.	0.47 ppm	1950 Gt C	1500
no warming	*medium* but CO_2 increase not visible for radiation. Only biogeochem. coupled.	0.47 ppm	1300 Gt C	1500

to gain further knowledge about the implications of changes in ocean circulation on the marine biology and carbon cycle during the event.

By analyzing ocean biogeochemical consequences of ocean circulation changes we focus on possible reasons which could have led to the benthic extinction event during the PETM (Kennett and Stott 1991; Thomas and Shackleton 1996). Several mechanisms, such as changing oceanic productivity, lowered oxygenation, or carbonate corrosivity are discussed as reason for the benthic extinction (Thomas 2007). It is not proven that any of these reasons occurred on a global scale, but most studies suggest that multiple stressors acted simultaneously (e.g., Ridgwell and Schmidt 2010). As our approach accounts for nearly all of the discussed stressors, we analyze their impact on the deep ocean habitat and evaluate if the extinction could have been triggered by an interaction of the above-mentioned processes.

Furthermore, we want to investigate how a deep ocean carbon source would have affected the ocean carbon cycle and especially sedimentary $CaCO_3$ dissolution during the PETM. Since a release of e.g., 2000 Pg C from methane hydrate could explain the CIE it is therefore intensively discussed to have triggered the PETM (Dickens et al. 1995). Moreover, modeling studies suggest that an additional emission of carbon to the deep ocean is necessary to reproduce the PETM dissolution record (Zeebe et al. 2009).

One of the most important proxies proving rapid atmospheric CO_2 increase and ocean acidification during the PETM is the sedimentary $CaCO_3$ dissolution record. The carbonate compensation depth (CCD) shoaled substantially during the onset of the PETM (Bowen et al. 2004). However, $CaCO_3$ dissolution did not occur uniformly throughout the basins (Thomas et al. 2002; Zachos et al. 2005), the CCD record implies strong $CaCO_3$ dissolution (CCD shoaling of 2 km) in the Atlantic and relatively weak disso-

lution (CCD shoaling of several 100 m) in the Pacific (Zeebe et al. 2009). We analyze how different rates of carbon release affect the deep ocean and surface ocean carbonate chemistry and compare our results to available proxy data.

This chapter is organized as follows. After introducing the experimental setup in Section 4.2 we describe the response of the climate system to a PETM related carbon perturbation (*medium* scenario), with emphasis on the ocean biogeochemistry in Section 4.4. In Section 4.5 we study the systems sensitivity towards different amounts (*high* scenario) and locations (*ocean source* scenario) of CO_2 sources. In Section 4.6 we separate warming induced and carbon induced effects on the ocean biogeochemistry (*no warming* scenario) during the onset of the PETM. The results are summarized and discussed in the context of existing model and data studies in Section 4.7.

4.2 Scenario design

We simulate the onset of the PETM with the the MPI-ESM, including the atmospheric general circulation model ECHAM6, the ocean general circulation model MPIOM, the ocean biogeochemistry model HAMOCC and the land surface and vegetation model JSBACH (for a detailed model description see Section 3.2). To replicate a carbon perturbation which is associated with the PETM, we run several CO_2 emission scenarios. We prescribe a yearly atmospheric CO_2 increase of 0.47 ppm in the *medium*, *ocean source* and *no warming* experiment. In the *high* experiment we prescribe a yearly atmospheric CO_2 increase of 0.71 ppm (Figure 4.1). All experiments start from the ECHAM6 based Late Paleocene background state (560 ppm CO_2). The atmospheric CO_2 concentration is linearly increased over a period of 1300 years, which results in a CO_2 concentration in the atmosphere of 1171 ppm for the *medium*, *ocean source*, *no warming* and 1483 ppm for the *high* experiment. The simulations are then calculated with fixed atmospheric CO_2 concentrations for another 1700 years in the *medium*, and another 200 years in the *ocean source*, *no warming* and the *high* experiment (Figure 4.1).

The atmospheric CO_2 increase in the *medium* scenario is equivalent to an emission of 1300 Gt C (1950 Gt C in *high* scenario), not considering land and ocean carbon uptake. The carbon fluxes between atmosphere, ocean and land are diagnosed but not calculated interactively, as we prescribe the time-evolution of atmospheric CO_2 as an input to the model. Consequently, changes in the land and ocean carbon storage do not feedback on the atmospheric CO_2 concentration or on the climate. The fixing of the atmospheric CO_2 concentration at 1171 ppm (1483 ppm) assumes a constant net emission of carbon, since in an interactively calculated simulation, the ocean and land carbon uptake would decrease the atmospheric CO_2 concentration over time.

The *ocean source* emission scenario consists of an annual atmospheric CO_2 increase of 0.47 ppm and an additional carbon source of 0.5 Gt C yr^{-1} in the deep Atlantic in >1000 m depth (see model description in Section 3.2.4). The equivalent emission of carbon therefore amounts to 1950 Gt C in this scenario, 1300 Gt C is added in the atmosphere and 650 Gt C is added in the deep ocean. An emission of CO_2 to the deep ocean due to oxygenation of methane hydrate (CH_4) during the PETM is discussed in several publications (e.g., Dickens et al. 1995; Thomas et al. 2002; Zeebe et al. 2009).

In the *no warming* experiment the prescribed atmospheric CO_2 increase is just visible for the land and ocean biogeochemistry models. The radiation in the model is fixed at 560 ppm and is not influenced by the CO_2 increase. Consequently, the surface temperature is not increasing due to radiative effects. This is a common approach to characterize feedbacks in the coupled carbon-climate system, which is also done for the simulations of the Coupled Model Intercomparison Project (CMIP5) experiments (e.g., Friedlingstein et al. 2006; Arora et al. 2013; Schwinger et al. 2014).

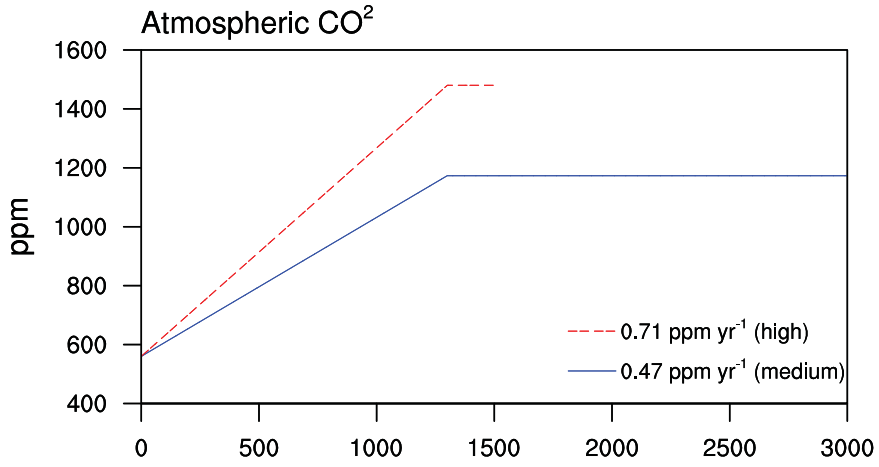

Figure 4.1: Prescribed atmospheric CO_2 emission scenarios for the onset of the PETM. Scenarios represent the assumption of a *high* (0.71 ppm yr^{-1}) and a *medium* (0.47 ppm yr^{-1}) rate of atmospheric CO_2 concentration increase.

The *no warming* simulation is compared to the *medium* emission scenario, to isolate/study climate change induced effects on the ocean biogeochemistry. After Friedlingstein et al. (2006) the *medium* simulation corresponds to the "coupled" state in which climate change and atmospheric CO_2 increase affect the carbon cycle. The *no warming* simulation corresponds to the "uncoupled" or "biogeochemically coupled" state in which CO_2 is treated as an nonradiatively active gas.
In the *high* emission scenario the atmospheric CO_2 concentrations are increasing faster and are fixed on a higher CO_2 level (after 1300 years), than in the *medium* scenario.

4.3 Changes in ocean circulation

The atmospheric CO_2 increase from 560 to 1171 ppm causes the SST to increase by ~5 °C in global average over 1300 years (Figure 4.2 & 4.6). After stabilization of the atmospheric CO_2 concentration at 1171 ppm, the SST increases by another 1.5 °C until the year 3000. However, the SST seems not to be in equilibrium yet. The temperature increase is strongest in the equatorial and polar regions (Figure 4.2). High latitude SST's increase by 8 to 10 °C, which is in accordance with most of the observational studies (Zachos et al. 2005, and references therein). Sluijs et al. (2006) rather predict a warming of only 5 °C in the Arctic Ocean, but starting from a more equable meridional temperature gradient in the pre-PETM climate state. However, our simulated annually averaged SST of 12 °C in the Arctic Ocean after the atmospheric CO_2 increase matches at least the temperatures inferred from high latitude proxies (Sluijs et al. 2006) during the event better. The meridional temperature gradient flattens throughout the simulation. While temperatures increase by 8 °C and 10 °C in the Southern and Arctic Ocean respectively, SST's rise by only 6 °C in the tropics.

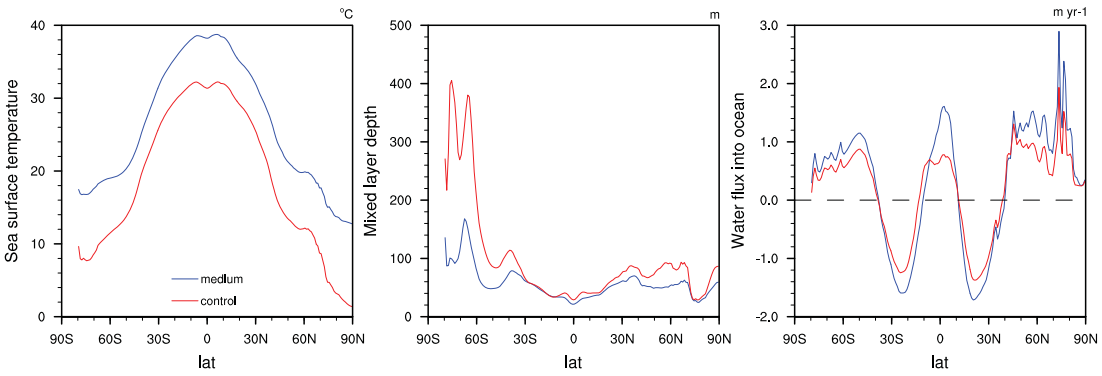

Figure 4.2: Zonal mean SST (°C), MLD (m) and freshwater flux into the ocean (m yr^{-1}) averaged over the last 30 years of the *medium* CO_2 emission scenario and the control run.

The zonally averaged MLD is everywhere shallower than in the background climate state. Especially in the Southern Hemisphere high latitudes the MLD shoales strongly. The Pacific sector of the Southern Ocean exhibits a MLD which is ~500 m shallower than in the control run (Figure 4.3). While it looks similar for the Indian sector, the MLD in the Atlantic sector of the Southern Ocean is deeper than in the control run. A decrease in deep convection reduced the MLD in the Indian sector of the Southern Ocean. However, convectional processes spread in the spatial extent, indicated by a deepening of the MLD in the Atlantic sector of the Southern Ocean. The net freshwater

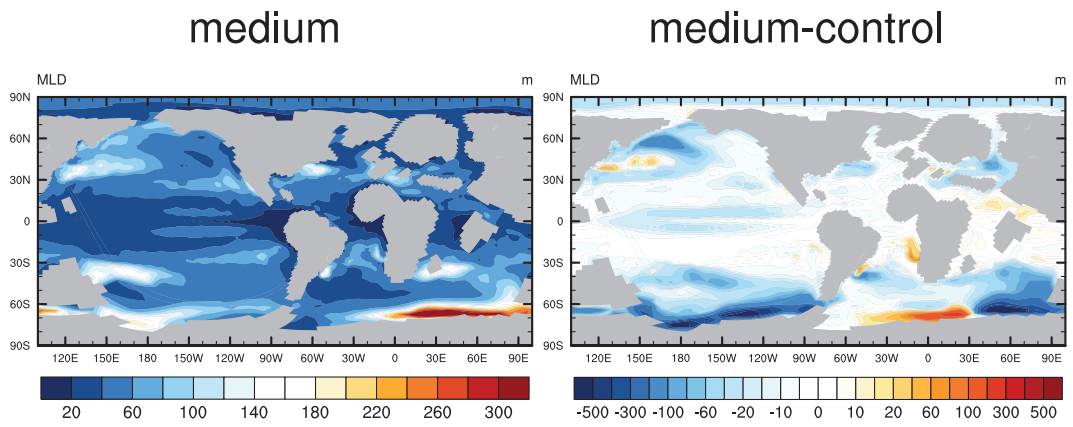

Figure 4.3: Left: MLD averaged over the last 30 years of the *medium* CO_2 emission scenario. Right: difference of the *medium* experiment and the control run (note the non-linear color bar).

flux into the ocean increases due to the prescribed CO_2 forcing, which is in accordance to the reduced MLD in the deepwater formation areas.
In general the tropics and mid to high latitudes experience a greater fresh water input, while in the subtropics the net loss of freshwater due to evaporation is increased. The northern mid to high latitude increase in freshwater input (Figure 4.2) takes primarily place in the Pacific. Figure 4.5 highlights the net freshwater input over the deep water formation areas in northern and southern high latitudes. The North Pacific (40-70 °N) freshwater input increases by 25 % and equilibrates at ∼4 Sv after 1500 years. The freshwater input into the North Atlantic (40-70 °N) increases only slowly over the first

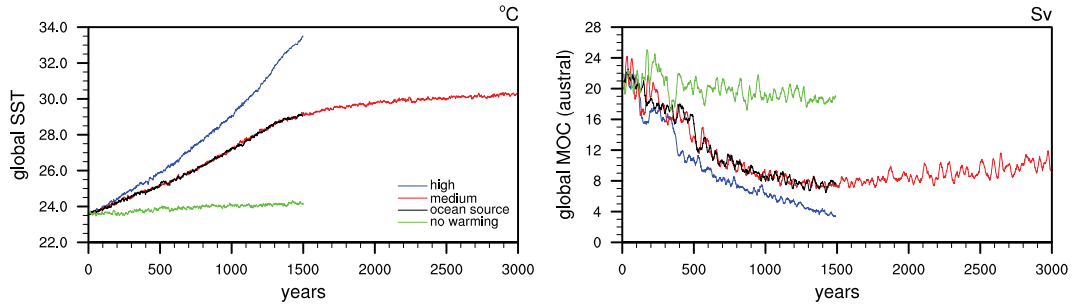

Figure 4.4: Key variables of ocean physical state for all simulations. Temporal evolution of averaged SST (°C, left) for the global ocean and maximum MOC (below 1000 m depth) for the Southern Hemisphere (Sv, right).

500 years. This period coincides with the initial strengthening of the MOC in the Atlantic (Figure 4.6). However, after 3000 years the freshwater input increased about 17 %. The areas of deepwater formation in the Southern Hemisphere in the Pacific sector and Indian sector of the Southern Ocean (both 60-80 °S) show an increase in freshwater input of 45 % and 33 % after 3000 years. Both areas respond rather quickly to the CO_2 forcing, but the freshwater input in the Pacific sector of the Southern Ocean exhibits an increase from year 2700 again. The Atlantic sector is the only region in the Southern Ocean which reveals a decrease in freshwater input in response to CO_2 increase and warming. Over a period of 500 years it decreases about 12 %, but then increases again to about 25 % above its initial value.
In response to surface warming and freshwater input, the MOC drops abruptly in the Southern Hemisphere. The maximum MOC weakens from 24 Sv to a minimum value of 8 Sv in year 1500 after the onset of the carbon perturbation. From this point on it seems to recover slowly, due to some strengthening of deep convection in the Indian and Atlantic sector of the Southern Ocean. We expect the MOC to reach a new equilibrium as soon as both, not only the CO_2 but also the freshwater forcing become stationary, since a similar behavior was detected by Li (2012). Li (2012) used the MPI-ESM in the present-day setup and prescribed a linear atmospheric CO_2 increase, similar to our CO_2 increase scenarios, starting from pre-industrial conditions. In response to a CO_2 increase over 2000 years the Atlantic meridional overturning circulation (AMOC) decreased by 55 % in his simulation. Following the CO_2 increase phase, atmospheric CO_2

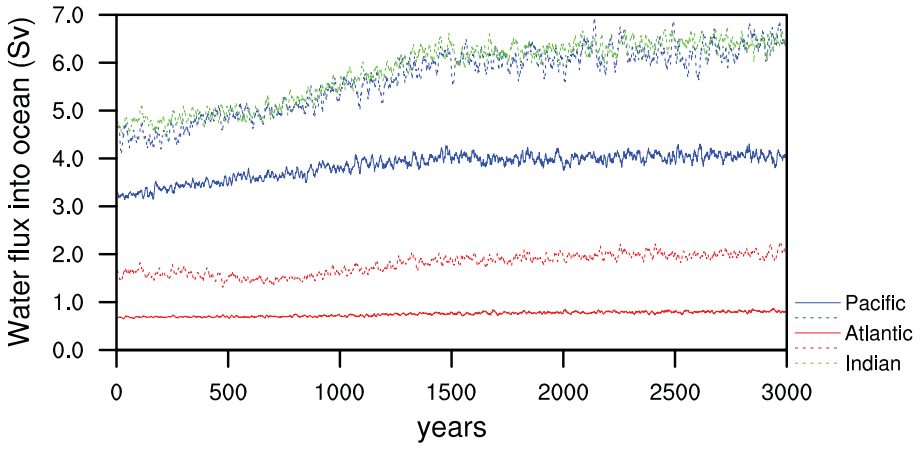

Figure 4.5: Timeseries of the net freshwater flux (precipitation - evaporation + runoff) into the ocean (in Sv) over the North Atlantic and North Pacific (both 40-70°N, solid lines), and over the Pacific, Atlantic and Indian Ocean section of the Southern Ocean (dashed lines) for the *medium* CO_2 emission scenario.

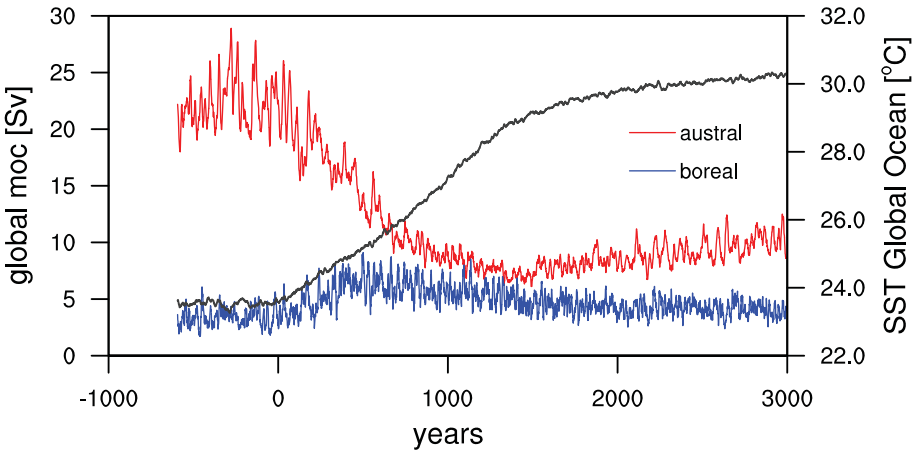

Figure 4.6: Timeseries (10 year running mean) of the maximum MOC (below 1000 m depth, blue and red lines correspond to the Northern and Southern Hemisphere, respectively) and the SST (global, black line) for the *medium* CO_2 emission scenario. Negative values on the x-axis correspond to the steady state in the control run.

concentrations were held constant over a period of 5500 years, which gave the system much more time to equilibrate. His results show that the MOC does only slightly resume to ∼65 % of its initial strength (to become stationary) after approximately 2000 years, but does only fully recover by decreasing the atmospheric CO_2 concentrations again. In the Northern Hemisphere the MOC is strengthening in response to the CO_2 forcing from 3 Sv in the pre-PETM to 7 Sv after 400 years of CO_2 increase. Around year 700 (CO_2 increase 330 ppm and SST increase of 1.8 °C) the MOC starts weakening again. The temporary Northern Hemisphere MOC strengthening is occurring equally in the Pacific and the Atlantic Ocean.

Figure 4.7 displays that principally below 2000 m no deep water formation takes place anymore. An intensification of the hydrological cycle and especially an increase in high latitude freshwater input due to PETM warming are dealt as the main reasons for the ocean stratification (Huber et al. 2003). The generally weaker MOC and the shallower convection, which result from our simulation are consistent with the reconstructions from the proxy record. The isotopic and paleo-temperature proxy record indicates greater stratification and weaker thermohaline overturning during the PETM (Tripati and Elderfield 2005; Nunes and Norris 2006). As a consequence the Southern Hemisphere dominated MOC and with it the deep ocean ventilation collapsed. However, a switch from Southern Ocean sinking to Northern Hemisphere sinking (Nunes and Norris 2006) is just occurring over a period of ∼700 years in our simulation (Figure 4.6). Generally, the proxy record leaves room for speculation regarding changes in deep

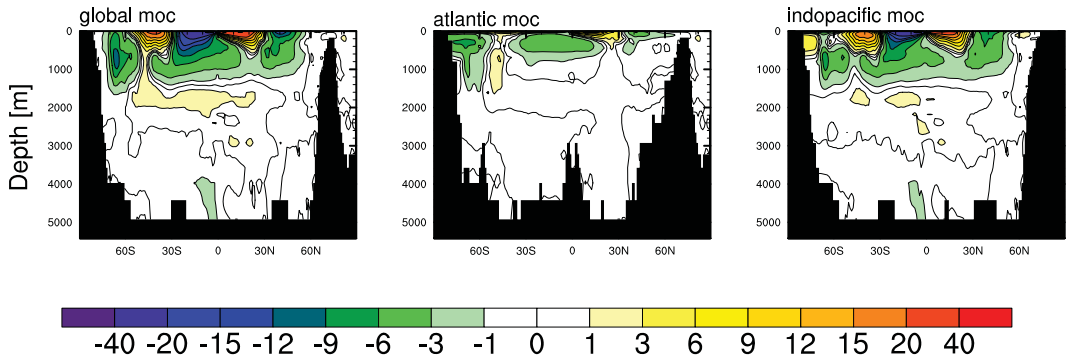

Figure 4.7: Streamfunction of the MOC during the last 100 years of the *medium* CO_2 emission scenario for the global, Atlantic, and Indopacific Ocean.

water formation areas in response to the carbon perturbation. Thomas et al. (2003) suggest that the main source for deep water ventilation was located in the Southern Ocean, before and during the PETM. The temporary increase in Northern Hemisphere deepwater formation in our simulation also shows the sensitivity of the model towards CO_2. A slower CO_2 increase might enable a stable deepwater formation in the Northern Hemisphere during the PETM.

4.4 Changes in ocean biogeochemistry

4.4.1 Nutrients & oxygen distribution - implications for marine biology

Nutrients

The surface ocean shows a general depletion in nutrients in response to (warming resulting from) the *medium* CO_2 increase scenario (Figure 4.8), although, the distribution pattern is still very similar to the pre-PETM conditions. The tropics and subtropics are poorer in surface phosphate concentrations than the temperate zones. Except the regions which are controlled by the eastern boundary currents in the South Pacific and South Atlantic, which show the highest phosphate concentrations at the surface in our simulation. This shows that the nutrient supply due to Ekman-induced upwelling along the coasts of South America in the Pacific and the African coast in the Atlantic is not reduced much. At 20° N along the northwestern coast of Africa the upwelling of nutrients is even increased in comparison to the control run. The decrease in phosphate concentrations is strongest in the Southern Ocean, especially in the Indian and Pacific sector where convection induced sinking of water masses occurred in the pre-PETM state. Also the North Atlantic and the North Pacific display smaller reductions in surface phosphate concentrations (Figure 4.8). The reduced meridional surface temperature gradient and the precipitation induced salinity decrease lead to a stronger stratification of the ocean, bringing less nutrients back to the surface ocean.

Figure 4.9 displays how the surface and subsurface waters of the Pacific and the Atlantic become depleted over time. The former recycling of nutrients within the first

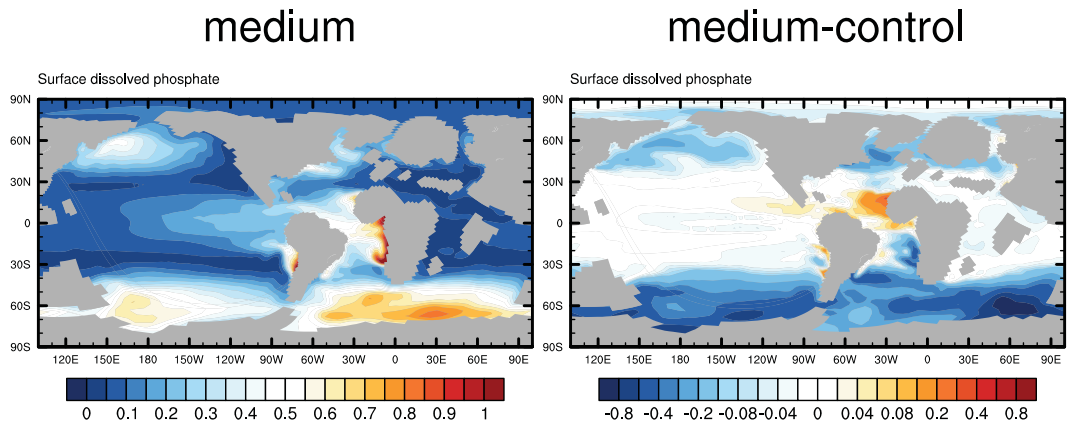

Figure 4.8: Left: phosphate concentrations in μmol L^{-1}, averaged over the last 30 years of the *medium* CO_2 emission scenario. Right: difference of the *medium* experiment and the control run (note the non-linear color bar).

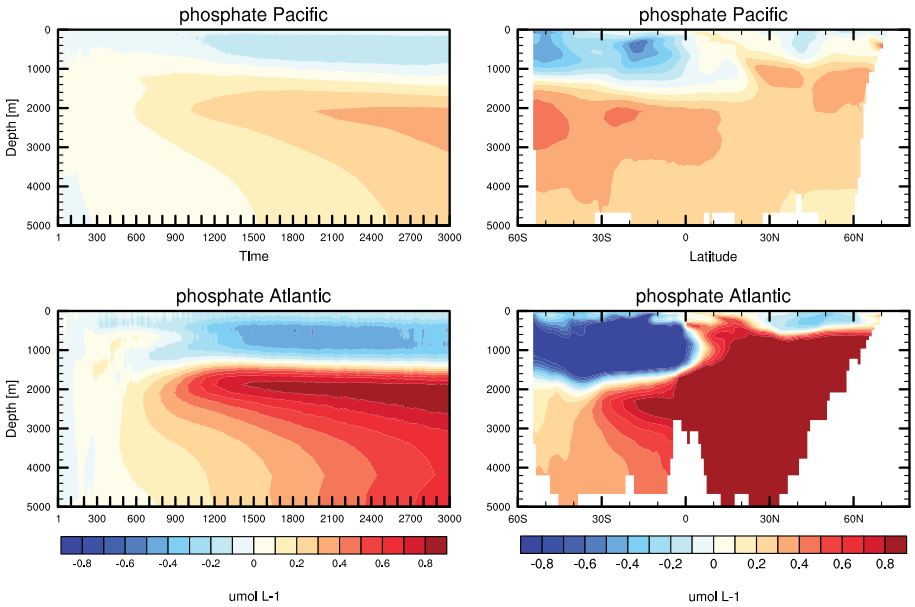

Figure 4.9: Left panel: Temporal evolution of anomaly (*medium*-control) in phosphate concentrations over time, integrated over the whole Pacific and Atlantic (μmol L^{-1}). Right panel: Zonally averaged anomaly (*medium*-control) of dissolved phosphate concentrations (30 year mean, μmol L^{-1}) for the Pacific and Atlantic after 3000 years.

several 100 meters is disturbed by nutrient accumulation in ocean water >1000 m depth. The phosphate accumulation at depth is much stronger in the Atlantic than in the Pacific which is a result of higher export and remineralization of OM, as well as the even weaker ventilation of the deep Atlantic. The meridional crosscut throughout the Pacific and the Atlantic basin after 3000 years reveals stronger surface ocean phosphate depletion in the Southern Hemisphere over the Northern Hemisphere. While in the Pacific the phosphate concentrations accumulate nearly homogeneously over the whole water column >1500 m depth, the accumulation of phosphate shows a North to South gradient in the mid and deep Atlantic. Almost the whole Atlantic north of the equator exhibits a surplus in phosphate of 0.8 μmol L^{-1}. Also after fixing atmospheric CO_2 concentrations in year 1300, the shifting of nutrients from top to bottom goes on. The redistribution of nutrients from the surface to the intermediate and deep ocean is a result of reduced vertical mixing. The depletion in surface nutrient concentrations causes a decrease in primary production and export of OM.

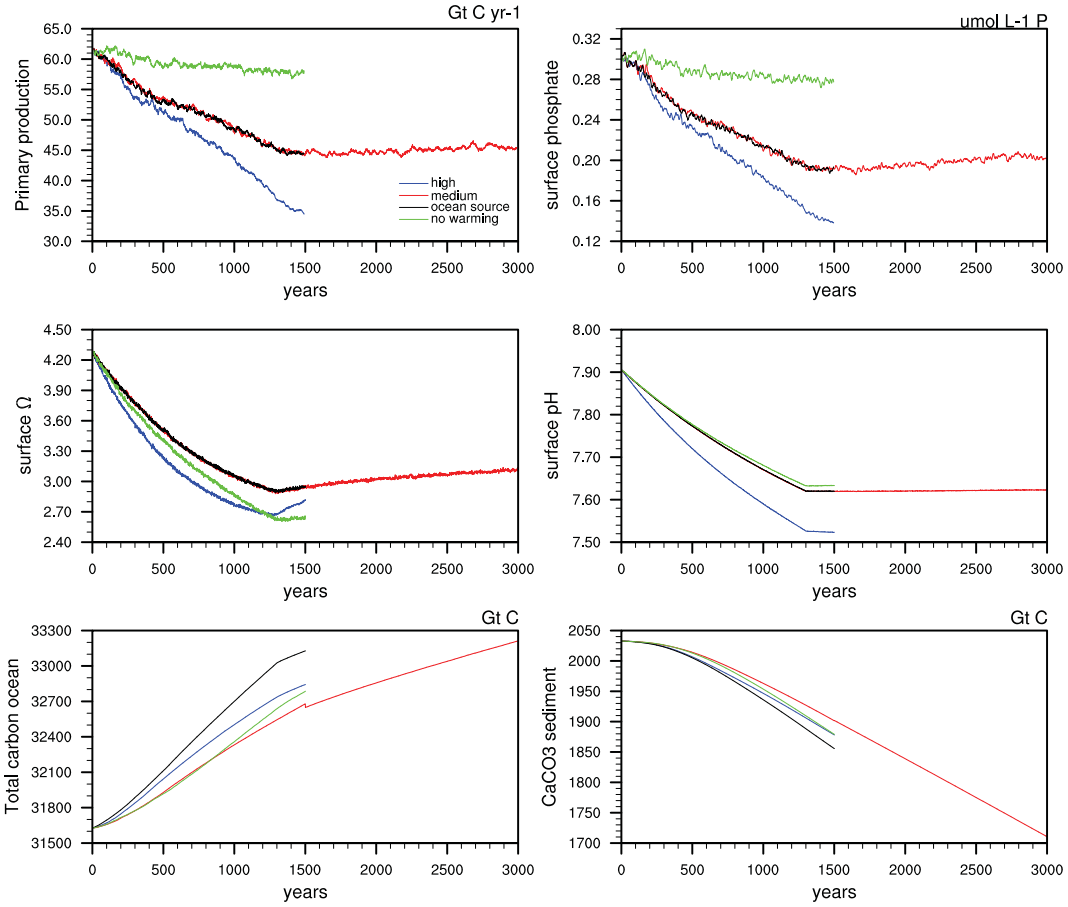

Figure 4.10: Key variables of ocean biogeochemistry for all simulations. Temporal evolution of globally integrated primary production (Gt C yr^{-1}, upper left), surface ocean dissolved phosphate concentration (μmol L^{-1}, upper right), surface ocean Ω (center left), surface ocean pH (center right), total carbon ocean inventory (Gt C, bottom left), and $CaCO_3$ sediment inventory (Gt C, bottom right).

Oxygen

Temperature dependent dissolution of oxygen causes the surface ocean oxygen concentrations to be reduced on a global scale (-11 %, at the end of the *medium* simulation). The oxygen decrease at depth (Figure 4.11) shows a very similar pattern to the phosphate enrichment (Figure 4.9) in the Pacific and the Atlantic. The meridional crosscut through the Pacific shows that the oxygen concentrations decrease everywhere and that the OMZ's expand vertically. The intermediate water masses (1000-2000 m depth) are decreased by up to 100 μmol L^{-1} at the end of the simulation. The deep Pacific reveals weaker oxygen depletion, coinciding with a lower phosphate concentration increase. The deep Pacific is still oxygenated with concentrations of >200 μmol L^{-1} at the end of the simulation. However, equatorial OMZ's show oxygen concentrations as low as 20 μmol. In the Atlantic the oxygen depletion is more intense and spreads into the deep ocean as well. Again, the low oxygen concentrations seem to be an effect of oxygen consumption due to OM remineralization, which is also explaining the Atlantic north to south gradient in oxygen concentrations (Figure 4.11). The oxygen concentrations

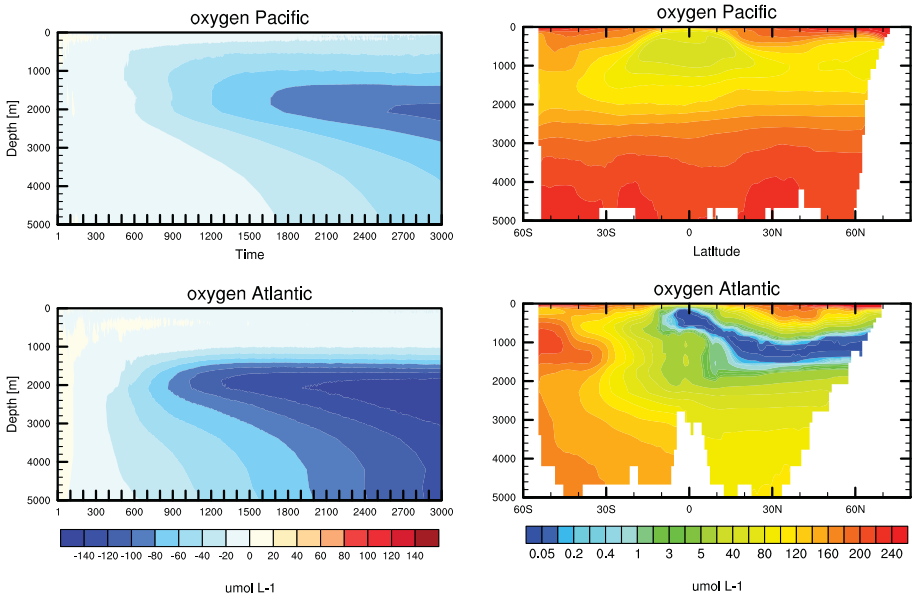

Figure 4.11: Left panel: Temporal evolution of anomaly (*medium*-control) in oxygen concentrations, integrated over the whole Pacific and Atlantic (μmol L^{-1}). Right panel: Zonally averaged oxygen concentrations (30 year mean, μmol L^{-1}) of the *medium* scenario for the Pacific and Atlantic after 3000 years (note the non-linear color bar). Concentrations below 0.05 μmol L^{-1} indicate areas of anaerobic remineralization.

in the deeper part of the Atlantic (>2000 m) are reduced everywhere by >100 μmol L^{-1} at the end of the simulation. Over larger areas of the South Atlantic (in 0-1500 m depth) the oxygen content even increases by up to 70 μmol L^{-1}. Zonally averaged deep ocean oxygen concentrations vary between 80 and 180 μmol L^{-1} and are not in equilibrium yet. The Atlantic OMZ (<20 μmol L^{-1}) is spanning up to 2000 m in the vertical extent and covering the Atlantic from 20° S to 70° N.

The weakening of the Pacific and Indian Ocean MOC acts to initially stagnate the deep ocean globally. However, the Pacific Ocean is still more ventilated than the deep Atlantic. As displayed in Figure 4.12 the oxygen content in seawater decreases every-

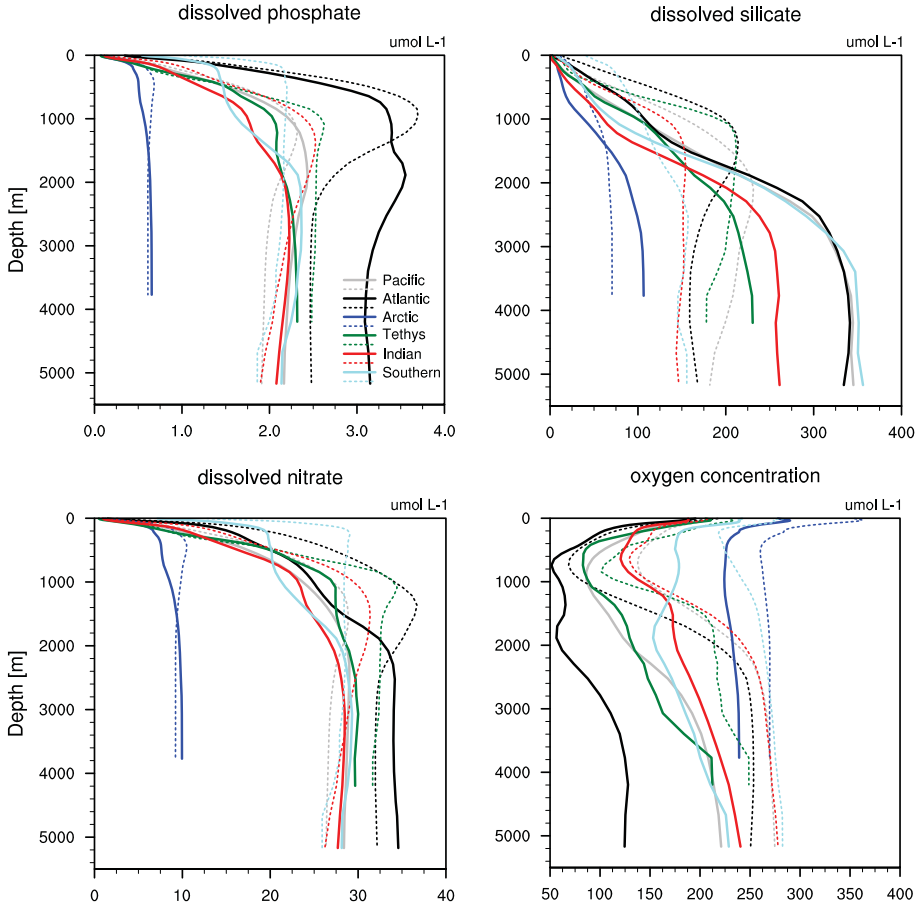

Figure 4.12: Basin-wide averaged phosphate, silicate, nitrate and oxygen concentrations for the *medium* CO_2 simulation (solid line) and the control run (dashed line). All concentrations are given in μmol L^{-1} and averaged over the last 30 years of the respective simulation.

where, but by far the strongest decrease occurs in the Atlantic. Large perturbations in the oceanic oxygen cycle potentially result from changes in oxygen supply (oxygen solubility and ocean circulation) and changes in OM export production. Since an increase in OM export results in higher oxygen consumption due to OM remineralization in intermediate waters. Note that we do not increase the nutrient supply artificially by increasing the weathering fluxes. This would at least decrease the oxygen concentrations further in the coastal regions, as it is predicted for other anoxic events in Earth history (Monteiro et al. 2012). For the prolongation of our simulation we expect the oxygen concentrations to decrease further. The achievement of inhospitable conditions in the oceanic bottom layer due to an oxygen deficiency would probably be reached earlier in the Atlantic than in the Pacific. In any case the deep sea oxygen concentrations are highly dependent on the behavior/progress of deep water formation rates and locations.

Primary and export production

The net primary production (NPP) is affected by the reduced nutrient availability and decreases by globally ∼30 %, at the end of the simulation. After stabilizing the atmospheric CO_2 concentration in the simulation, the NPP stays on a low level (Figure 4.13). The main mechanisms responsible for NPP decrease in the tropics and in the North Atlantic are linked to a reduced supply of nutrients to the euphotic zone in response to enhanced stratification and weaker circulation. Silica is most sensitive to the circulation changes which displays in the silica trapping below 2000 m depth in all ocean basins (Figure 4.12). The same applies in a less pronounced way to the dissolved phosphate, except in the deep Atlantic where the trapping of phosphate is very distinct (Figure 4.12). Integrated over the whole basin, both the Atlantic and the Pacific show a decrease in NPP of ∼25 % (11.64 Gt C yr^{-1} and 21.63 Gt C yr^{-1} NPP in year 3000, respectively). A long-lived decrease in productivity could have led to starvation of benthic organisms, as hypothesized by Winguth et al. (2012). This study also sees a decrease of 20-40 % in export production in their simulations depending on the strength of the prescribed CO_2 emission scenarios.
The export production in 90 m depth reveal an increase in $CaCO_3$/opal and $CaCO_3$/OM export ratios (Figure 4.13). Over the first 400 years the opal, OM and $CaCO_3$ export decrease simultaneously. From thereon the $CaCO_3$ export increases, while the opal and OM export decrease to 90 Tmol Si yr^{-1} and 6.5 Gt C yr^{-1} over 3000 years, respectively. This is a result of the way we parameterize the biological production, since the production/export of $CaCO_3$ depends directly on the opal production/export. Dissolved silica is very sensitive to changes in the ocean vertical mixing, which leads to a relatively rapid decrease in opal export. As a consequences a higher portion of the export flux is allocated to $CaCO_3$ producing organisms. However, there are two periods (year 1-400

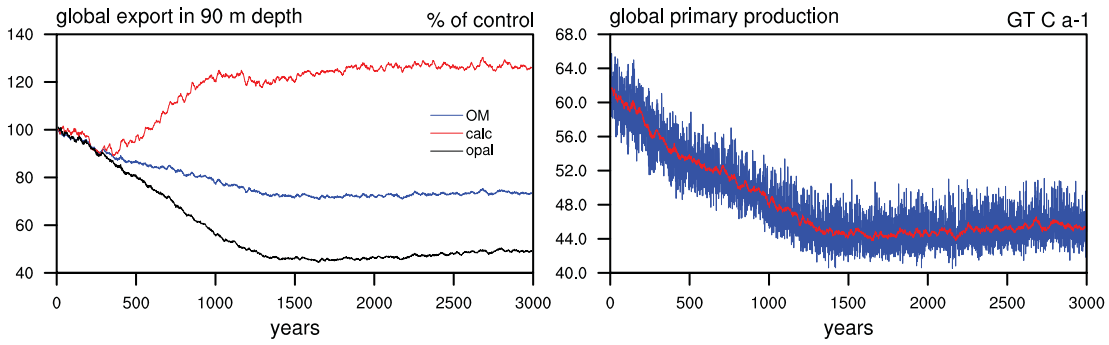

Figure 4.13: Left: global organic matter (OM), $CaCO_3$ (calc) and opal export, over the 3000 years of the *medium* scenario (in % of the control run). Right: global primary production over 3000 years of the *medium* scenario.

and 1200-1300) in which the $CaCO_3$ export decreases, too. This happens due to the implemented Ω-dependency (Section 3.2.4). The effect of the Ω decrease due to atmospheric CO_2 increase exceeds the effect of the silica decrease, due to warming in these periods. The second decline in $CaCO_3$ export ends because of the atmospheric CO_2 stabilization in year 1300. At the end of our simulation, the $CaCO_3$ export amounts to 0.44 Gt C yr^{-1} which equals an increase of 20 %, globally. In absolute numbers the yearly export is still low in comparison to present-day values (0.6 Gt C yr^{-1}; Sarmiento et al. 2002).

4.4.2 Model data comparison for changes in primary production

The proxy record reveals a locally very heterogeneous picture of production changes during the PETM. Observations generally infer that the change from a relatively well-mixed to a stratified and warm ocean at the onset and peak of the PETM (in response to the CO_2 increase) caused oligotrophic surface water conditions in the open-ocean sites in the Atlantic, Indian, and Pacific Ocean (Gibbs et al. 2006b). The decreased open-ocean productivity caused a less efficient biological pumping. Whereas shallower (coastal) regions showed no change or even a production increase during the PETM (Stoll et al. 2007), due to increased nutrient availability (Bralower 2002). However, the production increase did not compulsively set in during the onset of the event, but perhaps was an important mechanism of CO_2 drawdown facing the termination of the PETM (Bains et al. 2000).
The open ocean regions in our simulation show constant to slightly decreasing NPP (Figure 4.14). Whereby the mid to high latitudes show a stronger decrease than the

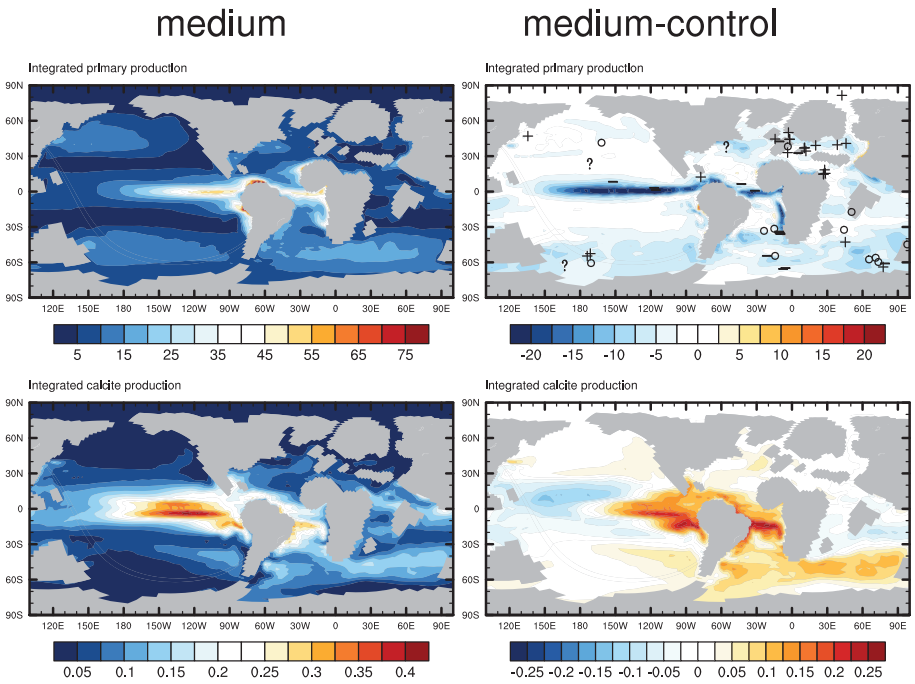

Figure 4.14: Upper panel: primary production integrated over the euphotic zone on the left, and the difference of the *medium* experiment and the control run on the right. The anomaly plot includes observational data points indicating tendencies in production from Winguth et al. (2012): pluses indicate increase, circles indicate no change, minuses indicate decrease, and question marks indicate unclear tendency. Lower panel: same as above for $CaCO_3$ production. All values are given in mol C m^{-2} yr^{-1} and are averaged over the last 30 years of the *medium* scenario.

subtropics, which almost stay unchanged. Unchanging conditions are also suggested for the subtropics by the proxies in the North Pacific, South Atlantic and Indian Ocean. For the Southern Hemisphere high latitudes, the observation sites indicate constant or increasing NPP for the Pacific sector of the Southern Ocean and constant to decreasing NPP for the Atlantic and Indian sector of the Southern Ocean. Our results fit the data in the Atlantic and Indian sector, but not in the Pacific sector. However, it is the same process which drives the depletion of nutrients within the different regions of the Southern Ocean and with it the decrease in NPP in our simulation. Moreover, several studies confirm a weakening of the Southern Ocean deepwater formation during the PETM (see Section 4.3), which would certainly lead to a reduced nutrient availability in the surface ocean.

The weakened equatorial upwelling in our simulation causes a relatively strong de-

crease in NPP along the equator in the central and eastern Pacific and in the Atlantic. This effect is confirmed by several observational studies covering these regions. Also the decrease in NPP along the southwestern coast of Africa is found in the observational data. For the regions in which our model predicts an increase in NPP, such as the northern section of the Pacific eastern boundary current along the South American coast and parts of the northwestern African coast in the Atlantic, are not covered by data.

Several observational sites in the Tethys ocean infer a production increase (Figure 4.14). However, apart from the boundary current along the Asian coast in the Tethys Ocean which shows an NPP increase, the Tethys Ocean shows small to no reduction in NPP in our simulation. Unfortunately this region is again not covered by data. Generally, the weathering induced nutrient supply must have been significantly increased during the PETM to fit the proxies for the Tethys Ocean and other coastal regions. Observations and and other modeling studies (Winguth et al. 2012, and references therein) infer higher weathering rates due an increase in extra-tropical precipitation during the PETM, which could potentially washout more nutrients and transport it to coastal areas. This hypothesis would explain most of the observational data points, suggesting an production increase in the Tethys Ocean. However, our simulation does not consider an increase in terrestrial weathering fluxes due to higher atmospheric CO_2 and intensification of the hydrological cycle. In principle, a coupling of the terrestrial runoff to the weathering input in our model would also increase the nutrient availability in the shelf regions during the PETM simulation and probably reduce the gap between our model results and the analyzed data.

According to the proxy record, the $CaCO_3$ surface productivity did not decrease during the PETM. Sedimentary accumulation rates during the PETM reflect rather dissolution due to ocean acidification in the water column (Stoll et al. 2007). Increased levels of shell fragmentation beside a general decline in $CaCO_3$ content and coarse fraction in sediments from Walvis Ridge (South Atlantic) suggest that the drop in sedimentary $CaCO_3$ wt% during the initial phase of the PETM was caused by dissolution rather than through a decrease in $CaCO_3$ production in the surface ocean (Zeebe and Zachos 2007). Figure 4.14 displays the spatial distribution of the $CaCO_3$ production in the euphotic zone and the difference to the background state. Areas of $CaCO_3$ decrease are the western tropical and subtropical Pacific as well as the Indian Ocean. The $CaCO_3$ production increases nearly over the whole Atlantic, but strongest increase appears in the tropics and the South Atlantic. Moreover, the $CaCO_3$ production increases in the tropical eastern Pacific and in the Indian and Atlantic sector of the Southern Ocean. Within these regions the strongest silicate depletion in the surface ocean occurs. A net ($CaCO_3$) productivity increase in the Atlantic sector of the Southern Ocean is also suggested by Stoll et al. (2007). They analyzed Sr/Ca ratios in sediment core sections covering the PETM to derive variations in productivity of calcareous nannoplankton.

Over the simulation period the averaged $CaCO_3$ export in 90 m depth increases slightly in the Pacific (0.11 mol C m^{-2} yr^{-1}), doubles in the Atlantic (0.12 mol C m^{-2} yr^{-1}) and triples in the Southern Ocean (0.05 mol C m^{-2} yr^{-1}).

4.4.3 Ocean acidification & sediment dissolution

Air-sea CO_2 exchange

The prescribed increase of atmospheric CO_2 forces the ocean to take up CO_2 from the atmosphere. The oceanic carbon uptake is subject to variations, but starts generally decreasing from year ~500 on (Figure 4.15). During the first 500 years of the simulation annual uptake rates of atmospheric CO_2 are strongest, which is primarily an effect of carbon transport to depth via the physical carbon pump. Additionally, increasing stratification of the ocean causes nutrient and DIC trapping in intermediate waters, which restricts the return of CO_2 enriched waters to the surface. This effectively reduces the outgassing of metabolic CO_2, while the biological production and (carbon-) export starts decreasing only slowly with CO_2 increase and warming.

After 500 years the annual CO_2 uptake starts declining. The upper ocean nutrient reservoir is already strongly diminished and carbon transport to depth is decreased because of the continuous decrease in convective overturning. The reduced removal and transport of carbon to deeper layers results in higher surface ocean pCO_2. Moreover, due to higher atmospheric CO_2 concentrations in the Late Paleocene background state the CO_3^{2-} concentrations in the surface ocean are lower than in modern conditions (for further information see Chapter 2). This limits the buffering capacity of the surface ocean in respect to CO_2 is already beforehand. Also the $CaCO_3$ production increase

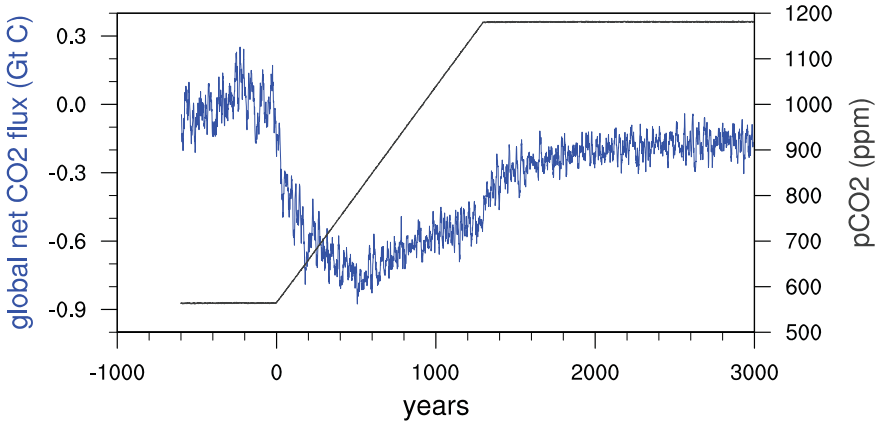

Figure 4.15: Left y-axis (blue graph): globally integrated CO_2 exchange between ocean and atmosphere, covering 600 years of the control run and 3000 years of the *medium* scenario. Negative y-axis values correspond to oceanic uptake, positive values to oceanic outgassing of CO_2 (in Gt C yr^{-1}). Right y-axis (black graph): pCO_2 in the surface ocean due to the *medium* CO_2 emission scenario.

from year 500 on serves as a (weak) positive feedback on the atmospheric CO_2 concentrations. The $CaCO_3$ production consumes TA, this effectively lowers the TA in the surface ocean. However, the increase in $CaCO_3$ export is rather small, compared to present-day $CaCO_3$ export rates. The globally accumulated oceanic CO_2 uptake amounts to 1142 Gt C (847 Gt C) after 3000 years (1500 years).

Oceanic carbon content

The oceanic dissolution of CO_2 alters the ocean carbon chemistry of seawater not only at the surface but also at depth. Principally the CO_2 signal should penetrate into the ocean interior and be compensated by a transient rise in the level of the lysocline and CCD (Zachos et al. 2005) over time. Ultimately this would result in the widespread dissolution of sea-floor $CaCO_3$ to restore pH throughout the ocean. Unlike to Panchuk et al. (2008) and according to Nunes and Norris (2006) our model predicts a substantial weakening of Southern Ocean deep water ventilation in response to PETM warming. As a consequence, the DIC concentrations just increase marginally in the deep Pacific. The strongest increase appears in 1000 to 2000 m depth (Figure 4.16). Below 2000

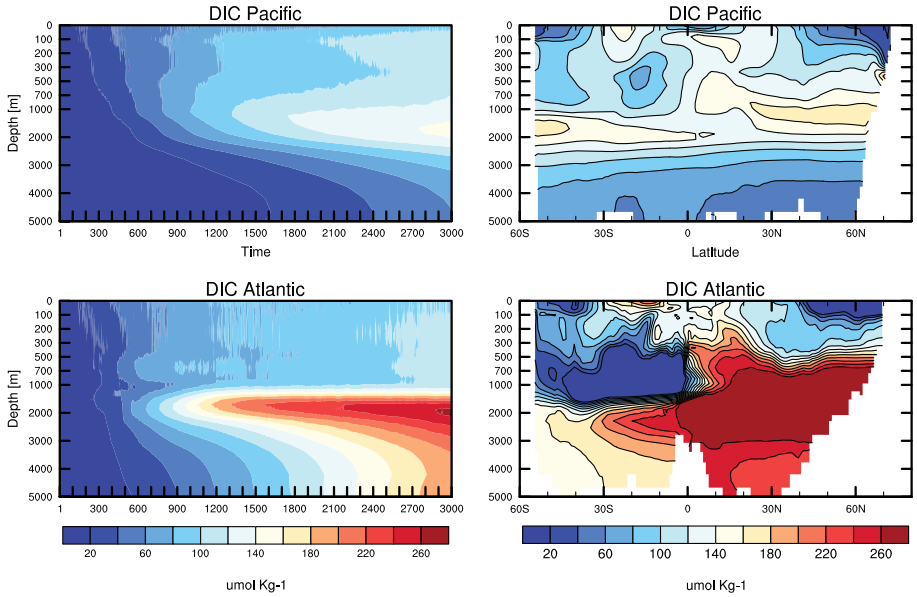

Figure 4.16: Left panel: Temporal evolution of anomaly (*medium-control*) in DIC concentrations, integrated over the whole Pacific and Atlantic. Right panel: Zonally averaged anomaly (30 year mean of *medium-control*) in DIC concentrations for the Pacific and Atlantic. Note the non-linear vertical axes, used to zoom in the upper ocean layers.

m depth the propagation of the atmospheric CO_2 signal is weakened. This matches the Pacific circulation cell, which only covers the uppermost 2000 m (Figure 4.7) due to the stronger stratification of the ocean. In the deep Pacific zonally integrated DIC concentrations are increased by 40 to 80 μmol kg^{-1} after 3000 years.
The Atlantic Ocean in our simulation does not exhibit any deep water formation which could transport CO_2 enriched waters to depth. Instead, the biology seems to have a major influence on DIC vertical transport during the PETM. The biological carbon pump enhances DIC transport to depth and causes a strong decrease in deep Atlantic pH (Figure 4.18). The respiratory CO_2 produced during aerobic remineralization increases the DIC concentrations quite drastically in the much narrower Atlantic (in comparison to present-day). The deep Atlantic zonally integrated DIC concentrations are increased by $\sim$160 μmol kg^{-1} in the southern and $\sim$240 μmol kg^{-1} in the northern part of the basin, at the end of the simulation.

Changes in seawater pH & Ω at the surface

Apart from some regions in the high latitude oceans, $CaCO_3$ saturation state (Ω) decreases everywhere in the surface ocean (Figure 4.17). Generally, the intensity of Ω reduction declines from the equator to the poles. However, the surface ocean stays supersaturated with respect to $CaCO_3$ throughout the whole simulation. This is supported by the greenhouse gas induced warming of the ocean which dampens the Ω decrease. Ridgwell and Schmidt (2010) also produce a strong reduction in the surface ocean saturation state due to a PETM related carbon perturbation. Their simulations does not indicate surface ocean undersaturation in respect to $CaCO_3$, neither. Also proxy data approves that the surface water saturation state across the PETM was not detrimental to the survival of most calcareous nannoplankton taxa (Gibbs et al. 2006a).
The pH decreases almost linearly with the atmospheric CO_2 increase (4.10). It adapts rather quickly to the fixation of the atmospheric CO_2 concentrations in year 1300 and balances on a global scale at a value of 7.62. Note that the increase in $CaCO_3$ production amplifies the decrease of surface pH due to the consumption and export of CO_3^{2-}, but this is only accountable for $<$0.02.
Figure 4.17 displays that the pH decreases everywhere. As a result of temperature dependent CO_2 uptake, pH decreases in the high latitudes more than in the low latitudes. A decrease in pH with simultaneous decrease in surface ocean Ω, both indicators for ocean acidification, are expected to have happened during the PETM (Hoenisch et al. 2012). The magnitude of the pH and Ω decrease depend primarily on the rate of the CO_2 release, however the strength and duration of the carbon injection for the PETM is still under debate (Pagani et al. 2006a). Hoenisch et al. (2012) consider a 0.25 to 0.45 unit decline in surface seawater pH possible, but question if model-inferred peak rates of $\leq$1 Gt C yr^{-1} for the PETM are sufficient to produce this signal. Recently, for

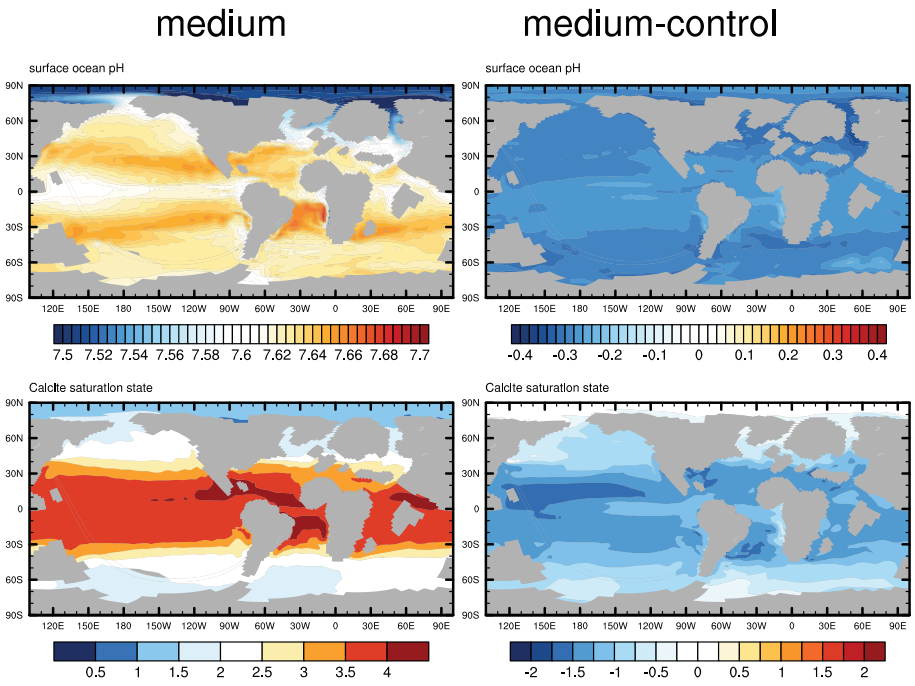

Figure 4.17: Left panel: surface ocean pH and Ω, averaged over the last 30 years of the *medium* CO_2 simulation. Right panel: difference of the *medium* experiment and the control run for both variables.

the first time a pH decrease could be confirmed by geochemical proxies for the PETM (Penman et al. 2014). From a sediment core located in the North Pacific Penman et al. (2014) derived an initial surface pH drop of 0.3 for the PETM, which is quite close to the results we obtain from our simulation (decrease of 0.28). For instance, Zeebe et al. (2009) simulate a lower pH decrease for the onset of the PETM but also prescribe lower rates of CO_2 increase (0.6 Gt C yr^{-1}) than we do. Zeebe et al. (2009) argue that a higher CO_2 increase rate could be inconsistent with CCD shoaling. In our simulation changes in the ocean circulation could act as a compensatory effect, since less CO_2 is transported to depth in the warming ocean.

Changes in seawater pH & Ω in the water column

Figure 4.18 shows that corresponding to the DIC increase and pH decrease, the CO_3^{2-} concentration in the Atlantic is decreased by 30 μmol kg^{-1}. Whereas in the deep Pacific the CO_3^{2-} concentration drops only by 20 μmol kg^{-1}. Proxy data indicates that the deep CO_3^{2-} content in the Pacific was about 1.5 times higher than in the South Atlantic Zeebe and Zachos (2007). At the end of our simulation the deep CO_3^{2-} concentration is

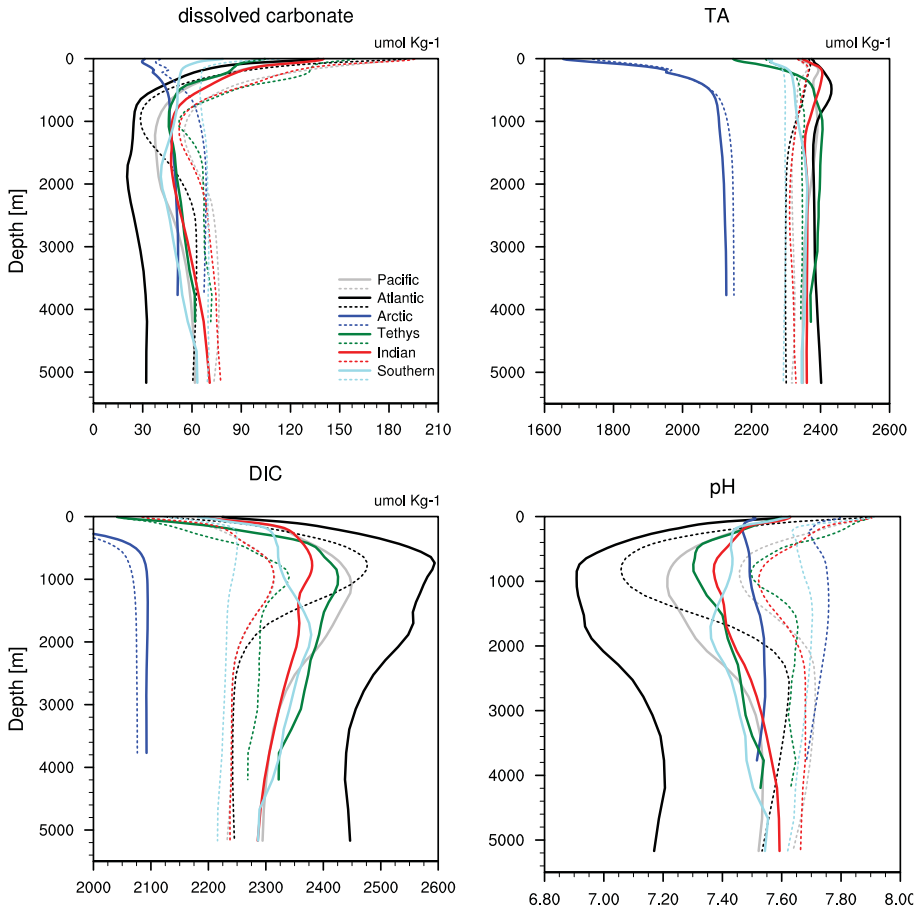

Figure 4.18: Basin-wide averaged carbonate, TA, DIC concentrations and pH for the *medium* simulation (solid line) and the control run (dashed line). All concentrations are given in μmol kg^{-1} and are averaged over the last 30 years of the simulation.

twice as high in the Pacific than in the Atlantic (Figure 4.18). However, if we compare the deep Pacific to the South Atlantic only, the factor amounts to 1.5, which reproduces the gradient indicated by (Zeebe et al. 2009) in the water column.
The reversed circulation (compared to modern conditions) of the pre-PETM background state, including deepwater formation in the Southern Ocean but no North Atlantic deep water source, produces a lower Ω in the Atlantic than in the Pacific (Figure 4.19, for further information see Chapter 2). This makes the $CaCO_3$ in the Atlantic water column and sediment more vulnerable to dissolution beforehand.
With increasing atmospheric CO_2 concentrations, Ω decreases significantly in our experiment in comparison to the pre-PETM state and continues to decrease after the

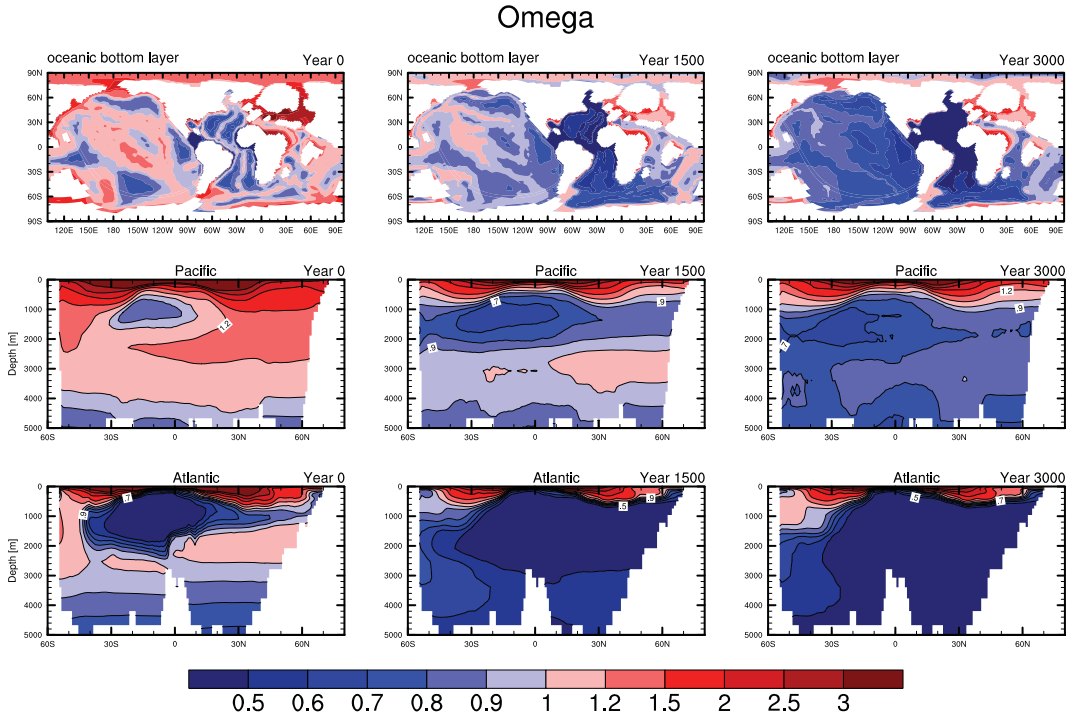

Figure 4.19: $CaCO_3$ saturation state (Ω) in the oceanic bottom layer (upper row), the zonally averaged Pacific (middle row) and the zonally averaged Atlantic (bottom row) for year 0 (left panel), year 1500 (middle panel) and year 3000 (right panel) in the *medium* simulation. All plots show 30 year averages.

atmospheric CO_2 is stabilized (Figure 4.19). The drop in Ω leads to dissolution in the water column and the sediment in all ocean basins. However, the Atlantic is more affected by the carbon perturbation than the Pacific. The faster acidification of the Atlantic in our simulation happens for two reasons: (1) the reversed CO_3^{2-} basin gradient compared to today, i.e., with higher CO_3^{2-} concentrations in the Pacific than in the Atlantic, allows a faster undersaturation of the Atlantic under the same carbon input like in the Pacific. (2) the aerobic OM remineralization and associated CO_2 release is much stronger in the Atlantic. Moreover, the size of the Atlantic in comparison to the Pacific allows a quicker response to the mentioned reasons. While the Pacific contains about 60 % of the global ocean volume, only 15 % fill the narrower Atlantic basin. Still, the physical carbon transport into the deep ocean is higher in the Pacific, due to stronger convectional mixing in the Pacific Ocean basin.
The subsurface ocean at depths below 400 m in the Pacific and below 100 m in the Atlantic is already undersaturated in year 1500 of our simulation (Figure 4.19). Due

to undersaturation in the water column, the sedimentation of $CaCO_3$ approaches zero in the year 900 in the Pacific. The $CaCO_3$ sedimentation in the deep Atlantic is already low in the pre-PETM state. During the experiment the basin averaged flux even increases because of $CaCO_3$ sedimentation in shallow parts of the Atlantic (<1000 m depth) along the coast of South America and Africa. The dissolution of deep sea $CaCO_3$ sediments drives the TA increase in the Atlantic and Indian Ocean at depth (Figure 4.18). After 3000 years the Atlantic and the Pacific are mostly undersaturated with respect to $CaCO_3$ which would represent inhospitable conditions for benthic calcifiers. The massive undersaturation is in line with the proxy record since the extinction associated with the PETM was particularly strong amongst deep-sea calcifiers, whereas agglutinating, non-calcifying deep-sea species show significantly lower levels of extinction (Ridgwell and Schmidt 2010).

Sediment

The dissolution of $CaCO_3$ bearing sediments is triggered by the increase in acidification of the oceanic bottom layer and the decrease in $CaCO_3$ rain from the surface. Global dissolution of $CaCO_3$ in the sediment amounts to 322Gt C after 3000 years. This equals to a decrease of 15.8 % of the pre-PETM inventory. The fluxes of TA at the ocean-sediment boundary, which we use as an indicator for $CaCO_3$ sediment dissolution, increase in every basin except in the Arctic Ocean (Figure 4.20).
The Atlantic Ocean is characterized by a net deposition of $CaCO_3$ in the pre-PETM state. The deposition takes place in shallow areas along the northwestern coast of Africa, the northern and northeastern coast of South America, as well as in the shelf areas around the southern tip of North America. This $CaCO_3$ deposition does not decrease over the duration of the experiment. Although, the net flux of TA from the sediment, due to sedimentary $CaCO_3$ dissolution, just becomes positive after 1000 years in the Atlantic, dissolution of deep sea $CaCO_3$ starts already in year 150. The relative TA concentration increase is much higher in the Atlantic oceanic bottom layer compared to the other basins (Figure 4.20).
The Pacific Ocean $CaCO_3$ sediments respond after around 500 years to the carbon perturbation and start to decline. The Pacific exhibits the highest absolute TA flux out of the sediment, because the basin comprises also 50 % of the global ocean floor (for comparison Atlantic: 16 %).
Similar to the Atlantic and the Pacific also the Indian Ocean shows a decline in $CaCO_3$ sediments with time. The Indian Ocean TA sediment to ocean flux increases stronger over the first half of the experiment, while to the end of the experiment the flux is nearly balanced. The TA in the ocean bottom layer in the Indian Ocean is in average about $\sim$50 μmol kg^{-1} increased at the end of the simulation (Figure 4.20). Lateral transport of TA rich water keeps the TA concentrations relatively low in comparison

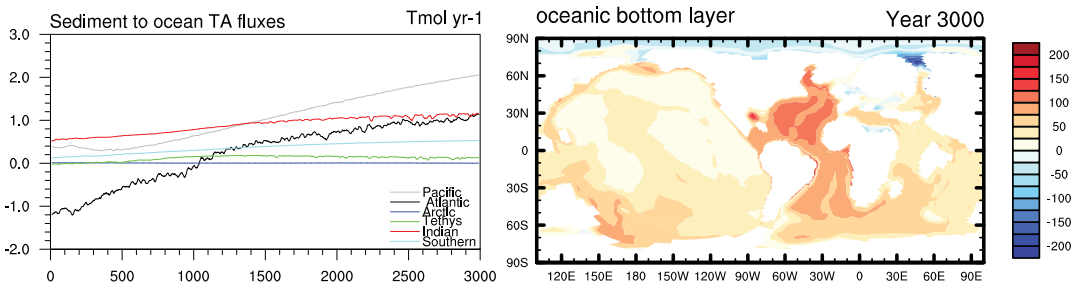

Figure 4.20: Left: basin specific absolute sediment to ocean TA flux (Terra mol yr^{-1}, 20-year running mean) in the *medium* CO_2 scenario. Right: TA anomaly (μmol kg^{-1}) in the oceanic bottom layer after 3000 years of the *medium* simulation.

to the Atlantic and influences the TA in the shallower Tethys and the Southern Ocean. While the $CaCO_3$ dissolution in the Tethys Ocean increases over the first half of the experiment, it decreases in the second half again. This also mirrors the gross deposition of $CaCO_3$ from the surface. The Southern Ocean is characterized by continuous dissolution increase since the remaining deepwater production transports carbon to the deep ocean. Though, the deposition of $CaCO_3$ even increases with time in the Southern Ocean shelf areas.

The dissolution driven TA increase in the oceanic bottom layer matches well the change in $CaCO_3$ wt% of the solid sediment (Figure 4.21). After 3000 years all basins still bear $CaCO_3$ sediments. Maximum $CaCO_3$ fractions amount to ~80 wt%. They are located in several spots in the Indian Ocean and in coastal regions in the western Pacific. Generally the Indian Ocean and the western Pacific show the strongest decrease in $CaCO_3$ wt% in our simulation (Figure 4.21). The reason for this is mainly the large/high amount of $CaCO_3$ which was stored in these locations in the pre-PETM setting. However, due to the large volume of the Pacific and the intense exchange of water masses between the Indian and its surrounding oceans, the TA in the bottom layer is not increased accordingly in the two basins.

4.4.4 Model data comparison for changes in $CaCO_3$ sediment content

The $CaCO_3$ sediment content resulting from our simulation is evaluated against the available sediment record (Panchuk et al. 2008, and references therein). In comparison to sediment core data the western Pacific dissolution should be more moderate in our simulation, while the Central Pacific which shows almost no dissolution matches the data well (Figure 4.21). The sedimentary $CaCO_3$ in the eastern Pacific dissolved almost completely according to the proxy record. Yet, our results do not show any dissolution

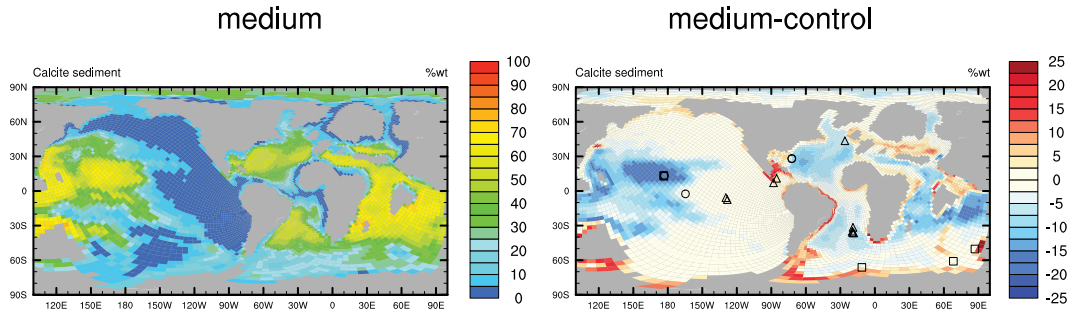

Figure 4.21: $CaCO_3$ sediment content (in wt%) for the *medium* CO_2 scenario after 3000 years (left column) and difference between *medium*-control run (right column). Calculations are based on 30 year averages. The anomaly plot includes observational data points (Panchuk et al. 2008) indicating tendencies in $CaCO_3$ wt% decrease: circles indicate low dissolution (<10 %), squares indicate medium dissolution(10-50 %) and triangles indicate high dissolution(>50 %). See Panchuk et al. (2008) for more details.

because the eastern Pacific has no $CaCO_3$ deposition in our simulation of the pre-PETM state. As described in Chapter 3, this mismatch is mainly a result of depth divergences between sediment cores and the model bathymetry.
In the Atlantic the $CaCO_3$ sediments decline more homogeneously over the whole basin. The model results mainly correspond to the sediment core data. In the shallow parts of the Southern Ocean $CaCO_3$ even increase over the 3000 years of the simulation, while deeper sections drop slightly in $CaCO_3$ wt%. Proxy data (sediment cores are located on the outskirts of the shelf) indicate moderate dissolution of $CaCO_3$ for offshore regions of the Southern Ocean during the PETM.

The Pacific and Atlantic $CaCO_3$ dissolution pattern resulting from our simulation is principally conform with moderate CCD shoaling in the Pacific and strong CCD shoaling in the Atlantic, as it is suggested by proxy data (Zachos et al. 2005; Zeebe et al. 2009). While Zeebe et al. (2009) are only able to reproduce the sediment dissolution ratio between Atlantic and Pacific by prescribing a steady North Pacific deepwater formation during the event (which makes the Atlantic deep waters more corrosive) and by partial carbon injection directly into the Atlantic, this seems not to be essential in our simulation. However, the dissolution ratio between the Atlantic and Pacific would have to be reevaluated over longer timescales in our simulation, since Zeebe et al. (2009) apply the fixed deepwater formation and the oceanic carbon source to simulate the whole event and not only the first 3000 years.

4.5 Sensitivity of ocean biogeochemistry to different sources & rates of carbon

To test the plausibility of different scenarios for the PETM we run two additional simulations and check their compatibility with the $CaCO_3$ dissolution record and with producing inhospitable conditions for the benthos (benthic extinction event). We study the sensitivity of our model towards a stronger atmospheric CO_2 increase (*high* scenario) and towards a deep ocean carbon source (*ocean source* scenario, see Section 4.1).

4.5.1 Atmosphere and ocean physics

High CO_2 scenario

In the *high* simulation the climate change related processes are intensified in comparison to the *medium* simulation. The SST increases by ∼8 °C over the 1300 years of CO_2 increase and warm by additional 1.5 °C in the 200 years of fixed CO_2 concentrations (at 1483 ppm). Although CO_2 is fixed after 1300 years, warming proceeds in the same rate as during the CO_2 increase. The stronger warming results in higher freshwater input into the deep water formation areas. Subsequently the overturning weakens further. The maximum MOC below 1000 m depth, in comparison to the *medium* simulation is ∼3 Sv lower in the Pacific and ∼1 Sv lower in the Atlantic. The deepwater warms only slightly more than in the *medium* simulation. In global average it is about 0.2 °C warmer (at 2000 m depth) in year 1500.

Ocean source scenario

The additional deep Atlantic carbon emission in the *ocean source* simulation has no effect on the atmospheric and oceanic physical state under this model setup. Like in the *medium* simulation, the MOC weakens with increasing CO_2 and warming and the circulation gets more stagnant. The surface warming is identical on the global scale, as well as in the spatial extent. By the end of the simulation after 1500 years, the global warming amounts to ∼5 °C (see Section 4.3).

4.5.2 Implications for the carbon cycle

High CO_2 scenario

The global ocean net uptake of atmospheric CO_2 amounts to 985 Gt C over 1500 simulation years, which equals an increase of 16 % in comparison to the *medium* scenario. This higher uptake occurs mainly over the first 600 years. In the following period the decrease in CO_2 uptake is higher than in the *medium* scenario. To the end of the

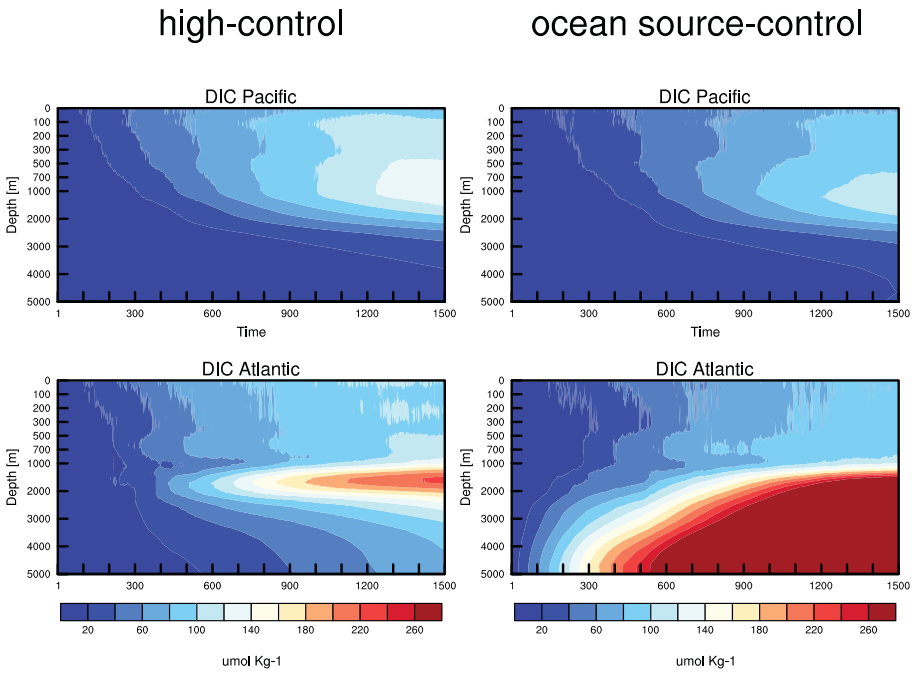

Figure 4.22: Temporal evolution of anomaly in DIC concentrations, integrated over the whole Pacific and Atlantic, for the *medium* (left panel) and *ocean source* (right panel) simulation. Note the non-linear vertical axes, used to zoom in the upper ocean layers.

simulation (year 1100-1500) the annual uptake is nearly identical between the two experiments.

Due to the increased uptake in the *high* scenario the DIC inventory is increased by 20 %. The DIC increase is distributed uniformly over all basins. However, the increase is restricted to the uppermost 2000 m of the water column. The DIC concentrations below 2000 m depth are not higher than in the *medium* scenario (Figure 4.22). At the end of the simulation (year 1500) the surface pH amounts to 7.53, which equals a decrease of 0.37 from Late Paleocene conditions, globally. Surface Ω decreases more rapidly than in the *medium* scenario, but the surface ocean does not get undersaturated with respect to $CaCO_3$ either.

The nutrient availability is very limited, since the surface oceans are even more depleted in nutrients than in the *medium* scenario. The stratified ocean further reduces the supply of nutrients to the surface. Consequently, the primary production decreases by 44 % in respect to the background state (-30 % in *medium* scenario, Figure 4.10), which results in an annual production of 35 Gt C in year 1500. The decrease in nutrient concentrations and primary production goes on after fixing atmospheric CO_2 concen-

trations from year 1300 on.
The $CaCO_3$ production and export varies over time but stays almost on the same level as at the beginning of the simulation. A net increase in $CaCO_3$ production like in the *medium* scenario is prevented by the Ω-dependency in the $CaCO_3$ production term. Higher atmospheric CO_2 concentrations lead to a faster Ω decrease in the surface ocean and with this the $CaCO_3$ production is weakened. The OM export decreases by 45 % over the simulated period, according to the reduction in primary production. The annual OM export amounts to 5 Gt C at the end of the simulation.
In the intermediate and deep ocean the same effects emerge as in the *medium* scenario. However, accordingly to the stronger warming and stratification of the ocean these effects are intensified. The increase in DIC concentrations in the intermediate waters due to remineralization of OM is enhanced. This leads to a faster acidification of intermediate waters, which is again in the Atlantic stronger than in the Pacific. The deep sea carbonate chemistry does not alter extensively between the *high* and *medium* scenario over the simulated period.

Ocean source scenario

Although we prescribe the same atmospheric CO_2 increase scenario in the *ocean source* and *medium* scenario, the oceanic CO_2 uptake in the *ocean source* experiment amounts to only 781 Gt C after 1500 years. This is a decrease of 8 % compared to the *medium* scenario. The annual oceanic CO_2 uptake increases over the first 400 years and then decreases continuously until the end of the simulation. The pCO_2 of the surface ocean is additionally to the atmospheric CO_2 increase influenced by the DIC signal from the Atlantic ocean floor (>1000 m depth). The reduced uptake is mainly owed to increased CO_2 outgassing in the Atlantic and Southern Ocean, which seems convincible since we prescribe the deep ocean carbon source (by increasing DIC concentrations) in the Atlantic. However, also in the Pacific, the CO_2 uptake is slightly reduced. Note that the decreased uptake does not influence the atmospheric CO_2 concentration, since the carbon cycle is not calculated interactively.
The DIC inventory is increased by 50 % compared to *medium* simulation. The deep Atlantic shows basin wide averaged DIC concentrations of up to 560 μmol kg^{-1}. The DIC signal does not spread very much horizontally. Within the simulation period there appears almost no DIC increase in the other basins (Figure 4.22). The surface ocean shows no differences in Ω and pH between the *ocean source* and the *medium* scenario. The same is true for biology related processes in the intermediate waters of the global ocean. Since the *ocean source* and *medium* scenario produce the same magnitude of warming, also the nutrient trapping in intermediate waters is identical. The additional carbon source does not influence this effect. However, if we would couple the artificial DIC concentration increase to the oxygen cycle in order to imitate the dissolution and

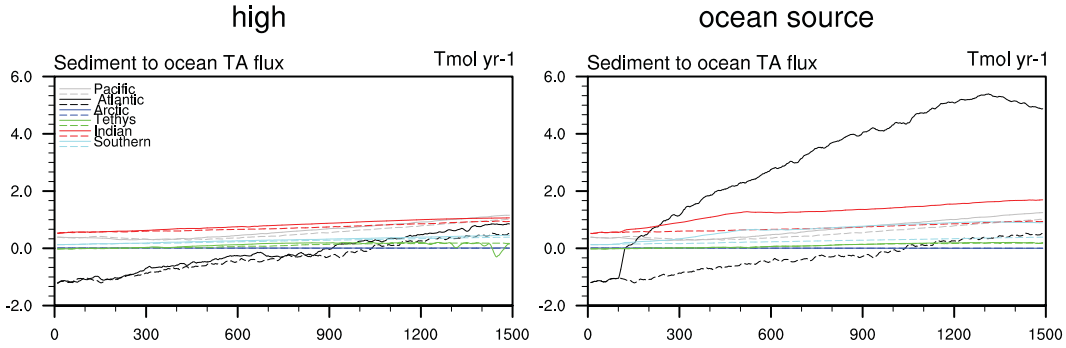

Figure 4.23: Sediment to ocean absolute TA flux (Terra mol yr^{-1}, 20yr running mean) for the *high* (left) and *ocean source* (right) CO_2 scenario, averaged over the specific basins. Both plots include TA fluxes from the *medium* scenario (dashed lines) for comparison.

oxygenation of methane hydrate (as a possible carbon source), it would considerably expand suboxic and hypoxic waters in the Atlantic.
While the *ocean source* simulation drives the deep Atlantic into extreme undersaturation in respect to $CaCO_3$, the Ω of the deep Pacific looks almost identical to the one in the *medium* experiment.

4.5.3 Effects on $CaCO_3$ sediments

High CO_2 scenario

The $CaCO_3$ dissolution in the *high* scenario (155 Gt C) exceeds the one in the *medium* scenario by 25 Gt C, which is equivalent to an increase of 19 %. The sediment to ocean TA fluxes indicate that the $CaCO_3$ dissolution increases homogeneously in all basins (Figure 4.23). The additional $CaCO_3$ dissolution in comparison to the *medium* scenario takes primarily place in the shallow parts of the ocean basins in the Atlantic, Tethys and Indian Ocean, whereas, deep sea $CaCO_3$ sediments are not affected by more intense dissolution. The dissolution pattern is in agreement with the DIC increase in the uppermost 2000 m of the water column.

Ocean source scenario

In the *ocean source* scenario the net $CaCO_3$ dissolution amounts to 177 Gt C, which is 47 Gt C stronger than in the *medium* scenario (36 % increase). While the $CaCO_3$ flux into the sediment (between *ocean source* and *medium* simulation) is identical over the

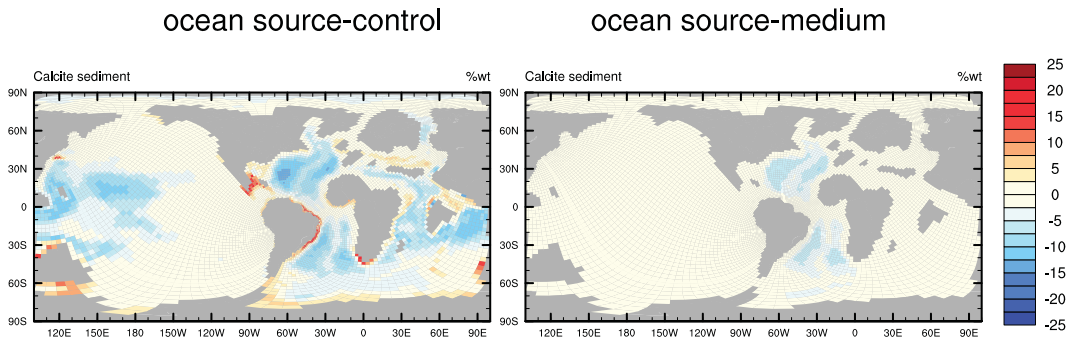

Figure 4.24: Difference in $CaCO_3$ sediment content (in wt%) for *ocean source-control* simulation (left column) and for *ocean source-medium* simulation (right column). Calculations are based on 30 year averages after 1500 simulation years.

whole experiment in all basins, the net changes are entirely due to dissolution processes. The additional $CaCO_3$ dissolution takes place in the Atlantic, but also the dissolution in the Indian Ocean is increased, as indicated by the TA flux into the oceanic bottom layer (Figure 4.23). In the Atlantic the TA flux rises from net sedimentary uptake of 1 Tmol yr^{-1} to a release of up to 5 Tmol yr^{-1}, but starts decreasing again after the prescribed carbon release is stopped in year 1300. The $CaCO_3$ dissolution pattern in Figure 4.24 shows that the *ocean source* simulation meets the criteria of strongest $CaCO_3$ dissolution in the Atlantic compared to the other basins. The difference in sedimentary carbonate content to the *medium* simulation is restricted to < 2.5 wt% outside of the Atlantic Ocean. In the Atlantic the $CaCO_3$ dissolution is amplified and resulting in an additional decrease of up to 5-10 wt% over widest areas of the basin.

4.6 Isolating the warming effect on ocean biogeochemistry during the PETM

We run an additional simulation (*no warming*, see Section 4.1) in which we prescribe the same atmospheric CO_2 increase as in the *medium* scenario, but the CO_2 is treated as an nonradiatively active gas. To assign climate change and climate concentration effects on the ocean biogeochemistry during the PETM we compare the (radiatively) "uncoupled" *no warming* simulation to the (radiatively and biogeochemically) "coupled" *medium* simulation. By analyzing the differences between the two simulations we can isolate how climate change affects the carbon cycle. We study the sensitivity of the ocean biogeochemistry towards warming and concomitant stratification of the ocean and analyze the resulting effects on $CaCO_3$ dissolution and deoxygenation of the deep sea.

4.6.1 Climate change induced reduction in oceanic carbon uptake

The ocean in the *no warming* simulation takes up 1020 Gt C over 1500 years, which equals an increase of 20 % in comparison to the *medium* scenario (Figure 4.25). The difference in uptake between the two simulations is attributed to ocean warming. This climate change induced effect acts as a positive feedback on atmospheric CO_2 concentrations. The carbon inventory in the ocean is increasing less/more slowly due to CO_2 induced warming. The comparison of the *medium* to the *no warming* simulation shows that the CO_2 uptake is partly decreased by SST increase which reduces CO_2 solubility in the surface ocean. However, the main attribution to the reduced CO_2 uptake is the suppressed carbon transport to depth due to the weakened thermohaline circulation and mixing.

The CO_2 uptake in the *no warming* simulation increases mainly in the southern Pacific Ocean where the main deepwater is formed. The Pacific Ocean absorbs 1302 Gt C (930 in *medium* scenario). However, also (net) outgassing increases in some regions, e.g., the Southern Ocean releases 249 Gt C over the whole duration of the simulation (9 Gt C in *medium* scenario). The increased CO_2 release in the Southern Ocean in the *no warming* simulation implies that CO_2 drawdown is triggered due to temperature increase in this region in the *medium* simulation. Pacific and Indian Ocean convection cells reduce not only in their vertical extent but also shift horizontally, due to warming. The anomaly in time evolution of the atmosphere-ocean CO_2 exchange between the *no warming* and the *medium* simulation is close to 0 over the first 400 years, before it becomes negative over a period of 150 years (Figure 4.25). During this period the CO_2 uptake in the *medium* simulation exceeds the one in the *no warming* simulation. This seems to be some transition phase in which CO_2 outgassing is already reduced in the Southern Ocean, but deepwater formation and concomitant CO_2 uptake are not

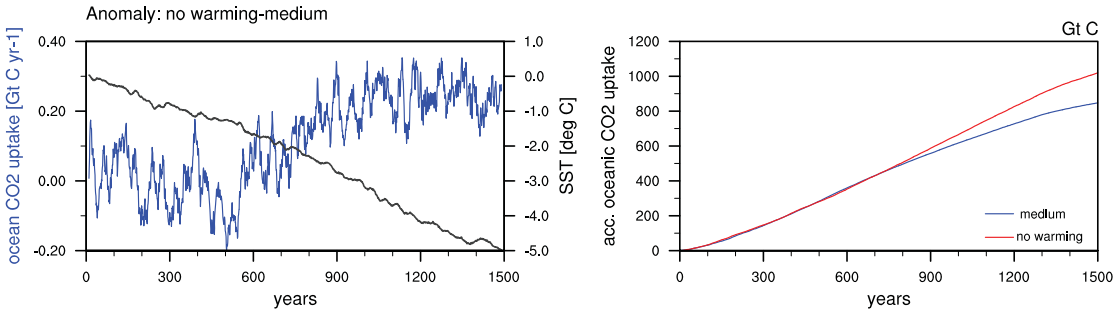

Figure 4.25: Left: Anomaly in ocean CO_2 uptake (Gt C yr^{-1}, blue line) and SST (°C, black line) between the *no warming* and *medium* simulation. Right: Cumulative atmosphere-ocean CO_2 flux (Gt C).

decreasing in the Pacific, yet. Another reason could be the biological carbon pump which reduces the oceanic CO_2 release in the *medium* simulation since the remineralized carbon is just partly brought back to the surface due to the stratification of the ocean. The CO_2 uptake starts to diverge between the two simulations in year 500, due to the reduced CO_2 solubility and decreased transport of carbon from the surface to depth. The feedback becomes stronger with rising temperatures. For the last 600 years the annual uptake is about 0.25 Gt C higher in the *no warming* simulation, which is perceived in the increasing divergence from the *medium* simulation in the accumulated CO_2 uptake (Figure 4.25). Overall, the occurred climate change must have reduced the efficiency of the ocean to absorb atmospheric CO_2 during the PETM. Assuming a carbon perturbation of 10.000 years this effect likely played a role in maintaining elevated atmospheric CO_2 concentrations and temperatures during the event. However, the strength of the carbon cycle feedback is determined on the weakening of the circulation and vertical mixing.

Indirect warming

Although the model's radiation code does not respond to the prescribed atmospheric CO_2 increase, some "indirect" warming is produced by the biogeochemistry components. This temperature increase primarily originates from CO_2 driven biogeophysical processes, such as changes in the fractional coverage of vegetation and reduction in transpiration due to atmospheric CO_2 increase. Furthermore CO_2 fertilization effects can lead to surface albedo reduction due to increasing leaf area, which occurs especially in the high latitudes (Arora et al. 2013). The warming of surface temperatures in non-radiatively coupled simulations is known and also appears in other models (Schwinger

et al. 2014, and references therein). In our simulation the warming amounts to a SST increase of 0.57 ℃. Since the surface warming is more intense in the high latitudes, the deepwater formation areas are more affected by it. Consequently, also in the *no warming* simulation the meridional overturning decreases by ∼2 Sv in the Southern Hemisphere over the simulated period (Figure 4.4).

4.6.2 Implications for the marine biogeochemical cycles

The *no warming* simulation shows just minor modifications in nutrients and production in comparison to the Late Paleocene background state. The surface ocean is characterized by only a weak depletion of nutrients and silicate. Also in the *no warming* simulation some "indirect" warming leads to a reduction in meridional overturning, which influences again the nutrient supply of the surface ocean. Since the opal production/export does only slightly decrease (-8 %), the $CaCO_3$ production does not increase like in the *medium* simulation. Instead the production and export of $CaCO_3$ decreases over time by about 20 %. Overall primary production decreases by 4 Gt C yr^{-1} (-6 %); So does the OM export (decrease by 6 %).

At depth the phosphate concentrations in the Pacific show almost no difference to the control run, whereas, in the Atlantic increased phosphate concentrations in 500-1500 m depth occur in the tropics and the Northern Hemisphere mid latitudes. However, the increase is much smaller than in the *medium* simulation. The same applies for the oxygen concentrations. Only the Atlantic shows a vertical expansion of OMZ's in the Northern Hemisphere. At the same time the OMZ's in the Southern Hemisphere shrink. Since the oxygen concentrations between 500 and 2000 m are increased in comparison to the background state. Consequently, the deoxygenation during the PETM is to large parts an effect of the circulation response to the carbon perturbation.

As a consequence of the decline in $CaCO_3$ export, the surface TA increases in the *no warming* scenario. Whereas, the decrease in Ω is stronger in the *no warming* scenario than in the *medium* scenario due to higher uptake of atmospheric CO_2. Furthermore the decrease in Ω due to the pCO_2 increase is not counteracted by ocean warming (through decrease of saturation concentration) like in the *medium* simulation, leading to surface ocean undersaturation with respect to $CaCO_3$ ($\Omega < 1$) in the Arctic Ocean and very low Ω of 1.3 over wider areas in the North Atlantic and the Southern Ocean. Lower Ω results in an effectively higher carbonate buffering of CO_2, which reveals in lower surface CO_3^{2-} concentrations at contemporaneous lower decrease in pH (-0.27), in comparison to the *medium* simulation. DIC concentrations in the surface ocean are higher than in the *medium* simulation (Figure 4.26), because of higher solubility of CO_2 in colder water and increased carbonate buffer. Surface DIC concentrations increase from 2090 to 2250 μmol kg^{-1} over the simulation period in the *no warming* simulation. The DIC inventory in the oceanic water column is 13 % increased compared to *medium*

scenario. The DIC concentrations increase primarily within the upper 1000 m and slightly in waters below 3000 m, globally. While in the upper 1000 m DIC concentrations are increased in both the Atlantic and the Pacific, its only the Pacific which exhibits increased DIC concentrations in waters below 3000 m compared to the *medium* simulation (Figure 4.26). In the Pacific CO_2 enriched water is faster transported to depth, since the vertical mixing is just slightly reduced, whereas the Atlantic is depleted in DIC in comparison to the *medium* scenario in the deep sea. The DIC concentrations do not show maximum concentrations in intermediate waters (1000-2500 m depth), since the products of OM remineralization (including DIC) are brought to the surface again by upwelling of water masses. As a consequence the downward transport of carbon (DIC) from the surface to depth in the Atlantic is faster in the *medium* than in the *no warming* simulation. The comparison of the two runs shows that while in the Pacific the strength of the circulation and mixing has a positive effect on the undersaturation of the deep ocean, it is the other way round in the Atlantic. The stagnation of the ocean mixing helps to establish corrosive deep sea conditions in the Atlantic via the trapping of OM and its remineralization in intermediate waters.

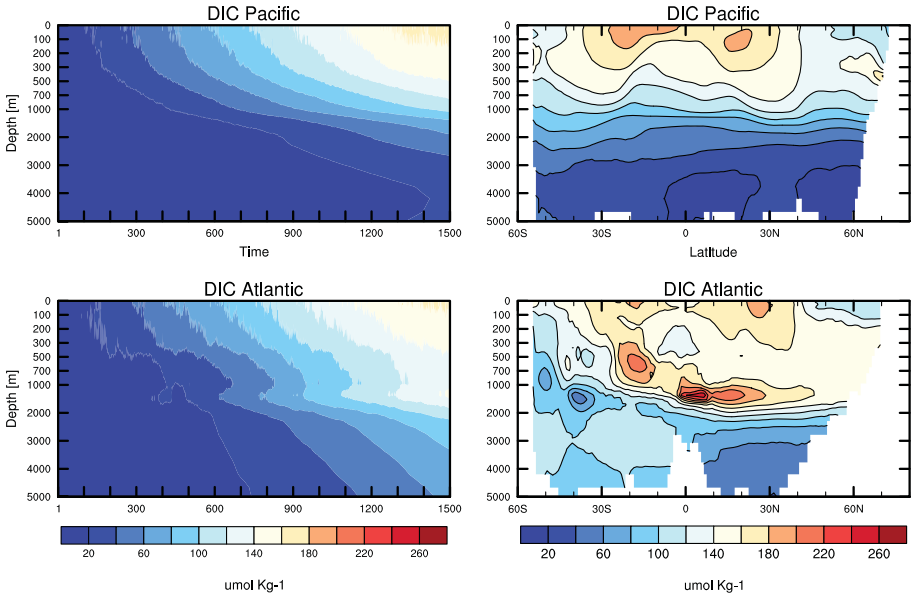

Figure 4.26: Left panel: Temporal evolution of anomaly (*no warming-control*) in DIC concentrations, integrated over the whole Pacific and Atlantic. Right panel: Zonally averaged anomaly (30 year mean of *no warming-control*) in DIC concentrations for the Pacific and Atlantic. Note the non-linear vertical axes, used to zoom in the upper ocean layers.

4.6.3 Effects on $CaCO_3$ sediments

In the *no warming* scenario the net $CaCO_3$ sediment dissolution amounts to 154 Gt C, which is equal to a 19 % increase compared to the *medium* scenario. The same amount of $CaCO_3$ is dissolved in the *high* scenario, in which we prescribe a 50 % stronger atmospheric CO_2 increase than in the *no warming* simulation.

The permanent deep water formation in the *no warming* experiment enables stronger $CaCO_3$ dissolution in the sediments of the Pacific and Indian Ocean. The main deep-water formation areas are located in these two basins which allow a faster propagation of the carbon perturbation to depth and thus drive the dissolution of $CaCO_3$ in the deep sea. The sediment to ocean TA fluxes almost double in both basins over the simulation period (Figure 4.27). The Southern and Tethys Ocean experience only a smaller increase in $CaCO_3$ dissolution, while the Atlantic shows the opposite effect in response to the CO_2 increase. Less sedimentary $CaCO_3$ is dissolved than in the *medium* simulation. The TA flux indicates that the Atlantic is characterized by net sedimentation throughout the simulation, although, the $CaCO_3$ export from the surface decreases with time. The permanent thermohaline circulation seems to be contra productive in achieving $CaCO_3$ dissolution in the deep Atlantic. While in the *medium* simulation the remnants of OM remineralization in the intermediate waters (due to the stagnation of the Atlantic circulation) drive the undersaturation of the deep ocean, this effect does not occur in the *no warming* simulation. The *no warming* scenario produces a $CaCO_3$ dissolution pattern between Atlantic and Pacific sediments which is the opposite of what is recorded in PETM sediment cores (Zachos et al. 2005; Zeebe et al. 2009).

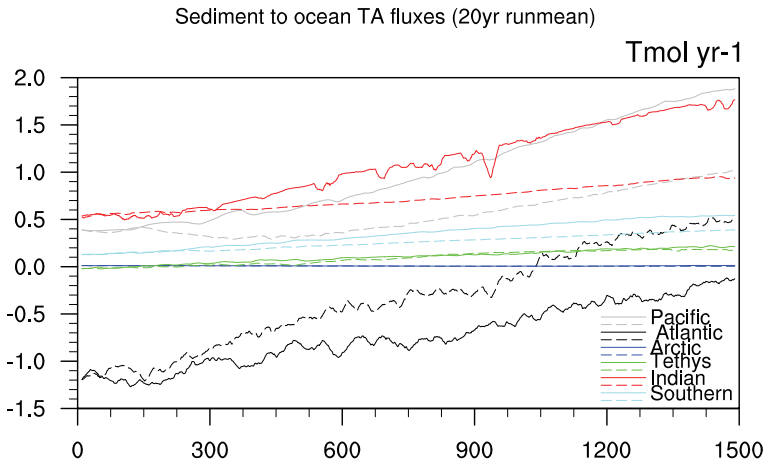

Figure 4.27: Sediment to ocean absolute TA flux (Terra mol yr^{-1}) for the *no warming* (solid lines) and the *medium* (dashed lines) simulation, averaged over the specific basins.

4.7 Summary & Discussion

We carry out several PETM related carbon perturbation scenarios and analyze the resulting response of the Earth system. In our analysis we focus primarily on the changes in the ocean biogeochemistry and how this could have led to the different signals we see in proxy record.
According to proxy data (e.g., summarized by Zeebe et al. 2009) SST rises by 6.5 ℃ (globally) with increasing atmospheric CO_2 concentrations in our simulation. Temperature increase occurs not uniformly. The meridional temperature gradient flattens throughout the simulation since high latitudes warm stronger than low latitudes. Moreover, the hydrological cycle intensifies with increasing atmospheric CO_2. As a consequence ocean freshwater input increases, especially in the mid to high latitudes where the main deep water formation areas are located. The reduced meridional temperature gradient and the increased freshwater input weaken the meridional overturning circulation (MOC) by 65 % and with it the formation and descend of water masses in mid to high latitudes. A weakening of deepwater formation in response to PETM warming is also consistent with proxy data (Tripati and Elderfield 2005; Nunes and Norris 2006).
The generally more stratified ocean is characterized by a shallow mixed layer depth (MLD) and low nutrient concentrations at the sea surface. Reduced upwelling disturbs the nutrient recycling within the uppermost several hundred meters of the water column. Instead, nutrient concentrations are enriched in the intermediate ocean waters >1000 m depth, where remineralization of organic matter (OM) also releases CO_2 and consumes oxygen. The stratification of the ocean prevents the upwelling of the CO_2 rich and oxygen poor waters to the surface again. Oxygen minimum zones (OMZ) expand subsequently. This process occurs in all basins in our simulation, but the enrichment of OM remnants is strongest in the Atlantic.
The weakening of Southern Ocean deep water ventilation causes the physical carbon pump to be less effective during the PETM. Nevertheless, DIC is transported to depth via this mechanism in the Pacific and causes undersaturation and $CaCO_3$ dissolution. However, no deep water formation takes place in the Atlantic in our simulation. Instead the accumulation of metabolic CO_2 acts as the main driver for Atlantic undersaturation. In response to increasing DIC concentrations, the deep ocean gets acidified and the carbonate ion concentrations decrease accordingly. The ratio between South Atlantic and Pacific carbonate ion concentrations (1:1.5) matches the argumentation of Zeebe and Zachos (2007); Zeebe et al. (2009) for the PETM main dissolution phase. The Atlantic Ocean is stronger affected by ocean acidification and thus sedimentary $CaCO_3$ is faster and stronger dissolved, also because of lower carbonate ion concentrations in the pre-PETM state (making Atlantic $CaCO_3$ more vulnerable to dissolution beforehand). The Pacific and Atlantic sedimentary $CaCO_3$ dissolution resulting from our simulation is confirming stronger CCD shoaling in the Atlantic than in the Pacific

Ocean (Zachos et al. 2007; Zeebe et al. 2009).
After 3000 years, the Pacific and the Atlantic Ocean are both strongly undersaturated in respect to $CaCO_3$, representing inhospitable conditions for benthic calcifiers. Moreover, the poor ventilation leads to a reduction in basin averaged oxygen concentrations of more than 100 μmol L^{-1} in the deep Atlantic and about 60 μmol L^{-1} in the deep Pacific. This results neither in the Atlantic nor in the Pacific in anoxia, but oxygen concentrations are not approaching an equilibrium state at the end of the simulation and will likely drop further in the prolongation of the experiment. According to the paleo-record the extinction was particularly strong among deep-sea calcifiers and less severe inside agglutinating species (Ridgwell and Schmidt 2010), which are not affected by $CaCO_3$ undersaturation.
At the surface the decreased nutrient availability leads to a 30 % reduction in net primary production (NPP), globally. The comparison of our results to the compilation of production tendencies in response to the PETM carbon perturbation (Winguth et al. 2012) looks promising except in the Tethys Ocean where NPP seem to have increased during the event (but remain unchanged or decreased in our simulation). This deviation from the proxy record is probably caused by not coupling the weathering and nutrient input to the terrestrial runoff (Winguth et al. 2010, 2012).
$CaCO_3$ production does not decrease in our simulation although it depends on the saturation state with respect to calcite (Ω). According to observational studies the onset of the PETM was rather characterized by dissolution of $CaCO_3$ in the water column than by a decrease in $CaCO_3$ production in the surface ocean (Stoll et al. 2007; Zeebe and Zachos 2007). Moreover, calcareous planktic organisms did not suffer severe extinction during the PETM (Thomas 2007).
The globally averaged surface pH declines by 0.28, which is very close to the estimates of Penman et al. (2014). They reconstructed a drop of 0.3 in surface pH based on boron proxies. Concomitantly, with the decline in pH Ω decreases, but the surface ocean stays supersaturated with respect to $CaCO_3$ throughout the simulation. Ω seems not to have been detrimental to the survival of most $CaCO_3$ bearing nannoplankton (Gibbs et al. 2006b).
The *ocean source* scenario in which we prescribe an artificial carbon source in the deep Atlantic results in almost the same physical and biogeochemical state than the *medium* simulation (Figure 4.4 & 4.10). However, the sedimentary $CaCO_3$ dissolution is highly increased in the Atlantic. Methane hydrate decomposition is discussed in the literature as a very possible mechanism for driving the PETM warming and the CIE (Dickens et al. 1995; Thomas et al. 2002; Zeebe et al. 2009). Our numerical modeling approach shows that the effects of such a carbon source would be mainly confined to the Atlantic basin, as the surrounding oceans show just slightly increased $CaCO_3$ dissolution. Depending on the degree of $CaCO_3$ dissolution which has to be achieved in the Atlantic to meet the CCD shoaling recorded in the sediment, the Atlantic carbon source seems

to be a functioning mechanism to produce it.
Climate change induced processes are intensified in the *high* scenario. Over the simulation period the SST increases by 9.5 ℃. The simulation enters some runaway-like climate state, since the warming proceeds constantly even though CO_2 concentrations are fixed over the last 200 years of the experiment (Figure 4.4). The surface temperatures increase is too strong in comparison to the paleo-temperature record (Kennett and Stott 1991; Zachos et al. 2003), precluding the simulation from representing a possible emission scenario for the PETM. Furthermore, the surface pH decrease of 3.7 is rather strong in comparison to proxy data (Penman et al. 2014) and other model simulations (Ridgwell and Schmidt 2010; Hoenisch et al. 2012). The deep sea carbonate chemistry just alters slightly between the *high* and *medium* simulation.
We simulated the *medium* scenario also in a radiatively uncoupled version, such that CO_2 is treated as a nonradiatively active gas (*no warming* simulation), to further investigate the warming induced effects on ocean biogeochemistry during the PETM. The simulation is confirming that the warming induced ocean stratification plays a major role related to the carbon perturbation during the PETM. The permanent deep water formation in the Pacific and Indian Ocean enables the descending of CO_2 enriched waters and with this a stronger dissolution in the same basins. Since the proximity to where carbon enters the deep sea via circulation dictates where neutralization by carbonate dissolution is most intense (Zachos et al. 2005). The Atlantic shows by contrast a strong depletion in DIC concentrations and hence less sedimentary $CaCO_3$ dissolution in comparison to the *medium* simulation. The intermediate and bottom waters get not/less corrosive in the absence of metabolic CO_2 accumulation due to maintained vertical mixing processes. $CaCO_3$ bearing sediments in the *no warming* simulation reveal an absolute increase in dissolution compared to the *medium* simulation on a global scale, but the dissolution ratio between the basins is not in accordance with the dissolution record from PETM sediments (Zachos et al. 2005; Zeebe et al. 2009).
The weakening of circulation and mixing in response to the PETM carbon perturbation seem to have been essential to establish deep ocean conditions which produced the PETM warming and acidification signals in the proxy record. While the reduction in Southern Ocean deep water formation causes a weakening of the physical carbon pump to inject CO_2 into the deep Pacific, the stagnating conditions in the Atlantic lead to corrosive deep sea conditions by trapping and remineralization of OM. Moreover, the carbon-climate feedback reduced the efficiency of the oceanic CO_2 absorption, promoting the maintenance of elevated atmospheric CO_2 concentrations and temperatures throughout the event.

Chapter 5

Conclusions and Outlook

5.1 Conclusions

I use the comprehensive Earth System Model MPI-ESM to simulate the warm climate of the Late Paleocene and the carbon perturbation which is associated with the PETM. I provide a detailed representation of the Late Paleocene ocean biogeochemistry state and address uncertainties, which arise from proxy data analysis, in the deep ocean carbonate chemistry before the PETM. In a set of transient CO_2 increase scenarios I analyze the response of the Earth system to the PETM related carbon perturbation, in order to reproduce the proxy record. I conclude the thesis by revisiting the research questions posed in the introduction.

1.) **Can the ocean biogeochemistry of the Late Paleocene be further constrained by using a complex ESM?**

Yes, I show that, while corresponding to the atmospheric CO_2 content, vertical and horizontal ocean biogeochemistry tracer distributions during the Late Paleocene are shaped by the warm and sluggish ocean circulation. The strong stratification of water masses is displayed by temperature and salinity profiles and a shallow mixed layer. The recycling of nutrients is less efficient than in modern conditions, which leads to slightly reduced primary production compared to present-day. Due to thermal induced stratification of the ocean, the upwelling regions in the equatorial Pacific and the South Atlantic exhibit extended oxygen minimum zones in intermediate waters. The surface ocean shows TA concentrations similar to modern conditions, despite the generally higher atmospheric CO_2 concentrations of 560 ppm. Yet, consistent with the higher atmospheric CO_2 the surface ocean pH and the saturation state with respect to $CaCO_3$ are lower than today. The simulated surface pH is in accordance to other Late Paleocene modelling studies, but based on a much lower $CaCO_3$:opal export ratio, than the one prescribed in intermediate complexity modelling studies of the Late Paleocene. The simulated distribution of sedimentary $CaCO_3$ captures the spatial patterns and absolute values of the proxy record by reflecting biogeochemical processes of the water column.

2.) **Does the Late Paleocene climate state influence the ocean biogeochemistry's sensitivity towards a carbon perturbation during the PETM?**

Yes, the Late Paleocene climate state influenced the ocean biogeochemistry response to the PETM already beforehand. The Late Paleocene surface ocean pH and the $CaCO_3$ saturation state result in an effectively lower carbonate buffer capacity towards a carbon perturbation during the PETM. This higher sensitivity of the surface ocean carbonate chemistry is slightly counteracted by the elevated Late Paleocene surface temperatures, which increases the $CaCO_3$ saturation state (by lowering the $CaCO_3$ saturation concentration).
The deep ocean $CaCO_3$ sediments are less vulnerable to dissolution due to the temperature effect and the vertically stratified ocean. The stratification diminishes the CO_2 transport to depth via vertical mixing processes (physical carbon pump).
Given that the Late Paleocene ocean circulation was driven by Southern Hemisphere deepwater formation, the Atlantic Ocean shows lower carbonate ion concentrations than the Pacific at depth. This reversal in deep sea carbonate ion concentrations between the Pacific and Atlantic in comparison to modern conditions is probably one of the reasons for the much stronger $CaCO_3$ dissolution in the Atlantic than in the Pacific during the PETM, which is suggested by proxy data.

3.) **How did the ocean circulation affect the marine carbon cycle and the biology in response to the PETM carbon perturbation?**

The weakening of the MOC and concomitant changes in ocean circulation in response to the CO_2 induced warming have been essential for reproducing the PETM related proxy record. The changes in the ocean circulation play a key role in establishing the $CaCO_3$ dissolution record associated with the PETM.
Biologically produced organic matter (OM) sinks and is remineralized in intermediate depth waters. In response to atmospheric CO_2 increase, warming and stratification of the ocean cause a reduction in vertical mixing of water masses. As a result, the products of decomposition of OM are trapped in intermediate waters, increasing CO_2 and thereby increasing DIC concentrations and consuming oxygen (promoting strong deoxygenation). Since the upwelling of carbon rich waters to the surface is not promoted by the circulation anymore, this increase in metabolic CO_2 leads to corrosive conditions with respect to $CaCO_3$ throughout the water column and triggers sedimentary $CaCO_3$ dissolution in the deep ocean. Especially in the Atlantic, the remineralization rather than the physical mixing from the surface provides the deep ocean with carbon. In the Pacific some deep sea ventilation remains throughout the PETM simulation. Consequently, the $CaCO_3$ dissolution is higher in the Atlantic than in the Pacific. The *no warming* simulation emphasizes the importance of ocean stratification for establishing PETM conditions, since undersaturation and sediment dissolution is much weaker at

permanent deep ocean ventilation. The comparison of the *medium* and the *no warming* simulation shows that while in the Pacific the strength of the circulation and mixing enhances the undersaturation of the deep ocean, it is the other way around in the Atlantic. The stagnation of the ocean mixing establishes corrosive deep sea conditions in the Atlantic via the production of metabolic CO_2.
In terms of the biology, the ocean circulation response to the carbon perturbation results in a strong reduction in open ocean productivity, since decreased upwelling of nutrient rich waters weakens the nutrient supply of the surface ocean. However, the surface ocean features hospitable conditions throughout the simulation for calcifiers, meaning that it does not get undersaturated with respect to $CaCO_3$. In the deep ocean, the benthos is facing low oxygen concentrations (but no pronounced anoxic conditions) and highly undersaturated waters with respect to $CaCO_3$. Moreover, the decrease in productivity could have harmed the benthos and led to starvation of benthic organisms by supplying less OM. Our results show poorly ventilated, partly dysoxic and highly undersaturated intermediate and deep oceans. This phenomenon is more pronounced in the Atlantic Ocean. The Pacific is still somewhat better ventilated but undersaturation occurs through the transport of carbon from the surface. In accordance with proxy data, the conditions in the deep ocean are less hospitable for $CaCO_3$ than organic-agglutinated foraminifera at the end of the simulation.

4.) **What is the relevance of different sources and rates of carbon perturbation for the marine biogeochemistry?**

Based on our modelling approach, an atmospheric CO_2 increase equivalent to an emission of 1 Gt carbon per year (*medium* scenario) is the highest atmospheric carbon release rate necessary to reproduce the proxy record of the PETM. Stronger CO_2 increase (1.5 Gt yr^{-1} in *high* scenario) produces warmer surface temperatures of >8 ℃, which is inconsistent with temperature reconstructions. Furthermore, a decrease in surface pH of 3.7 is produced which is rather strong in comparison to proxy data.
Since the physical carbon pump is further weakened with the additional temperature increase and poor ventilation, the deep sea (>2000 m depth) carbonate chemistry does not alter extensively between the *high* and *medium* scenario over the simulated period. Consequently, the higher atmospheric CO_2 increase rates do not increase the dissolution of deep sea $CaCO_3$ sediments.
Modelling studies concerning the present-day and future high CO_2 world ocean show that the carbon input rate determines the effect on ocean carbonate chemistry in the next several hundred years (Zeebe et al. 2008; Ilyina and Zeebe 2012). According to our results, this is not the same for the PETM. The stagnation of the ocean and the isolation effect of the deep ocean due to the reduced ventilation exceed the effect of higher input rates of carbon from the atmosphere.

Including a deep Atlantic carbon source (*ocean source* scenario) provides severe undersaturation and dissolution of sedimentary $CaCO_3$. The Atlantic exhibits much stronger dissolution of sedimentary $CaCO_3$ than the Pacific Ocean. Our numerical modeling approach shows that the effects of such a carbon source would be mainly restricted to the Atlantic basin, as the surrounding oceans just show slight increases in sedimentary $CaCO_3$ dissolution. Depending on the degree of carbonate dissolution which has to be achieved in the Atlantic in comparison to the Pacific to meet the carbonate compensation depth (CCD) shoaling recorded in the proxy data, the Atlantic carbon source seems to be a functioning mechanism to produce it. Moreover, since different proxy record studies do not agree entirely on the deepwater formation response during the PETM, the deep Atlantic carbon source would be useful to produce the $CaCO_3$ dissolution record if changes in ocean circulation would favor a deep Atlantic ventilation in response to the carbon perturbation. Although, the weaker ocean acidification and deoxygenation due to the missing metabolic CO_2 would then at least partly be compensated by a higher amount of CO_2 rich waters, transported into the deep Atlantic by intensified mixing.

5.) **Did feedback mechanisms between climate and ocean carbon cycle play a role for maintaining elevated atmospheric CO_2 and temperatures throughout the PETM?**

Yes, climate change induced feedbacks in the carbon cycle reduce the oceanic CO_2 uptake (-17 %) due to global temperature increase. The reduced vertical mixing decreases the carbon transport to depth. Consequently the surface ocean gets supersaturated with respect to CO_2 more quickly and more CO_2 stays in the atmosphere causing a prolonged greenhouse effect. If the simulation includes an additional carbon source in the deep ocean the feedback process is enhanced and the oceanic CO_2 uptake is further decreased (-23 %).
Based on results of present-day studies with the MPI-ESM, investigating the MOC response to atmospheric CO_2 increase on longer timescales, I assume that the reduced deepwater formation conditions, which are the main reason for the decrease in oceanic CO_2 uptake, would proceed in a prolongation of the PETM modelling experiments. Moreover, the development of unstable stratification in the Southern Ocean during the PETM (which would increase the deep ocean ventilation again) is additionally prevented by the absence of seasonal sea ice, which embodies a mechanism to ventilate the deep ocean on a multi-millennial timescale in modern conditions.
Assuming a carbon perturbation of 10.000 years the carbon climate feedback likely played a role in maintaining elevated atmospheric CO_2 concentrations and temperatures during the event. However, the strength of the carbon cycle feedback is determined by the weakening of the circulation and vertical mixing. The climate change

effect on the carbon cycle is probably one of the feedback processes which drove the prolonged warming throughout the PETM.

5.2 Outlook

The modelling study presented here could be extended by incorporating additional processes and testing further hypothesis. Such as:

- Proxy data analysis suggest increasing production rates in coastal regions during the PETM. Our results are not capable to reproduce this production increase, which implies that some mechanisms is not considered yet in the models. A plausible mechanisms could lie in higher weathering rates due to an increase in extra-tropical precipitation during the PETM, which could potentially washout more nutrients, transport them to coastal areas and hence drive the production increases in coastal regions (Winguth et al. 2012, and references therein). In this context it would be of interest to couple the weathering flux to the atmospheric CO_2 concentration or to the hydrological cycle in HAMOCC. By this the nutrient availability in the shelf regions would be increased, which would help to reduce the gap between our model results and the proxy data.

- Another limitation of this study is the relatively short timescale (3 krs) over which the simulations are computed, compared to the overall duration of the PETM of 170 kyrs. The prolongation of the simulations could reveal valuable information. For instance, on the long-term behavior of the ocean circulation. Furthermore, on the evolution of anoxic conditions in the deep ocean and changes in the $CaCO_3$ dissolution pattern if the stratification of the ocean proceeds. Since both the deoxygenation and the acidification are dealt as the major contributors related to the benthic extinction. Finally, modelling the tail part of the PETM including the (weathering induced) draw down of atmospheric CO_2 would be a promising topic.

- We tried already in the context of this study to spin up the coupled model in the PETM setup, using an interactive carbon cycle including emission driven carbon perturbation scenarios. However, due to some major problems in the atmosphere-ocean CO_2 exchange, which we ascribe to the higher atmospheric CO_2 concentrations in the PETM setup relative to present-day, we did not get the model in a reasonable steady-state. To run the model interactively would give a more comprehensive picture of the carbon cycle during the PETM. Future work should consider also the feedbacks of the terrestrial carbon cycle and vegetation

on the ocean biogeochemistry.

- As shown in this thesis the ocean circulation has a major impact on the marine carbon cycle during the PETM. It is necessary to intensify the analysis of PETM circulation changes both in numerical modelling and especially in proxy data studies. For a successful model versus observation comparison, more studies on proxy data would be desirable to precisely reconstruct the evolution of the deepwater formation areas in the Northern and Southern Hemisphere during the event.

Bibliography

Andrews, O. D., N. L. Bindoff, P. R. Halloran, T. Ilyina, and C. Le Quéré, 2013: Detecting an external influence on recent changes in oceanic oxygen using an optimal fingerprinting method. *Biogeosciences*, **10 (3)**, 1799–1813, doi:10.5194/bg-10-1799-2013, URL `http://www.biogeosciences.net/10/1799/2013/`.

Arakawa, A. and V. R. Lamb, 1977: Computational design of the basic dynamical processes of the UCLA general circulation model. *Methods in computational physics*, **17**, 173–265.

Archer, D., H. Kheshgi, and E. Maier-Reimer, 1998: Dynamics of fossil fuel CO2 neutralization by marine CaCO3. *Global Biogeochem. Cycles*, **12 (2)**, 259–276, URL `http://dx.doi.org/10.1029/98GB00744`.

Archer, D., P. Martin, B. Buffett, V. Brovkin, S. Rahmstorf, and A. Ganopolski, 2004: The importance of ocean temperature to global biogeochemistry. *Earth and Planetary Science Letters*, **222 (2)**, 333–348.

Arora, V. K., et al., 2013: Carbon-Concentration and Carbon-Climate Feedbacks in CMIP5 Earth System Models. *J. Climate*, **26 (15)**, 5289–5314, doi:10.1175/JCLI-D-12-00494.1, URL `http://dx.doi.org/10.1175/JCLI-D-12-00494.1`.

Bains, S., R. D. Norris, R. M. Corfield, and K. L. Faul, 2000: Termination of global warmth at the Palaeocene/Eocene boundary through productivity feedback. *Nature*, **407 (6801)**, 171–174, URL `http://dx.doi.org/10.1038/35025035`.

Bice, K. L. and J. Marotzke, 2001: Numerical evidence against reversed thermohaline circulation in the warm Paleocene/Eocene ocean. *J. Geophys. Res.*, **106 (C6)**, 11 529–11 542, URL `http://dx.doi.org/10.1029/2000JC000561`.

Bice, K. L. and J. Marotzke, 2002: Could changing ocean circulation have destabilized methane hydrate at the Paleocene/Eocene boundary? *Paleoceanography*, **17 (2)**, 1018–1033, doi:10.1029/2001PA000678, URL `http://dx.doi.org/10.1029/2001PA000678`.

Bopp, L., C. Le Quere, M. Heimann, A. C. Manning, and P. Monfray, 2002: Climate-induced oceanic oxygen fluxes: Implications for the contemporary carbon budget.

Global Biogeochem. Cycles, **16 (2)**, 6–1–6–13, URL http://dx.doi.org/10.1029/2001GB001445.

Bopp, L., et al., 2013: Multiple stressors of ocean ecosystems in the 21st century: projections with CMIP5 models. *Biogeosciences*, **10 (10)**, 6225–6245, doi:10.5194/bg-10-6225-2013, URL http://www.biogeosciences.net/10/6225/2013/.

Bowen, G. J., D. J. Beerling, P. L. Koch, J. C. Zachos, and T. Quattlebaum, 2004: A humid climate state during the Palaeocene/Eocene thermal maximum. *Nature*, **432 (7016)**, 495–499, URL http://dx.doi.org/10.1038/nature03115.

Bralower, T. J., 2002: Evidence of surface water oligotrophy during the Paleocene-Eocene thermal maximum: Nannofossil assemblage data from Ocean Drilling Program Site 690, Maud Rise, Weddell Sea. *Paleoceanography*, **17 (2)**, 1023–, URL http://dx.doi.org/10.1029/2001PA000662.

Brovkin, V., T. Raddatz, C. H. Reick, M. Claussen, and V. Gayler, 2009: Global biogeophysical interactions between forest and climate. *Geophys. Res. Lett.*, **36 (7)**, L07 405–, URL http://dx.doi.org/10.1029/2009GL037543.

Cocco, V., et al., 2013: Oxygen and indicators of stress for marine life in multi-model global warming projections. *Biogeosciences*, **10 (3)**, 1849–1868, doi:10.5194/bg-10-1849-2013, URL http://www.biogeosciences.net/10/1849/2013/.

Cui, Y., et al., 2011: Slow release of fossil carbon during the Palaeocene-Eocene Thermal Maximum. *Nature Geosci*, **4 (7)**, 481–485, URL http://dx.doi.org/10.1038/ngeo1179.

de Boyer Montegut, C., G. Madec, A. S. Fischer, A. Lazar, and D. Iudicone, 2004: Mixed layer depth over the global ocean: An examination of profile data and a profile-based climatology. *J. Geophys. Res.*, **109 (C12)**, C12 003–, URL http://dx.doi.org/10.1029/2004JC002378.

Dickens, G. R., 1999: Carbon cycle: The blast in the past. *Nature*, **401 (6755)**, 752–755, URL http://dx.doi.org/10.1038/44486.

Dickens, G. R., 2000: Methane oxidation during the late Paleocene thermal maximum. *Bull. Soc. Geol. France*, **171(1)**, 37–49.

Dickens, G. R., M. M. Castillo, and J. C. G. Walker, 1997: A blast of gas in the latest Paleocene: Simulating first-order effects of massive dissociation of oceanic methane hydrate. *Geology*, **25 (3)**, 259–262, doi:10.1130/0091-7613(1997)025⟨0259:ABOGIT⟩2.3.CO;2, URL http://geology.gsapubs.org/content/25/3/259.abstract, http://geology.gsapubs.org/content/25/3/259.full.pdf+html.

Dickens, G. R., J. R. O'Neil, D. K. Rea, and R. M. Owen, 1995: Dissociation of oceanic methane hydrate as a cause of the carbon isotope excursion at the end of the Paleocene. *Paleoceanography*, **10 (6)**, 965–971, URL http://dx.doi.org/10.1029/95PA02087.

Dunkley Jones, T., A. Ridgwell, D. J. Lunt, M. A. Maslin, D. N. Schmidt, and P. J. Valdes, 2010: A Palaeogene perspective on climate sensitivity and methane hydrate instability. *Philosophical Transactions of the Royal Society A: Mathematical,Physical and Engineering Sciences*, **368 (1919)**, 2395–2415, doi:10.1098/rsta.2010.0053, http://rsta.royalsocietypublishing.org/content/368/1919/2395.full.pdf+html.

Feely, R. A., C. L. Sabine, K. Lee, W. Berelson, J. Kleypas, V. J. Fabry, and F. J. Millero, 2004: Impact of Anthropogenic CO2 on the CaCO3 System in the Oceans. *Science*, **305 (5682)**, 362–366, URL http://www.sciencemag.org/content/305/5682/362.abstract.

Fouquart, Y. and B. Bonnel, 1980: Computations of solar heating of the earth's atmosphere- A new parameterization. *Beitraege zur Physik der Atmosphaere*, **53**, 35–62.

Friedlingstein, P., et al., 2006: ClimateâCarbon Cycle Feedback Analysis: Results from the C4MIP Model Intercomparison. *J. Climate*, **19 (14)**, 3337–3353, doi:10.1175/JCLI3800.1, URL http://dx.doi.org/10.1175/JCLI3800.1.

Gent, P. R., J. Willebrand, T. J. McDougall, and J. C. McWilliams, 1995: Parameterizing eddy-induced tracer transports in ocean circulation models. *Journal of Physical Oceanography*, **25 (4)**, 463–474.

Gibbs, S. J., P. R. Bown, J. A. Sessa, T. J. Bralower, and P. A. Wilson, 2006a: Nannoplankton Extinction and Origination Across the Paleocene-Eocene Thermal Maximum. *Science*, **314 (5806)**, 1770–1773, doi:10.1126/science.1133902, http://www.sciencemag.org/content/314/5806/1770.full.pdf.

Gibbs, S. J., T. J. Bralower, P. R. Bown, J. C. Zachos, and L. M. Bybell, 2006b: Shelf and open-ocean calcareous phytoplankton assemblages across the Paleocene-Eocene Thermal Maximum: Implications for global productivity gradients. *Geology*, **34 (4)**, 233–236, URL http://geology.gsapubs.org/content/34/4/233.abstract.

Gibbs, S. J., et al., 2013: Species-specific growth response of coccolithophores to Palaeocene-Eocene environmental change. *Nature Geosci*, **6 (3)**, 218–222, URL http://dx.doi.org/10.1038/ngeo1719.

Giorgetta, M. A., et al., 2013: Climate and carbon cycle changes from 1850 to 2100 in MPI-ESM simulations for the Coupled Model Intercomparison Project phase 5. *J. Adv. Model. Earth Syst.*, **5 (3)**, 572–597, URL http://dx.doi.org/10.1002/jame.20038.

Groeger, M. and U. Mikolajewicz, 2011: Note on the CO2 air–sea gas exchange at high temperatures. *Ocean Modelling*, **39 (3–4)**, 284–290, URL http://www.sciencedirect.com/science/article/pii/S1463500311000886.

Hagemann, S. and L. Gates, 2003: Improving a subgrid runoff parameterization scheme for climate models by the use of high resolution data derived from satellite observations. *Climate Dynamics*, **21 (3-4)**, 349–359, URL http://dx.doi.org/10.1007/s00382-003-0349-x.

Heinemann, M., 2009: *Warm and sensitive Paleocene-Eocene climate*, Reports on Earth System Science, Vol. 70. Max-Planck-Inst. für Meteorologie, Hamburg.

Heinemann, M., J. H. Jungclaus, and J. Marotzke, 2009: Warm Paleocene/Eocene climate as simulated in ECHAM5/MPI-OM. *Climate of the Past*, **5 (4)**, 785–802, doi:10.5194/cp-5-785-2009, URL http://www.clim-past.net/5/785/2009/.

Heinze, C., A. Hupe, E. Maier-Reimer, N. Dittert, and O. Ragueneau, 2003: Sensitivity of the marine biospheric Si cycle for biogeochemical parameter variations. *Global Biogeochem. Cycles*, **17 (3)**, 1086–, URL http://dx.doi.org/10.1029/2002GB001943.

Heinze, C. and E. Maier-Reimer, 1999: The Hamburg Oceanic Carbon Cycle Circulation Model version "HAMOCC2s" for longtime integrations. *Technical Report 20. Deutsches Klimarechenzenrum, Modellberatungsgruppe, Hamburg.*

Heinze, C., E. Maier-Reimer, A. M. E. Winguth, and D. Archer, 1999: A global oceanic sediment model for long-term climate studies. *Global Biogeochem. Cycles*, **13 (1)**, 221–250, URL http://dx.doi.org/10.1029/98GB02812.

Heinze, C., E. Maier-Reimer, and K. Winn, 1991: Glacial pCO2 Reduction by the World Ocean: Experiments With the Hamburg Carbon Cycle Model. *Paleoceanography*, **6 (4)**, 395–430, URL http://dx.doi.org/10.1029/91PA00489.

Heinze, M. and T. Ilyina, 2014: Ocean Biogeochemistry in the warm climate of the Late Paleocene. *Climate of the Past Discussions*, **10 (2)**, 1933–1975, doi:10.5194/cpd-10-1933-2014, URL http://www.clim-past-discuss.net/10/1933/2014/.

Hibler, W. D., 1979: A Dynamic Thermodynamic Sea Ice Model. *J. Phys. Oceanogr.*, **9 (4)**, 815–846, URL http://dx.doi.org/10.1175/1520-0485(1979)009<0815:ADTSIM>2.0.CO;2.

Hoenisch, B., et al., 2012: The Geological Record of Ocean Acidification. *Science*, **335 (6072)**, 1058–1063.

Huber, M., L. Sloan, and C. Shellito, 2003: *Early Paleogene Oceans and Climate: a Fully Coupled Modeling Approach Using the NCAR CCSM*, in: Causes and Consequences of Globally Warm Climates in the Paleogene, Geological Society of America, Special Paper, Vol. 369. Geological Society of America, Boulder, 25-47 pp.

Huber, M. and L. C. Sloan, 2001: Heat transport, deep waters, and thermal gradients: Coupled simulation of an Eocene greenhouse climate. *Geophys. Res. Lett*, **28 (18)**, 3481–3484.

Iacono, M. J., J. S. Delamere, E. J. Mlawer, M. W. Shephard, S. A. Clough, and W. D. Collins, 2008: Radiative forcing by long-lived greenhouse gases: Calculations with the AER radiative transfer models. *J. Geophys. Res.*, **113 (D13)**, D13 103, URL http://dx.doi.org/10.1029/2008JD009944.

Ilyina, T., K. D. Six, J. Segschneider, E. Maier-Reimer, H. Li, and I. Nunez-Riboni, 2013: Global ocean biogeochemistry model HAMOCC: Model architecture and performance as component of the MPI-Earth system model in different CMIP5 experimental realizations. *J. Adv. Model. Earth Syst.*, **5 (2)**, 287–315, URL http://dx.doi.org/10.1029/2012MS000178.

Ilyina, T. and R. E. Zeebe, 2012: Detection and projection of carbonate dissolution in the water column and deep-sea sediments due to ocean acidification. *Geophys. Res. Lett.*, **39 (6)**, L06 606–, URL http://dx.doi.org/10.1029/2012GL051272.

Ilyina, T., R. E. Zeebe, E. Maier-Reimer, and C. Heinze, 2009: Early detection of ocean acidification effects on marine calcification. *Global Biogeochem. Cycles*, **23 (1)**, GB1008–, URL http://dx.doi.org/10.1029/2008GB003278.

Jungclaus, J. H., et al., 2006: Ocean Circulation and Tropical Variability in the Coupled Model ECHAM5/MPI-OM. *Journal of Climate*, **19 (16)**, 3952–3972, URL http://search.ebscohost.com/login.aspx?direct=true&db=aph&AN=22671146&site=ehost-live&scope=site.

Jungclaus, J. H., et al., 2013: Characteristics of the ocean simulations in the Max Planck Institute Ocean Model (MPIOM) the ocean component of the MPI-Earth system model. *J. Adv. Model. Earth Syst.*, **5 (2)**, 422–446, URL http://dx.doi.org/10.1002/jame.20023.

Kennett, J. P. and L. D. Stott, 1991: Abrupt deep-sea warming, palaeoceanographic changes and benthic extinctions at the end of the Palaeocene. *Nature*, **353 (6341)**, 225–229, URL http://dx.doi.org/10.1038/353225a0.

Laskar, J., A. Fienga, M. Gastineau, and H. Manche, 2011: La2010: a new orbital solution for the long-term motion of the Earth. *Astronomy & Astrophysics*, **532**, A89, doi:10.1051/0004-6361/201116836, URL http://dx.doi.org/10.1051/0004-6361/201116836.

Li, C., 2012: *Long-term stability and adjustment toward equilibrium in a future warm climate*, Reports on Earth System Science, Vol. 119. Max-Planck-Inst. für Meteorologie, Hamburg.

Lin, S.-J. and R. B. Rood, 1996: Multidimensional flux-form semi-Lagrangian transport schemes. *Monthly Weather Review*, **124 (9)**, 2046–2070.

Lochte, K., H. Ducklow, M. Fasham, and C. Stienen, 1993: Plankton succession and carbon cycling at 47°N 20°W during the JGOFS North Atlantic Bloom Experiment. *Deep Sea Research Part II: Topical Studies in Oceanography*, **40 (1-2)**, 91–114, URL http://www.sciencedirect.com/science/article/pii/096706459390008B.

Lott, F. and M. J. Miller, 1997: A new subgridâscale orographic drag parametrization: Its formulation and testing. *Quarterly Journal of the Royal Meteorological Society*, **123 (537)**, 101–127.

Lunt, D. J., P. J. Valdes, T. D. Jones, A. Ridgwell, A. M. Haywood, D. N. Schmidt, R. Marsh, and M. Maslin, 2010: CO2-driven ocean circulation changes as an amplifier of Paleocene-Eocene thermal maximum hydrate destabilization. *Geology*, **38 (10)**, 875–878.

Lunt, D. J., et al., 2012: A model-data comparison for a multi-model ensemble of early Eocene atmosphere-ocean simulations: EoMIP. *Climate of the Past Discussions*, **8 (2)**, 1229–1273, doi:10.5194/cpd-8-1229-2012, URL http://www.clim-past-discuss.net/8/1229/2012/.

Mahowald, N. M., et al., 2005: Atmospheric global dust cycle and iron inputs to the ocean. *Global Biogeochem. Cycles*, **19 (4)**, GB4025–, URL http://dx.doi.org/10.1029/2004GB002402.

Maier-Reimer, E., 1993: Geochemical cycles in an ocean general circulation model. Preindustrial tracer distributions. *Global Biogeochem. Cycles*, **7 (3)**, 645–677, URL http://dx.doi.org/10.1029/93GB01355.

Maier-Reimer, E., I. Kriest, J. Segschneider, and P. Wetzel, 2005: The HAMburg Ocean Carbon Cycle Model HAMOCC 5.1. *Technical Decription Release 1.1, Tech. rep. 14, Reports on Earth System Science, Hamburg, Germany.*

Marsland, S., H. Haak, J. Jungclaus, M. Latif, and F. Röske, 2003: The Max-Planck-Institute global ocean/sea ice model with orthogonal curvilinear coordinates. *Ocean Modelling*, **5 (2)**, 91–127.

Mikolajewicz, U. and T. J. Crowley, 1997: Response of a coupled ocean/energy balance model to restricted flow through the central American isthmus. *Paleoceanography*, **12 (3)**, 429–441.

Mikolajewicz, U., E. Maier-Reimer, T. J. Crowley, and K.-Y. Kim, 1993: Effect of Drake and Panamanian gateways on the circulation of an ocean model. *Paleoceanography*, **8 (4)**, 409–426.

Miller, K. G., T. R. Janecek, M. E. Katz, and D. J. Keil, 1987: Abyssal circulation and benthic foraminiferal changes near the Paleocene/Eocene boundary. *Paleoceanography*, **2 (6)**, 741–761, URL `http://dx.doi.org/10.1029/PA002i006p00741`.

Monteiro, F. M., R. D. Pancost, A. Ridgwell, and Y. Donnadieu, 2012: Nutrients as the dominant control on the spread of anoxia and euxinia across the Cenomanian-Turonian oceanic anoxic event (OAE2): Model-data comparison. *Paleoceanography*, **27 (4)**, PA4209–, URL `http://dx.doi.org/10.1029/2012PA002351`.

Najjar, R. G., et al., 2007: Impact of circulation on export production, dissolved organic matter, and dissolved oxygen in the ocean: Results from Phase II of the Ocean Carbon-cycle Model Intercomparison Project (OCMIP-2). *Global Biogeochem. Cycles*, **21 (3)**, GB3007–, URL `http://dx.doi.org/10.1029/2006GB002857`.

Norris, R. D., S. K. Turner, P. M. Hull, and A. Ridgwell, 2013: Marine Ecosystem Responses to Cenozoic Global Change. *Science*, **341 (6145)**, 492–498, doi:10.1126/science.1240543, `http://www.sciencemag.org/content/341/6145/492.full.pdf`.

Nunes, F. and R. D. Norris, 2006: Abrupt reversal in ocean overturning during the Palaeocene/Eocene warm period. *Nature*, **439 (7072)**, 60–63.

Pacanowski, R. and S. Philander, 1981: Parameterization of vertical mixing in numerical models of tropical oceans. *Journal of Physical Oceanography*, **11 (11)**, 1443–1451.

Pagani, M., K. Caldeira, D. Archer, and J. C. Zachos, 2006a: An Ancient Carbon Mystery. *Science*, **314 (5805)**, 1556–1557, doi:10.1126/science.1136110, `http://www.sciencemag.org/content/314/5805/1556.full.pdf`.

Pagani, M., et al., 2006b: Arctic hydrology during global warming at the Palaeocene/Eocene thermal maximum. *Nature*, **443 (7111)**, 598–598, URL `http://dx.doi.org/10.1038/nature05211`.

Panchuk, K., A. Ridgwell, and L. Kump, 2008: Sedimentary response to Paleocene-Eocene Thermal Maximum carbon release: A model-data comparison. *Geology*, **36 (4)**, 315–318, doi:10.1130/G24474A.1, http://geology.gsapubs.org/content/36/4/315.full.pdf+html.

Pearson, P. N., P. W. Ditchfield, J. Singano, K. G. Harcourt-Brown, C. J. Nicholas, R. K. Olsson, N. J. Shackleton, and M. A. Hall, 2001: Warm tropical sea surface temperatures in the Late Cretaceous and Eocene epochs. *Nature*, **413 (6855)**, 481–487, URL http://dx.doi.org/10.1038/35097000.

Pearson, P. N. and M. R. Palmer, 2000: Atmospheric carbon dioxide concentrations over the past 60 million years. *Nature*, **406 (6797)**, 695–699, URL http://dx.doi.org/10.1038/35021000.

Penman, D. E., B. Hoenisch, R. E. Zeebe, E. Thomas, and J. C. Zachos, 2014: Rapid and sustained surface ocean acidification during the Paleocene-Eocene Thermal Maximum. *Paleoceanography*, **29 (5)**, 2014PA002 621–, URL http://dx.doi.org/10.1002/2014PA002621.

Ragueneau, O., et al., 2000: A review of the Si cycle in the modern ocean: recent progress and missing gaps in the application of biogenic opal as a paleoproductivity proxy. *Global and Planetary Change*, **26 (4)**, 317–365, URL http://www.sciencedirect.com/science/article/pii/S0921818100000527.

Reick, C. H., T. Raddatz, V. Brovkin, and V. Gayler, 2013: Representation of natural and anthropogenic land cover change in MPI-ESM. *J. Adv. Model. Earth Syst.*, **5 (3)**, 459–482, URL http://dx.doi.org/10.1002/jame.20022.

Ridgwell, A. and D. Schmidt, 2010: Past constraints on the vulnerability of marine calcifiers to massive carbon dioxide release. *Nature Geoscience*, **3 (3)**, 196–200.

Ridgwell, A. and R. Zeebe, 2005: The role of the global carbonate cycle in the regulation and evolution of the Earth system. *Earth and Planetary Science Letters*, **234 (3)**, 299–315.

Riebesell, U., I. Zondervan, B. Rost, P. D. Tortell, R. E. Zeebe, and F. M. M. Morel, 2000: Reduced calcification of marine plankton in response to increased atmospheric. *Nature*, **407 (6802)**, 364–367, URL http://dx.doi.org/10.1038/35030078.

Roberts, C. D., A. N. LeGrande, and A. K. Tripati, 2009: Climate sensitivity to Arctic seaway restriction during the early Paleogene. *Earth and Planetary Science Letters*, **286 (3-4)**, 576–585, URL http://www.sciencedirect.com/science/article/pii/S0012821X09004415.

Roeckner, E., 2003: *The atmospheric general circulation model ECHAM5: Model description*. Max-Planck-Institute for Meteorology.

Roeckner, E., T. Mauritsen, M. Esch, and R. Brokopf, 2012: Impact of melt ponds on Arctic sea ice in past and future climates as simulated by MPI-ESM. *Journal of Advances in Modeling Earth Systems*, **4 (3)**, M00A02.

Roeckner, E., et al., 2006: Sensitivity of Simulated Climate to Horizontal and Vertical Resolution in the ECHAM5 Atmosphere Model. *Journal of Climate*, **19 (16)**, 3771–3791, URL http://search.ebscohost.com/login.aspx?direct=true&db=aph&AN=22671141&site=ehost-live&scope=site.

Roeske, F., 2006: A global heat and freshwater forcing dataset for ocean models. *Ocean Modelling*, **11 (3)**, 235–297.

Sarmiento, J. L., J. Dunne, A. Gnanadesikan, R. M. Key, K. Matsumoto, and R. Slater, 2002: A new estimate of the CaCO3 to organic carbon export ratio. *Global Biogeochemical Cycles*, **16 (4)**, 54–1–54–12, doi:10.1029/2002GB001919, URL http://dx.doi.org/10.1029/2002GB001919.

Schneck, R., C. H. Reick, and T. Raddatz, 2013: Land contribution to natural CO2 variability on time scales of centuries. *J. Adv. Model. Earth Syst.*, **5 (2)**, 354–365, URL http://dx.doi.org/10.1002/jame.20029.

Schneider, B., et al., 2008: Climate-induced interannual variability of marine primary and export production in three global coupled climate carbon cycle models. *Biogeosciences*, **5 (2)**, 597–614, doi:10.5194/bg-5-597-2008, URL http://www.biogeosciences.net/5/597/2008/.

Schwinger, J., et al., 2014: Nonlinearity of Ocean Carbon Cycle Feedbacks in CMIP5 Earth System Models. *J. Climate*, **27 (11)**, 3869–3888, doi:10.1175/JCLI-D-13-00452.1, URL http://dx.doi.org/10.1175/JCLI-D-13-00452.1.

Seferian, R., et al., 2013: Skill assessment of three earth system models with common marine biogeochemistry. **40 (9-10)**, 2549–2573–, URL http://dx.doi.org/10.1007/s00382-012-1362-8.

Semtner, A. J., 1976: A Model for the Thermodynamic Growth of Sea Ice in Numerical Investigations of Climate. *J. Phys. Oceanogr.*, **6 (3)**, 379–389, doi:10.1175/1520-0485(1976)006⟨0379:AMFTTG⟩2.0.CO;2, URL http://dx.doi.org/10.1175/1520-0485(1976)006<0379:AMFTTG>2.0.CO;2.

Sijp, W. P., A. S. von der Heydt, H. A. Dijkstra, S. Floegel, P. M. Douglas, and P. K. Bijl, 2014: The role of ocean gateways on cooling climate on long time scales.

Global and Planetary Change, **119 (0)**, 1–22, URL http://www.sciencedirect.com/science/article/pii/S0921818114000691.

Six, K. and E. Maier-Reimer, 1996: Effects of plankton dynamics on seasonal carbon fluxes in an ocean general circulation model. *Global Biogeochemical Cycles*, **10 (4)**, 559–583.

Six, K. D., S. Kloster, T. Ilyina, S. D. Archer, K. Zhang, and E. Maier-Reimer, 2013: Global warming amplified by reduced sulphur fluxes as a result of ocean acidification. *Nature Clim. Change*, **3 (11)**, 975–978, URL http://dx.doi.org/10.1038/nclimate1981.

Sluijs, A., J. C. Zachos, and R. E. Zeebe, 2012: Constraints on hyperthermals. *Nature Geosci*, **5 (4)**, 231–231, URL http://dx.doi.org/10.1038/ngeo1423.

Sluijs, A., et al., 2006: Subtropical Arctic Ocean temperatures during the Palaeocene/Eocene thermal maximum. *Nature*, **441 (7093)**, 610–613, URL http://dx.doi.org/10.1038/nature04668.

Stevens, B., et al., 2013: Atmospheric component of the MPI-M Earth System Model: ECHAM6. *J. Adv. Model. Earth Syst.*, **5 (2)**, 146–172, URL http://dx.doi.org/10.1002/jame.20015.

Stoll, H. M., N. Shimizu, D. Archer, and P. Ziveri, 2007: Coccolithophore productivity response to greenhouse event of the PaleoceneâEocene Thermal Maximum. *Earth and Planetary Science Letters*, **258 (1–2)**, 192–206, doi:10.1016/j.epsl.2007.03.037, URL http://www.sciencedirect.com/science/article/pii/S0012821X07001902.

Svensen, H., S. Planke, A. Malthe-Sørenssen, B. Jamtveit, R. Myklebust, T. R. Eidem, and S. S. Rey, 2004: Release of methane from a volcanic basin as a mechanism for initial Eocene global warming. *Nature*, **429 (6991)**, 542–545.

Takahashi, T., W. S. Broecker, and S. Langer, 1985: Redfield ratio based on chemical data from isopycnal surfaces. *Journal of Geophysical Research: Oceans*, **90 (C4)**, 6907–6924, doi:10.1029/JC090iC04p06907, URL http://dx.doi.org/10.1029/JC090iC04p06907.

Takahashi, T., et al., 2009: Climatological mean and decadal change in surface ocean pCO2, and net sea–air CO2 flux over the global oceans. *Deep Sea Research Part II: Topical Studies in Oceanography*, **56 (8–10)**, 554–577, doi:http://dx.doi.org/10.1016/j.dsr2.2008.12.009, URL http://www.sciencedirect.com/science/article/pii/S0967064508004311.

Thomas, D., J. Zachos, T. Bralower, E. Thomas, and S. Bohaty, 2002: Warming the fuel for the fire: Evidence for the thermal dissociation of methane hydrate during the Paleocene-Eocene thermal maximum. *Geology*, **30 (12)**, 1067–1070.

Thomas, D. J., T. J. Bralower, and C. E. Jones, 2003: Neodymium isotopic reconstruction of late Paleocene–early Eocene thermohaline circulation. *Earth and Planetary Science Letters*, **209 (3–4)**, 309–322, URL http://www.sciencedirect.com/science/article/pii/S0012821X03000967.

Thomas, E., 2007: Cenozoic mass extinctions in the deep sea: What perturbs the largest habitat on Earth? *Geological Society of America Special Papers*, **424**, 1–23, doi:10.1130/2007.2424(01), http://specialpapers.gsapubs.org/content/424/1.full.pdf+html.

Thomas, E. and N. J. Shackleton, 1996: The Paleocene-Eocene benthic foraminiferal extinction and stable isotope anomalies. *Geological Society, London, Special Publications*, **101 (1)**, 401–441, doi:10.1144/GSL.SP.1996.101.01.20, URL http://sp.lyellcollection.org/content/101/1/401.abstract, http://sp.lyellcollection.org/content/101/1/401.full.pdf+html.

Tripati, A. and H. Elderfield, 2005: Deep-Sea Temperature and Circulation Changes at the Paleocene-Eocene Thermal Maximum. *Science*, **308 (5730)**, 1894–1898, doi:10.1126/science.1109202, http://www.sciencemag.org/content/308/5730/1894.full.pdf.

Tyrrell, T. and R. E. Zeebe, 2004: History of carbonate ion concentration over the last 100 million years. *Geochimica et Cosmochimica Acta*, **68 (17)**, 3521–3530, doi:10.1016/j.gca.2004.02.018, URL http://www.sciencedirect.com/science/article/pii/S0016703704001681.

Waddell, L. M. and T. C. Moore, 2008: Salinity of the Eocene Arctic Ocean from oxygen isotope analysis of fish bone carbonate. *Paleoceanography*, **23 (1)**, PA1S12–, URL http://dx.doi.org/10.1029/2007PA001451.

Wanninkhof, R., 1992: Relationship Between Wind Speed and Gas Exchange Over the Ocean. *J. Geophys. Res.*, **97 (C5)**, 7373–7382, URL http://dx.doi.org/10.1029/92JC00188.

Weiss, R., 1970: The solubility of nitrogen, oxygen and argon in water and seawater. *Deep Sea Research and Oceanographic Abstracts*, **17 (4)**, 721–735, URL http://www.sciencedirect.com/science/article/pii/0011747170900379.

Weiss, R., 1974: Carbon dioxide in water and seawater: the solubility of a non-ideal gas. *Marine Chemistry*, **2 (3)**, 203–215.

Wetzel, P., E. Maier-Reimer, M. Botzet, J. Jungclaus, N. Keenlyside, and M. Latif, 2006: Effects of ocean biology on the penetrative radiation in a coupled climate model. *Journal of Climate*, **19 (16)**, 3973–3987.

Winguth, A., C. Shellito, C. Shields, and C. Winguth, 2010: Climate Response at the Paleocene–Eocene Thermal Maximum to Greenhouse Gas Forcing - A Model Study with CCSM3. *J. Climate*, **23 (10)**, 2562–2584, doi:10.1175/2009JCLI3113.1, URL `http://dx.doi.org/10.1175/2009JCLI3113.1`.

Winguth, A. M., E. Thomas, and C. Winguth, 2012: Global decline in ocean ventilation, oxygenation, and productivity during the Paleocene-Eocene Thermal Maximum: Implications for the benthic extinction. *Geology*, **40(3)**, 263–266, doi:10.1130/G32529.1, `http://geology.gsapubs.org/content/early/2012/01/23/G32529.1.full.pdf+html`.

Zachos, J., M. Pagani, L. Sloan, E. Thomas, and K. Billups, 2001: Trends, Rhythms, and Aberrations in Global Climate 65 Ma to Present. *Science*, **292 (5517)**, 686–693.

Zachos, J. C., S. M. Bohaty, C. M. John, H. McCarren, D. C. Kelly, and T. Nielsen, 2007: The Palaeocene–Eocene carbon isotope excursion: constraints from individual shell planktonic foraminifer records. *Philosophical Transactions of the Royal Society A: Mathematical, Physical and Engineering Sciences*, **365 (1856)**, 1829–1842, doi:10.1098/rsta.2007.2045, `http://rsta.royalsocietypublishing.org/content/365/1856/1829.full.pdf+html`.

Zachos, J. C., G. R. Dickens, and R. E. Zeebe, 2008: An early Cenozoic perspective on greenhouse warming and carbon-cycle dynamics. *Nature*, **451 (7176)**, 279–283, URL `http://dx.doi.org/10.1038/nature06588`.

Zachos, J. C., M. W. Wara, S. Bohaty, M. L. Delaney, M. R. Petrizzo, A. Brill, T. J. Bralower, and I. Premoli-Silva, 2003: A Transient Rise in Tropical Sea Surface Temperature During the Paleocene-Eocene Thermal Maximum. *Science*, **302 (5650)**, 1551–1554, doi:10.1126/science.1090110, `http://www.sciencemag.org/content/302/5650/1551.full.pdf`.

Zachos, J. C., et al., 2005: Rapid Acidification of the Ocean During the Paleocene-Eocene Thermal Maximum. *Science*, **308 (5728)**, 1611–1615, doi:10.1126/science.1109004, `http://www.sciencemag.org/content/308/5728/1611.full.pdf`.

Zeebe, R., 2012a: LOSCAR: Long-term ocean-atmosphere-sediment carbon cycle reservoir model v2. 0.4. *Geoscientific Model Development*, **5**, 149–166.

Zeebe, R. E., 2012b: History of Seawater Carbonate Chemistry, Atmospheric CO2, and Ocean Acidification. *Annu. Rev. Earth Planet. Sci.*, **40 (1)**,

141–165, doi:10.1146/annurev-earth-042711-105521, URL http://dx.doi.org/10.1146/annurev-earth-042711-105521.

Zeebe, R. E., 2013: What caused the long duration of the Paleocene-Eocene Thermal Maximum? *Paleoceanography*, **28 (3)**, 440–452, URL http://dx.doi.org/10.1002/palo.20039.

Zeebe, R. E. and J. C. Zachos, 2007: Reversed deep-sea carbonate ion basin gradient during Paleocene-Eocene thermal maximum. *Paleoceanography*, **22 (3)**, PA3201, URL http://dx.doi.org/10.1029/2006PA001395.

Zeebe, R. E. and J. C. Zachos, 2013: Long-term legacy of massive carbon input to the Earth system: Anthropocene versus Eocene. *Philosophical Transactions of the Royal Society A: Mathematical,Physical and Engineering Sciences*, **371 (2001)**, doi:10.1098/rsta.2012.0006, http://rsta.royalsocietypublishing.org/content/371/2001/20120006.full.pdf+html.

Zeebe, R. E., J. C. Zachos, K. Caldeira, and T. Tyrrell, 2008: Carbon Emissions and Acidification. *Science*, **321 (5885)**, 51–52, doi:10.1126/science.1159124, URL http://www.sciencemag.org/content/321/5885/51.short, http://www.sciencemag.org/content/321/5885/51.full.pdf.

Zeebe, R. E., J. C. Zachos, and G. R. Dickens, 2009: Carbon dioxide forcing alone insufficient to explain Palaeocene-Eocene Thermal Maximum warming. *Nature Geosci*, **2 (8)**, 576–580, URL http://dx.doi.org/10.1038/ngeo578.

Acknowledgements

First and foremost I wish to thank my supervisor Tatiana Ilyina for her patient support and her ever open door whenever I had questions or need for discussions. I especially appreciate her continuous efforts to keep me on track, and for encouraging me all the way throughout this thesis. I would like to express my gratitude to my co-advisor Victor Brovkin for his continuous support, and for interesting discussions. Special thanks to Gerhard Schmiedl for stepping in as a reviewer on short notice. Without his help my defence could not have taken place on the anticipated date. I thank Jochem Marotzke for being my panel chair and for giving advice on the chosen path of research during this thesis.

I thank Dr. Katharina Six for her good company during several conferences, her scientific advice and her readiness to discuss whatever came into my mind. Furthermore, I thank Helmuth Haak for sharing his expertise and for his programming support and endless willingness to help. I enjoyed the helpful and productive discussions with Ernst Maier-Reimer and Rosina Grimm and would like to thank them for their continuous scientific support. I especially thank Laura Niederdrenk for operating my personal NCL and LaTex support-line.

Moreover, I want to thank the all members of MPI for making my stay at the institute very pleasant. Thanks to all the people with whom I had such a great time throughout my PhD especially Philipp Griewank, Fabio Cresto Aleina, Max Popp, Felix Bunzel, Jan Ackmann, Josiane Salameh, Malte Rieck, Sebastian Sonntag, Freja Vamborg, Florian Rauser and my PETM lunch buddy Rika Port.

I am glad to be a member of the International Max Planck Research School on Earth System Modelling (IMPRS-ESM). I thank Antje Weitz, Cornelia Kampmann, and Wiebke Böhm for their tremendous efforts to solve all the non-scientific problems so that I could fully concentrate on science.

Special thanks belong to my family and friends who supported me throughout the last years. Especially I want to thank Eva for always being there for me and for caring about little Hugo during the last couple of months of my PhD.

Eidesstattliche Erklärung

Declaration of oath

Hiermit erkläre ich an Eides statt, dass ich die vorliegende Dissertationsschrift selbst verfasst und keine anderen als die angegebenen Quellen und Hilfsmittel benutzt habe.

I hereby declare, on oath, that I have written the present dissertation by myself and have not used other than the acknowledged resources and aids.

Hamburg, den 07.10.2014

Mathias Heinze